UNIVERSITÀ DI PISA

Scuola di dottorato “Galileo Galilei”

Dottorato in Fisica applicata – XXIII ciclo

Tesi di Dottorato

Coherent and incoherent light generation with rare earth doped crystals

Raffaele Faoro

Relatore

Prof. Mauro Tonelli

Presidente del Dottorato

Prof. Francesco Pegoraro

Aprile 2013

Contents

1 Solid state visible light emitters **7**

1.1 Lighting source history 7

1.2 Solid State lighting 9

1.3 LED 10

1.4 OLED 12

1.5 Light sources based on Laser diode. 15

2 Theoretical background **17**

2.1 Characterization of visible sources 17

2.1.1 Useful notation and units on Radiometry and Photometry . . 17

2.2 Colorimetry 20

2.2.1 Human colour vision 20

2.2.2 CIE Chromaticity diagram 23

2.3 Rare earths 26

2.3.1 Free ions 27

2.3.2 Rare earth in the crystal field 31

2.4 Energy transfer in rare earth doped crystal 34

2.4.1 Radiative relaxation 34

2.4.2 Non radiative relaxation 36

2.4.3 Cooperative mechanisms 39

3 Experimental apparatus and crystals **45**

3.1 Crystals . . . 45

3.2 Czochralski growth method . . . 46

3.2.1 BaY_2F_8 . . . 47

3.2.2 KYF_4 . . . 48

3.2.3 KY_3F_{10} . . . 49

3.2.4 $LiLuF_4$ . . . 50

3.2.5 $LiYF_4$ . . . 52

3.3 Flux growth methods . . . 53

3.3.1 YPO_4 . . . 53

3.3.2 $Ba_2NaNb_5O_{15}$ . . . 53

3.4 Experimental apparatus . . . 54

3.4.1 X-Ray crystal orientation . . . 54

3.4.2 Crystals preparation . . . 54

3.4.3 Absorption measurements . . . 55

3.4.4 Excitation source . . . 55

3.4.5 Monocromator . . . 57

3.4.6 Detectors . . . 58

3.4.7 Integrating Sphere . . . 58

3.5 Experimental set-up . . . 59

3.5.1 Steady state fluorescence . . . 59

3.5.2 Decay-time measurements . . . 59

3.5.3 Intrinsic efficiency measurement . . . 60

3.5.4 Absorbed fraction determination . . . 62

3.5.5 Efficiency measurements . . . 62

4 White light generation **65**

4.1 Pr Levels . . . 65

4.2 Absorption measurements . . . 66
4.2.1 Absorption spectra . . . 67
4.3 Efficiency measurements . . . 73
4.3.1 Absorption . . . 75
4.3.2 Fluorescence . . . 78
4.3.3 Results . . . 82
4.4 Chromatic characterization . . . 86
4.5 Other dopants . . . 90
4.6 Conclusion . . . 96

5 KYF_4: Praseodymium 98
5.1 Absorption . . . 98
5.2 Fluorescence: diode vs argon . . . 100
5.3 Fluorescence: temperature behaviour . . . 104
5.4 Conclusion . . . 108

6 $Ba_2NaNb_5O_{15}$ Praseodymium 109
6.1 Structural characterization . . . 110
6.2 10 K emission spectra . . . 116
6.3 298 K emission spectra . . . 120
6.4 Decay time measurements . . . 123
6.5 Conclusion . . . 125

7 YPO_4 Dysprosium 127
7.1 Introduction . . . 127
7.2 10 K spectroscopy . . . 128
7.3 Room temperature spectra and Judd-Ofelt analysis . . . 135
7.4 Excited states dynamics . . . 139
7.5 Results . . . 142

8 Tm^{3+} $LiYF_4$: spectroscopy and laser experiment. 143

8.1 Absorption 145

8.2 Fluorescence measurements. 148

8.3 Cw and passive Q-switched laser experiment. 152

8.4 Conclusion 156

A Principal methods for the Correlated Colour Temperature determination 161

B Emission cross section 165

B.1 Reciprocity method 166

B.2 Integral $\beta - \tau$ method 168

Bibliography 171

Introduction

In recent years energy saving has become one of the most discussed and investigated subjects. In this direction many research works have been devoted to the design of new artificial lighting emitters with increased efficiencies. In fact, in most public, working and living places, artificial lighting is also used during daily hours. Therefore, even a small reduction of the presently large consumption of energetic resources could provide significant savings from both the economical and the ecological points of view. For these reasons, there is currently a great deal of interest in the development of simple and compact sources of visible radiation. The possible impact that an efficient, cheap and reliable visible source would have on display technology, optical processing and market has provided the stimulus for a great deal of work on new visible emitters. At the present time, new white light sources are represented by light-emitting diodes (LED), by organic light-emitting diodes (OLED) and nano crystals or nano particles inside particular hosts.

In the case of LEDs white light is obtained by mixing materials that emit light of different colours or by using phosphors to downconvert a blue or UV wavelength. In both cases a mixture of phosphors or a complex doping scheme is needed to achieve white-light emission [1, 2]. Recently new commercial displays have been produced using organic light emitting diodes (OLED). Despite of their favourable properties [3, 4, 5, 6], OLEDs show limited lifetime and power scaling capabilities.

Materials for two and three dimensional displays can employ up-conversion of

infrared light by means of nano particles of optimized composition dispersed in a polymer [7, 8, 9] or embedded in a film [10]. Results are very promising, but the efficiency of the device obtained is inherently limited by the up-conversion process which needs high power, high doping levels, and in any case does not usually exceeds 5% overall efficiency. Once used only for indicator lights, Solid State Lighting (SSL) technology is now replacing conventional technologies in traffic lights, exit signs, airplane and taxiway edge lights [11]. Today SSL are expected to replace conventional technologies such as incandescent and fluorescent lighting.

As the "perfect" source has not been found yet, the impact that a new efficient, inexpensive and reliable visible laser source would have on data Storage, display technology, undersea communication and optical processing has stimulated their development in the last years.

In this thesis fluorides and oxides Pr-doped are characterized as new Solid State sources in the visible range. Since the trivalent Praseodymium ion (Pr^{3+}) has several transitions in the visible spectral range, it is suitable for both incoherent white light emission and for visible laser emission. Direct pumping of Pr^{3+}-lasers operating at room temperature has been realized with Ar-ion lasers [12]. These pumping systems did not match the absorption lines of Pr^{3+} well and laser emission resulting in moderate efficiencies. Suitable laser diodes based on GaN, emitting in the blue spectral region, have been commercially available since 2003. Since then the investigation of new Pr-doped laser materials pumped with a blue laser diode has increased.

Compared to the mixing of three colours obtained from three different ions (Er, Tm, Ho usually) the Pr emission efficiency is potentially higher because it is minimized the interaction between energy levels of different ions which can cause quenching of the emission. Moreover the efficiency is not limited by the up-conversion process. Besides, the inorganic bulk fluorides investigated have very low phonon energy (a few hundreds of cm^{-1}), and they usually show lower non-radiative decay rates

owing to the quenching of radiation. Fluorides are relatively hard, not hygroscopic and not prone to ageing problems therefore they posses a virtually unlimited lifetime and better power scalability than LEDs and OLEDs. Last but not least, fluorides have gained renewed attention in the last years thanks to the excellent laser results recently obtained by several research groups that demonstrate the high optical quality of the samples that can be produced with the present crystal growth technology. Fluoride crystals are also characterized by a large versatility of compositions and of shapes. Indeed new crystal growth methods have been developed in recent times that can produce single crystals in a variety of shapes. For example the Laser Heated Pedestal Growth and micro-pulling down methods can produce single crystal fibres with a diameter from 100 μm to some mm and length up to hundreds of cm [13] lowering in addition the production costs respect to traditional bulk crystal growth methods.

This work also investigates other promising rare earth as visible emitters, such as Dysprosium in oxide (YPO_4) and Europium and Samarium in fluorides (BaY_2F_8), all this materials has interesting emission in the visible light and could be excited using some inexpensive GaN laser diode, with an emission of $\sim$ 405 nm.

The last part of the thesis regards the coherent light generation in the 1.9 micron regions, that is part of the so called "eye safe" wavelength region. Laser systems that operate in this region offer exceptional advantages for free space applications compared to conventional systems that operate at shorter wavelengths. This gives them a great market potential for the use in LIDAR and gas sensing systems and for direct optical communication applications. The favourable absorption in water makes such lasers also very useful for medical applications.

In particular it was studied the potential of Tm doped $YLiF_4$, and its emission around 1.9 micron to realize a Diode Pumped Solid State Passive Q-switching laser. Diode pumped solid-state lasers (DPSSL) allow great compactness, easy handling

and high-power operation. The Tm^{3+} ion is versatile due to its absorption around 800 nm, which matches the commercially available AlGaAs diode lasers designed for Nd^{3+} pumping, its relatively long excited level lifetime and its efficient cross-relaxation process. Continuous wave DPPSL with Tm ions in oxide and fluorides are already studied, showing output power over 100 Watt and slope efficiency up to 50% [14]. The choice of passive Q-switching is due to the fact that the realization is much simpler and cheaper compared with the active Q-switching and more important, it generates shorter pulses and consequently higher peak power, which is advantageous for OPO pumping. While the use of oxide for PQS lasers are already studied in several host such as YAG [15] or isostructural $KLu(WO_4)_2$ [16], the use of fluoride crystals as active media is an unexplored field. Fluoride crystals exhibit longer fluorescence lifetimes and hence longer energy storage times than most other hosts [17, 18]. The use of fluoride crystals as laser hosts is favoured because of their wide transparency window (ranging from UV up to far IR) and the low phonon energy; in particular $YLiF_4$ phonon energy, 440 cm^{-1}, is less than one half of the typical oxides value. Thus, the motivation for this research was to achieve higher single pulse energy and shorter pulse durations.

In chapter 1 the state of the art on white light emission, describing the main methods used in lighting and display applications, is presented.

In chapter 2 I review the general theory of rare earth doped materials with particular attention to the description if the energy levels calculation as well as to relaxation and cooperative processes. I also introduce the fundamental concepts of the chromatic theory for the description of white light emitting source.

In chapter 3 I overview the different experimental set-up we used to obtain the experimental data of this thesis. I also show the main features of the crystals on which we performed our measurements.

In chapter 4 I propose some Pr-doped fluoride crystals (BaY_2F_8, KYF_4, KY_3F_{10}

and $LiLuF_4$) as possible solid-state white-light emitters. In this frame we measured the chromatic coordinates, the conversion efficiency and also its dependence from the doping concentration, and the volume of samples. It is well known that Pr-doped crystals show a bright emission in the visible range, but at the best of my knowledge a systematic study on the spectroscopic features of these materials has never been carried out. I also present some preliminary studies on some other dopants, such as Eu^{3+} and Sm^{3+} in BaY_2F_8, in order to understand if these ions can be a good candidate as visible-light emitters. The emission of these two probe samples, under a UVLED excitation are presented. Colour-coordinates have been calculated in order to characterize the emission.

In chapter 5, I present a spectroscopic investigation on KYF_4:1.25at% Pr^{3+} I report in detail on the effects of the multisite-disordered nature of the sample on its optical properties. In particular I discuss the broadening of the ^3P_J absorption lines, at room temperature, and the 570-665 nm orange-red polarized emissions pumping the $^3P_2$ and $^3P_1$+$^1I_6$ manifolds at 445 and 457 nm respectively. The $^3P_0$ lifetime was in agreement with that measured in other fluoride hosts. Moreover The unpolarized emission as a function of temperature (300-700 K) has been measured in order to evaluate the KYF_4 phonon energy.

In chapter 6 different $Ba_2NaNb_5O_{15}$ trivalent Praseodymium doped crystal are studied, focusing on the visible emission of this materials. Their visible emission properties are reported as a function of the doping level under different excitation and temperature conditions. The experimental observations are accounted for by considering the effects of the crystal structure, of the doping mechanisms and of the interactions between host lattice and doping ions. The proposed conclusions are verified by means of single crystal X-ray diffraction measurements and the resulting site occupancies of the active ions are discussed in the light of the synthesis procedure.

In chapter 7 I present the Dy^{3+}-doped YPO_4 crystal, investigated by optical spectroscopy techniques. The energy level scheme of the active ion has been deduced from the low temperature spectra and reproduced by means of a crystal-field calculation. The room temperature absorption spectra have been analysed in the framework of the Judd-Ofelt approach, and the results of this analysis have been applied in a discussion concerning the spectral composition of the visible luminescence.

In chapter 8 I present the optical characterization around 1.9 micron emission of a Tm:YLiF sample. Absorption, steady state and dynamical fluorescence are reported. Emission and absorption cross section of the 1.9 μm transition are presented, and they are discussed in order to understand the laser behaviour in Cw e PQS regimes. Finally the Cw and Passive Q-switching laser is reported, giving as best results of 14 ns long pulse and a peak power of $\approx$ 65 kW.

In Appendix A I present the methods used for the calculus of the Correlated Colour Temperature (CCT).

Chapter 1

Solid state visible light emitters

In this chapter a review of the history of lighting sources based on pyroluminescence, electricity, and fluorescence is reported. More exhaustive historical information can be found in [19]. Following a brief overview and state of the art of solid state sources is reported.

1.1 Lighting source history

Natural light comes from the sun. The solar spectrum includes not only the visible light (with wavelengths from 0.38 to 0.78 μm) but also UV light and infrared radiation. The ideal lighting source should be close to sunlight's spectrum, that can be approximated as a blackbody with a temperature of 5800 K. The main technologies for white light production have been three: pyroluminescence, electricity and fluorescence.

Up to the beginning of the 19^{th} century, artificial light was produced by pyroluminescence, which is due to radiative transitions in excited atoms and ions, recombination of ions to form molecules, and incandescence of solid particles in flames. For thousands of years torches (made of vegetables treated with flammable

substances-pitch, wax, resin, tallow, oil, etc.) were the only artificial sources of light. Amié Agrand from Geneva invented an oil lamp with a tubular wick placed within two concentric tubes and a glass chimney around the burner. These sources have a black-body emission spectrum, but since their temperature is very low the emission peak is always in the IR region. This leads to a very low efficiency in the visible region.

Gas lighting was introduced by William Murdoch in 1772. In 1826, Thomas Drummond invented the first crystalline lighting device (called the limelight) based on candoluminescence, which emits in excess of blackbody incandescence due to thermal excitation of ions (discovered in 1820 by Goldsworthy Gurney). The device consisted of a cylinder of lime (calcium oxide), which was brought to a state of dazzling brilliancy by the flame of an oxyhydrogen blowpipe. Also in this case the efficiency was very low. This kind of source was used only in theatre and in street lighting.

Thanks to the invention of a direct current generator (dynamo machine) by Z.T. Gramme (1870s), in 1876 Paul Jablochkoff demonstrated the first practical electric lighting device. This happened two centuries after the effect of the luminous discharge of static electricity in mercury vapour was discovered. In 1879 Swan demonstrated an incandescent lamp (British patents n. 18 and 250 of 1880) but a couple of months later, Edison demonstrated his devices and obtained a patent for a filament lamp (U.S. patent no. 223 898 of 1879). In 1903, the tungsten filament was invented by A. Just and F. Hanaman. In this process higher temperatures are obtained and the emission peak shifts to shorter wavelength increasing the visible light emitted. In this way the efficiency is higher than that obtained by the pyroluminescence.

In 1900, Peter Cooper Hewitt patented the mercury vapour lamp, and in 1938 GE and Westinghouse Electric Corporation introduced new coloured and white low-pressure mercury discharge lamps with the inside of the tube coated with a phosphor

powder. The fluorescent lamp employs photoluminescence excited by UV emission of mercury (at least 50 lm/W) and is much more efficient than the incandescent lamp (16 lm/W) [20].

1.2 Solid State lighting

The first solid state source based on the electroluminescence processes has been presented in 1907 by H. J. Round. He discovered electroluminescence in a silicon carbide semiconductor. About 60 years later by N. Holonyak Jr. and S. F. Bevacqua presented a p-n junction emitter of visible (red) light [21]. The first LEDs with efficiency that exceeds filtered incandescent lamps based on double heterostructures were developed by Kroemer [22]. From then on, many different solid state sources consisting

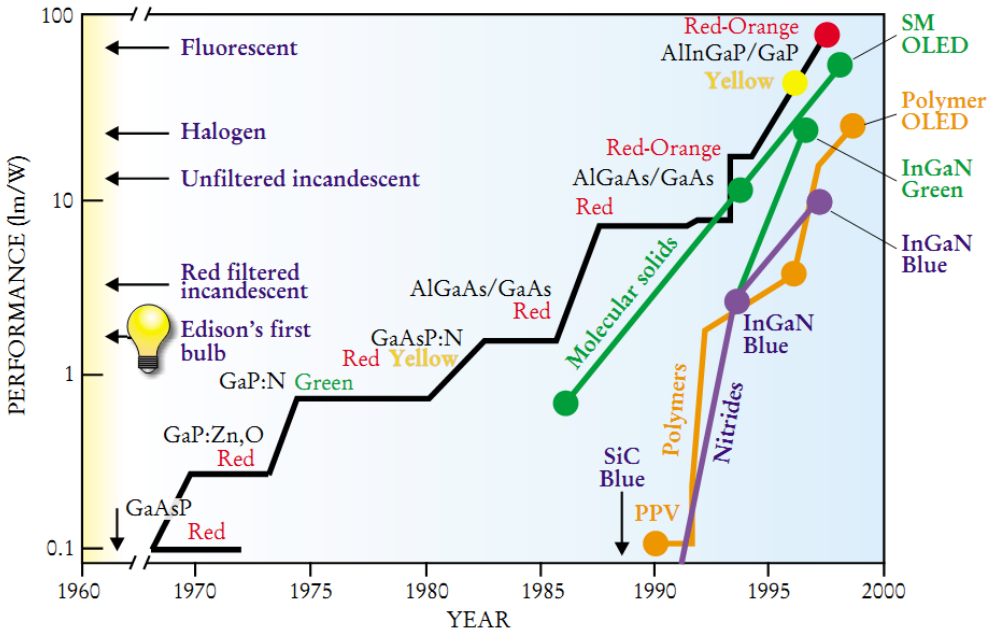

Figure 1.1. The evolution of total efficacy of solid-state lighting technologies [23]

of different materials have been proposed. The main ones are: LED (Light Emitting

Diode), OLED (Organic Light Emitting Diode) and devices based on the emission of nano-crystal and nano-powder dispersed in different materials. Breakthroughs in light-emitted diode (LED) and organic light-emitted diode (OLED) technology are catalysing advances in solid state lighting (SSL) devices. SSL technology is now replacing conventional technologies in traffic lights, exit signs, airplane taxiway edge lights, and other application. SSL has the potential to double and increase even more the efficiency of general lighting systems in the coming decades, making it the best option for reducing energy consumption [11, 24]). This research field is always progressing and producing every day new materials and new device designs. A graph of the development of the solid state sources is reported in Figure 1.1.

1.3 LED

The LED (Light emitting diode) consists of a chip of semiconducting material doped with impurities to create a p-n junction. The light emission is produced by the electron-hole recombination. The wavelength of the light emitted, and therefore its colour, depends on the band gap energy of the materials forming the p-n junction. The emission is monochromatic and thus unuseful for general lighting applications. To create white LED sources, three methods are commonly used [25] (Figure 1.2):

- *Colour mixing*: mixing the output from three RGB (red green and blue) LEDs. The colour mixing approach has the advantage of highest maximum luminous efficiency of 150 lm/W (no conversion loss) [20]. However, the absence of efficient LEDs in the green region of the spectrum currently limits this approach. This is the most expensive option since it requires the use of three LEDs per lamp. Also, the three or more different colour components have different voltage requirements, different degradation characteristics and different temperature dependencies, a sophisticated colour system balance is required.

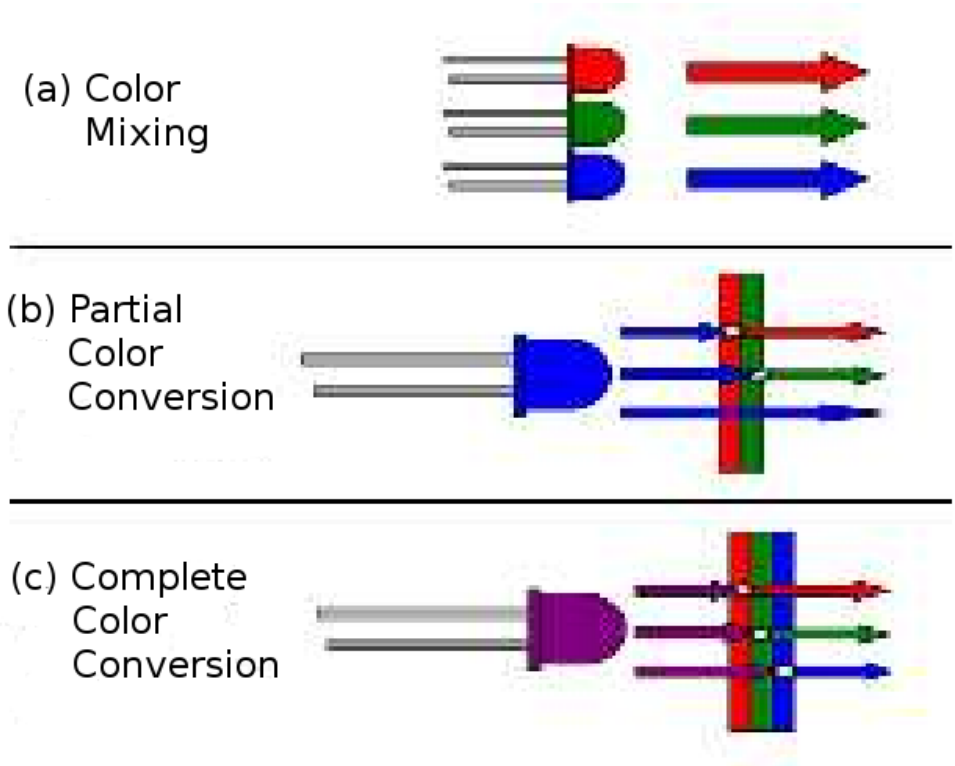

Figure 1.2. Three main approaches to solid-state lighting [25]

- *Partial colour conversion*: a blue pump source is partially phosphor-converted to yellow. The remaining unconverted blue pump light is transmitted through the phosphor and combines with the yellow-converted light to form white light [26]. The blue LED plus phosphor strategy has the shortest time line for commercialization. Companies as Nichia, CREE, and others, already have demonstrated white light generation by using a blue LED and a single phosphor (YAG:Ce). Part of the blue light emitted by the LED escapes and an other part is converted by the phosphor to an amber colour that is the complimentary colour of the blue light emitted by the LED. With this approach two main problems arise: the halo effect and the low level absorption of blue light by the phosphor. The first, relative to the multicolour no-white perception

of the light by an observer, occurs because the light from the blue LED is directional while the amber light from the phosphor radiates over a 2π solid angle.

- *Complete colour conversion*: the output from a single UV or violet LED is completely absorbed and converted by two or more phosphors to white light. In this case many fluorescent materials and complex doping schemes have to be used [1, 27]. High colour rendering index, similar to fluorescent lamps, can be realized. Since the UV light is not used directly, as the blue pump radiation in the partial conversion, the UV source efficiency has to compensate the conversion losses.

1.4 OLED

An OLED (organic light-emitting diode) is a light-emitting diode (LED) in which the emissive electroluminescent layer is a film of organic compound which emits light in response to an electric current. This layer of organic semiconductor is situated between two electrodes The first demonstration for OLED lighting regarded the green OLED and was reported by Kodak in 1987. The dopant-based green and red OLEDs were presented in 1989 [28, 29]. The possibility of producing a flat large area lighting panel with a cheap and simple process will enable novel products and new fields of application. Due to their high contrast ratio, their colour gamut and flexibility OLEDs are especially useful in the display development. In the last period their application in the lighting field has been investigated. White light-emitting OLEDs can be fabricated by four approaches (Figure 1.3) [30]:

- A single white emitting stack, where the white emission is achieved by using a combination of different emissive components providing red, green, and blue light from a single emitting layer. With this approach, building the device is

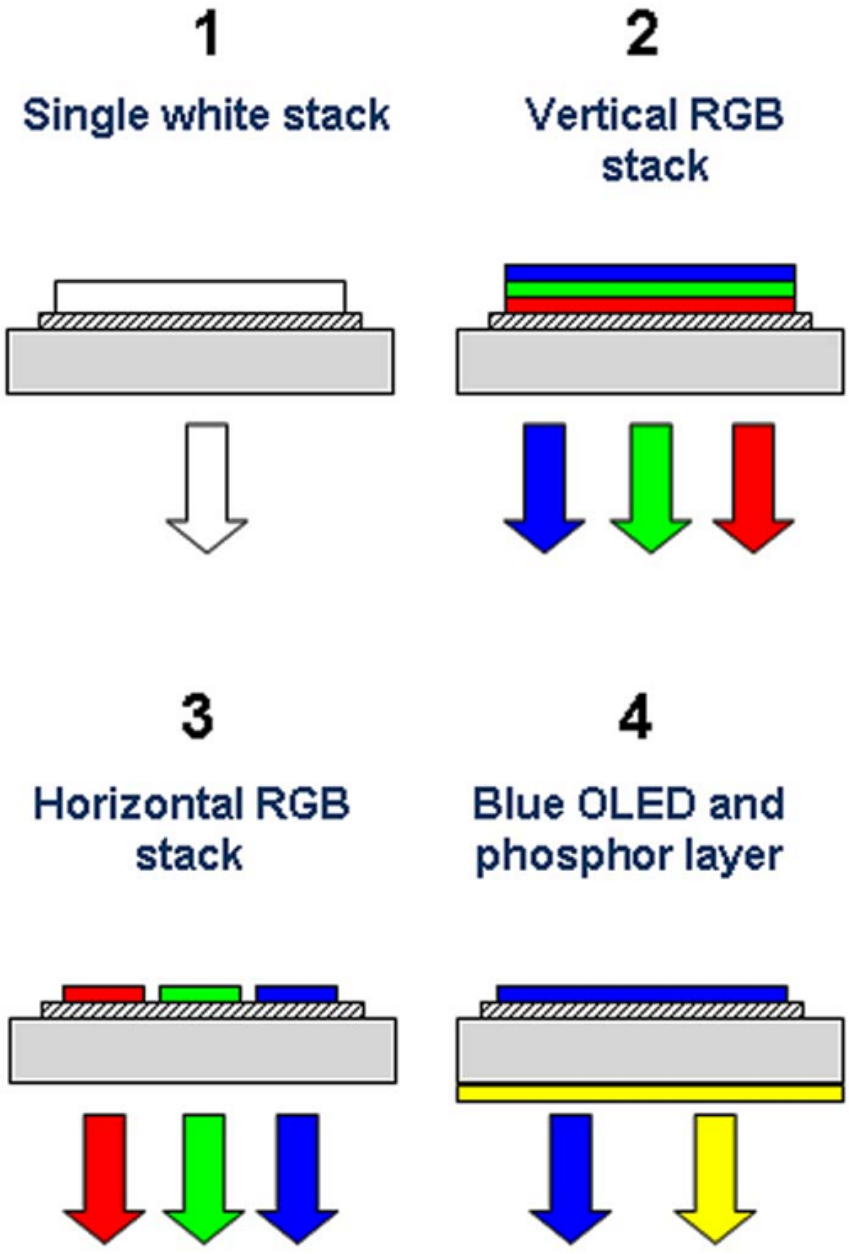

Figure 1.3. Four main approaches to OLED production [30]

easy but tuning the colour without affecting device performance becomes a difficult task (Figure 1.3) [31].

- A vertical red-green-blue (RGB) stack, where the output spectrum of such a device is determined by the three light emitting components. This device architecture leads to colour homogeneity over the active area but relies on complex processing methods (Figure 1.3) [32, 1].

- A horizontal RGB stack ,where the output spectrum of the horizontal stack can be changed while operating the device when addressing the patterns separately. Compared with the vertical configuration the three colour are spatially separated. Consequently, the emitted light is not so homogeneous (Figure 1.3).

- A single colour emitting OLED in combination with a conversion layer. This approach can be implemented by easy fabrication techniques and can provide better colour stability as the ageing rate is determined by only one emitter. White light-emitting devices by the means of luminescence conversion based on an inorganic blue light emitting LED and conversion by phosphor were first published by Schlotter et al. [33](Figure 1.3).

The principal problem of OLED devices is related to their cost and their insufficient operating lifetime. There are several problems that limit their useful lifetime: reaction with the ambient (oxygen, CO_2 and moisture); electrochemical degradation (reduction or oxidation), and spontaneous statistical conversions/decay of the charged species. Finally, emitters of different colour age with different rates, which means that the quality of white light will deteriorate with time.

In the last years, the hybrid Inorganic/Organic (I/O) approach has been proposed [25]. This technology combines high power, long lifetime inorganic LEDs with organic lumophores that have very high photon conversion efficiency, adjustable emission colour, can be easily deposited over large areas, and are very low cost.

1.5 Light sources based on Laser diode.

The technology of visible light sources based on frequency up-conversion of infrared-to-visible light in rare earth doped materials has been revisited recently with the development of powerful 980 nm lasers. The materials investigated are usually doped with Yb^{3+} as an absorber or donor ion and an acceptor or emitter ion that can be: Erbium (Er^{3+}), Holmium (Ho^{3+}) and Thulium (Tm^{3+}). The efficiency of the visible light produced with this method showed that Up-Conversion technology is a realistic alternative to the existing display technologies. A major benefit to using this process is the ability to operate displays at very high-brightness without degradation of the emitting materials. Also the low energy pump photons do not produce damage in the up-conversion materials. In this field Prof. Michael Bass proposed the emission of white light from powders of fluoride crystal ($NaFY_4$, KY_3F_{10} and YF_3) doped with rare earth and dispersed in a polymer (PMMA) [8, 9, 7]. The benefit to using crystal powders is that they can be mixed in any proportion without modifying their individual properties. However if the infrared pump increases the efficiency of the system, the up-conversion transfer efficiency represent the efficiency limit of the device.

In the recent years the developing of GaN laser diode with an emission in the blue-purple and near UV regions commercially available since 2003 permits to rediscover some fluorescing materials already investigated for coherent light generation. The basic idea is to substitute the LED with the laser diode, and using one of the conversion scheme exposed in the previous section 1.3. Furthermore the developing blue-ray disk (405 nm laser diode) and video-projector based on laser diode have been decreasing the cost of the laser of one order of magnitude in the last 10 years, making the realization on large scale of laser based lighting system more interesting from the economical point of view. That laser allow to excite the materials with narrow absorption bands not matched by the emission of the LED, like fluorides

incorporating rare earth, such as Praseodymium (Pr) and so on. These materials were already investigated for coherent light generation, normally excited with an Ar-ion laser [12], but the huge dimension of ionic lasers make this pumping scheme not suitable for the lighting purpose, that is possible due to the small dimension of the GaN laser diodes. In the 2010 the Professor Tonelli group investigate the efficiency properties of Praseodymium doped fluorides for white light generation, reporting a maximum intrinsic efficiency of 60% [34]. Indeed the use of materials doped only with one rare earth ions reduce the possibility of non radiative processes, that limit the overall efficiency as in upconversion processes.

Chapter 2

Theoretical background

In this chapter I will describe the most important theoretical features concerning the colour definition and the rare earth ions useful for this thesis. The first section of this chapter will concern the theory for the chromatic characterization of a light source: colour definition, human eye view and units. In the second section, the background theory of rare earth ions in crystals will be presented. All the results regarding the general features of rare earth ions are based on the works of Refs. [35, 36, 37]. The chromatic theory refers to the CIE (Commission Internationale de l'Enclairage) published parameters, to *Handbook of Optics I* [38] and to *Handbook of Optics III* [39].

2.1 Characterization of visible sources

2.1.1 Useful notation and units on Radiometry and Photometry

In reference [39] it is possible to find an in depth description of the principles of radiometry and photometry. In this subsection we will introduce only the definitions

and the units useful for the present work.

Radiometry

Radiometry is the measurement of optical radiation in the electromagnetic spectrum, namely the radiation within the frequency range from 3 x 10^{11} to 3 x 10^{16} Hertz (Hz).This range corresponds to wavelengths between 0.01 to 1000 micrometers (μm) and includes the ultraviolet, visible and infrared regions. The radiometry units can be divided into two classes: those concerning the power or energy and those that are geometrical in nature. In the first class are: the energy, that in the SI (International System-derived unit is measured in joules (J); the power or radiant flux, defined as the derivative of the energy with respect to time, that is measured in watt (W). In the second class are: the irradiance or flux density, derivative of the power with respect to the area (W m^{-2}); the radiant intensity, power per unit of solid angle; the radiance, power per unit of projected area per unit of solid angle (W m^{-2} sr^{-1}).

Photometry

Photometry is the measurement of electromagnetic radiation detectable by the human eye. It is thus restricted to the wavelength range from about 360 to 830 nm. Photometry is identical to radiometry except that everything is weighted by the spectral response of the nominal human eye. The base unit for photometry is the lumen (lm) and is defined by the following standard: at a wavelength of 555 nm, one watt of radiant power is equal to 683 lumens.

In Table 2.1.1 are reported the relevant quantities and their radiometric and photometric units. Most of the quantities reported refer to the nature of the source (point source or radiating surface of a given area) and to the geometry of the detection system. To convert a radiometric to a photometric quantity the CIE (Commission Internationale de l'Enclairage) introduced the empirical curve V(λ) defined as

	Radiometry		**Photometry**	
Quantity	Name	Unit	Name	Unit
Power Radiant	flux	Watt (W)	Luminous flux	lumen (lm)
Power per area	Irradiance	$W \cdot m^{-2}$	Illuminance	$lm \cdot m^{-2}$=lux (lx)
Power per solid angle	Radiant intensity	$W \cdot sr^{-1}$	Luminous intensity	$lm \cdot sr^{-1}$ =candela (cd)
Power per area per solid angle	Radiance	$W \cdot m^{-2} \cdot sr^{-1}$	Luminance or brightness	$lm \cdot m^{-2} \cdot sr^{-1}$ $=cd \cdot m^{-2}$ =nit

Table 2.1. Radiometric and photometric quantities and units.

the spectral response of the human eye. Since the eye has two classes of photosen-

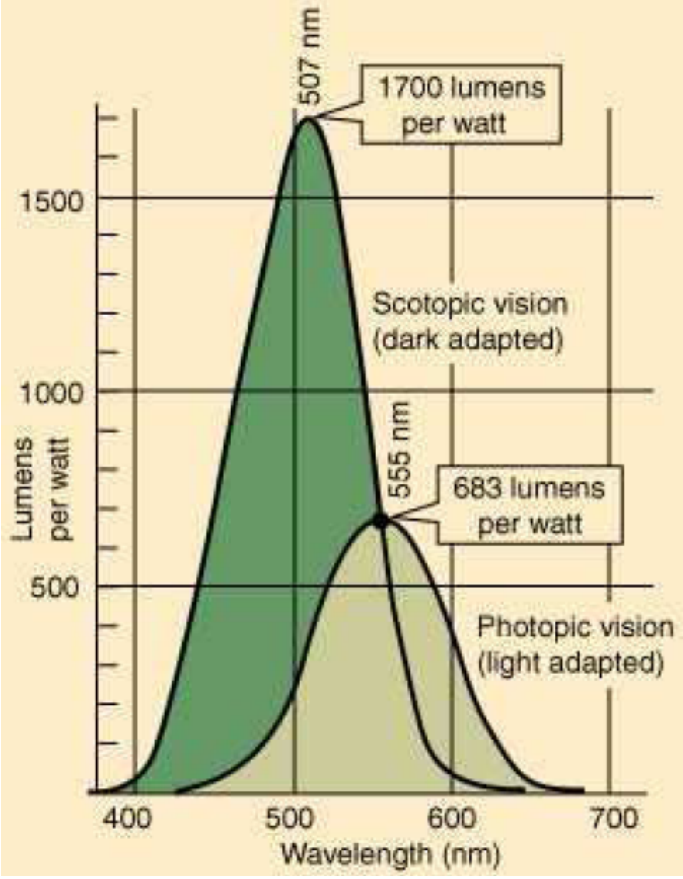

Figure 2.1. Response of human eye: absolute spectral luminous efficiency functions for photopic and scotopic.

sors: *cones* and *rods*, the $V(\lambda)$ function assume two different values in these cases.

Photopic vision (the vision of the eye under well-lit conditions) mainly concerns the cones, where V(λ) peaks at 555 nm and goes to zero beyond 400 and 750 nm. Where scotopic vision (the monochromatic vision of the eye in dim light) is concerned with the rods, where V(λ) peaks at 507 nm and goes to zero beyond 360 and 650 nm. Multiplying V(λ) by the factor K_m= 683 lm$\times$ W^{-1} the absolute spectral luminous efficiency can be obtained (Figure 2.1). A luminous quantity X_ν is obtained by:

$$X_\nu = K_m \int_{360}^{750} X_\lambda V(\lambda) d\lambda \tag{2.1}$$

where X_λ is the corresponding radiant quantity spectral distribution.

2.2 Colorimetry

The goal of colorimetry is to incorporate properties of the human colour vision system into the measurement and specification of visible light. Colorimetry provides quantitative representations that predict when two lights will appear identical to the human observer, allowing colour reproduction (e.g. nature and paint, photography, display, printing, etc). A good introduction to colorimetry can be found in Reference [40].

2.2.1 Human colour vision

Human colour vision derives from the response of the cones contained in the retina of the eye. There are three types of cones corresponding roughly to red, green, and blue sensitive detectors. Each of these photoreceptors responds differently to the spectral composition of light. The "green" and "red" cones are mostly packed into the fovea centralis. The approximate spectral sensitivities of these photo-receptors are shown in Figure 2.2. The relative heights for the three types are set equal for

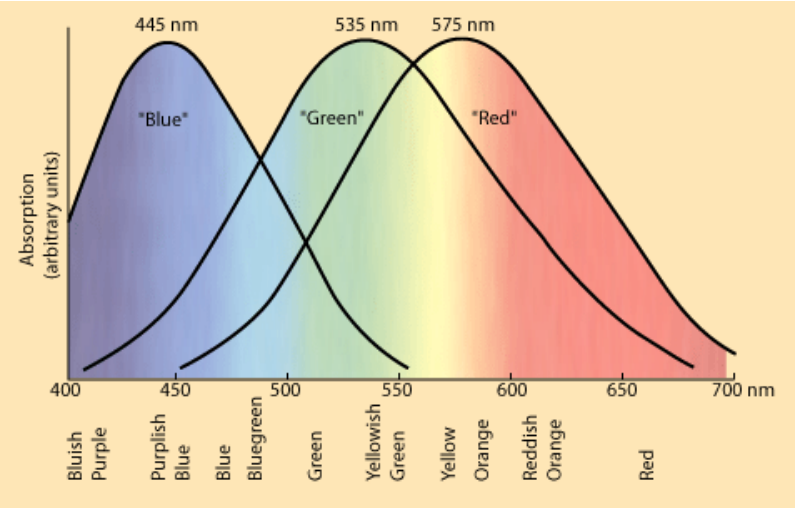

Figure 2.2. Normalized colour sensitivity of the red-, green- and blue-sensitive cones of the human eye [41]

lack of detailed data.

The colours we see are usually not monochromatic, but rather are the superposition of visible wavelengths characterized by an intensity-distribution curve. Coloured lights appear the same to us, no matter what are their intensity-distribution curves, provided that three of their properties are the same: their hue, saturation and brightness for coloured lights and lightness for coloured surfaces.

- *Hue* corresponds to the main colour: it is what distinguishes one spectral colour from another. It is specified by the dominant wavelength in the intensity-distribution curve.

- *Saturation* corresponds to the purity of the colour. A very saturated colour generally has almost all its intensity fairly close to the dominant wavelength, while an unsaturated colour would have contribution from many other wavelengths. Monochromatic colours have the highest saturation and white light is completely unsaturated. Other colours may be thought as a mixture of white light with a saturated colour.

- *Brightness* refers to the sensation of overall intensity of a light, ranging form dark, through dim, to bright, and dazzling. For surface colours, the third property is lightness which is related to the percentage of incident light reflected by a surface and refers to the whiteness, grayness or blackness of a colour.

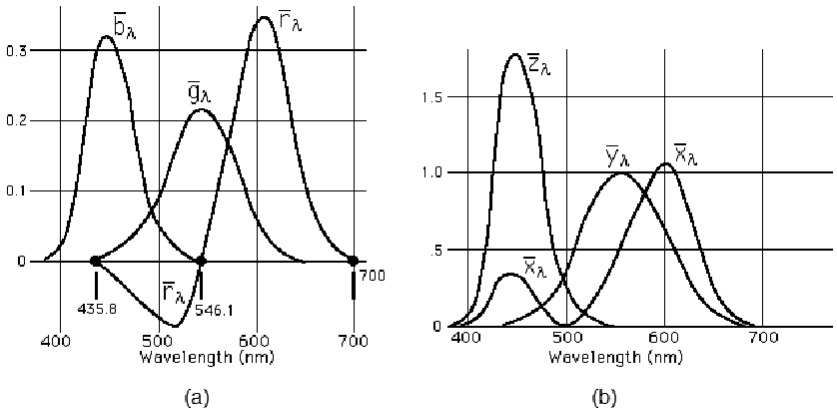

Figure 2.3. (a)The historical RGB colour matching functions and (b) the CIE 1931 colour matching functions [41].In both case the vertical axis is the tristimulus value

Overlapping spots of light on a white screen, i.e. a screen which diffusely reflects all the visible wavelengths equally well, combines their colours by additive mixture. In the 1920's colour matching experiments were conducted showing that, if it were possible to remove some amount of one or more colours (sometimes referred to as negative amounts of colour), any colour could be matched by an additive mixture of monochromatic red at 700 nm, green at 546.1 nm and blue at 435.8 nm. These three colours are called the RGB primaries. Colours that additively combine to produce white are called complementary colours. The weights given to the three primaries in order to match a colour are called tristimulus values.

The *tristimulus values* at all wavelengths of the visible spectrum constitute the colour matching functions, which for the historical RGB primaries are shown in

Figure 2.3 (a). A negative value on a colour matching function indicates that some colours cannot be exactly produced by adding up the primaries.

2.2.2 CIE Chromaticity diagram

In 1931, the CIE derived a new set of primaries from the RGB primaries matching functions of Figure 2.3 (a). This new set of primaries, called X, Y, and Z, was derived so that the set always produces positive tristimulus values. It is possible to represent any colour in terms of these primaries and equal values of X, Y, and Z produce white. They also were arranged so that a single parameter Y determines the luminance of the colour. The CIE defined the Standard Observer to have the colour-matching functions shown in Figure 2.3 (b). These tristimulus values specify the chromaticity, i.e. the amounts of three standard primaries X, Y, Z needed to exactly reproduce any visible colour via the following formulas where E(λ) is the product of the surface reflectance and the light source distribution :

$$X = \int E(\lambda)\bar{\mathrm{x}}(\lambda)d\lambda, \tag{2.2}$$

$$Y = \int E(\lambda)\bar{\mathrm{y}}(\lambda)d\lambda, \tag{2.3}$$

$$Z = \int E(\lambda)\bar{\mathrm{z}}(\lambda)d\lambda. \tag{2.4}$$

All visible colours are found in a horseshoe shaped cone in the X-Y-Z space. As it is a 3D space it is impractical to work in it directly. It is common to project this space to the X+Y+Z=1 plane. The result is a 2D space known as the CIE chromaticity diagram shown in Figure 2.4. The coordinates in this space are usually called x,y

and z and they are derived from X-Y-Z using the following equations:

$$\mathrm{x} = \frac{X}{X+Y+Z}, \tag{2.5}$$

$$\mathrm{y} = \frac{Y}{X+Y+Z}, \tag{2.6}$$

$$\mathrm{z} = \frac{Z}{X+Y+Z} = 1 - \mathrm{x} - \mathrm{y}. \tag{2.7}$$

As the z component bears no additional information, it is often omitted. Note that since x-y space is just a projection of the 3D X-Y-Z space, each point in x-y corresponds to several points in the original space. As the missing information is the luminance Y, a colour is usually described by x,y,Y coordinates, where x and y determine the chromaticity and Y the brightness component of the colour.

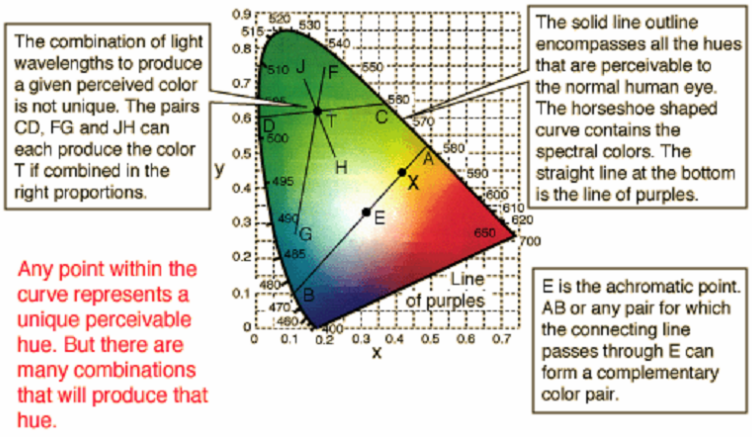

Figure 2.4. The 1931 CIE chromaticity diagram [41]

The horseshoe outline is the locus of the saturated (monochromatic) colours, i.e. the colours produced by one wavelength of the visible spectrum. Inside the horseshoe shaped locus are all the spectral colours, i.e. the colours produced by any combination of the monochromatic colours. We note that the line of purples, the straight line connecting the lowest wavelength blue and the highest wavelength red,

does not represent spectral colours.

White is perceived when the colours add to achieve a value in the central part of the CIE diagram. A particular white point is of theoretical interest as it gives certain information about spectral colours. It is the achromatic white point E of Figure 2.4 which is the point of coordinates x=1/3, y=1/3, z=1/3, i.e. formed by mixing equal amounts of the three primaries.

By drawing a straight line connecting the achromatic point E and any spectral colour of coordinate x,y, we can derive important information about this spectral colour, namely its dominant wavelength, its degree of saturation and its complementary colour. The dominant wavelength of the spectral colour (which determines this colour's hue) is determined by the intersection of this line with the horseshoe outline. For instance in Figure 2.4, the dominant wavelength of all the colours lying on the straight line between points E and A (for instance point X) is given by point A. The degree of saturation of colour X is given by the ratio of the distances $\overline{XE}$ and $\overline{AE}$. If this ratio close to unity, i.e. X is close to the spectral horseshoe outline, its saturation is high. If the ratio is small (X close to the achromatic point) it means the colour of point X is unsaturated.

The complementary colour of any spectral colour X is found by extending the straight line between X and E through the achromatic point to the opposite side of the horseshoe outline. For instance, on Figure 2.4 point B is the complement of point A and of any spectral colour located on the straight line between A and E.

An interesting property of the x,y chromaticity diagram is that all possible mixtures of two colours x_1,y_1 and x_2,y_2 are given by the straight line connecting these two points. As a result, all the possible mixtures of three colours x_1,y_1, x_2,y_2 and x_3,y_3 lie inside the triangle determined with those three points. For instance, using 650 nm red, 520 nm green and 460 nm blue as the three primary colours, any colour inside the large triangle can be made without using negative contributions of the

tristimulus values.

The gamut of colours is all colours that can be reproduced using the three primaries. These three colours give about as big a triangle can fit inside the horseshoe, so they give the biggest gamut without negative contributions, i.e. what can be physically achieved with three lights. That is why blue, green and red are called the additive primary colours. Of course, even by using the primary colours, other spectral colours cannot be produced. However, for most purpose that is not important, because most colours occurring in nature are unsaturated.

In spite of all its useful characteristics, the 1931 CIE x,y chromaticity diagram has one important caveat: if the distance between any arbitrary two points is the same as the distance between another two points, the perceived amount of change in colour from one point to the other will not be the same for the two pairs. In order to correct this, researchers are trying to find a perceptually uniform colour space. It has, unfortunately, still not been found. CIE proposed two alternatives as improvements compared with the 1931 CIE x,y,Y space. These are CIE LUV and CIE LAB.

2.3 Rare earths

Rare earths (RE) are elements with very similar chemical features, with an atomic number Z between 58 (Cerium) and 71 (Lutetium). The rare earths in solids are either divalent, trivalent or quadrivalent with the electronic configuration $4f^N 5s^2 5p^6$. The trivalent valence state is the most common in solids and is the valence state of interest in this work. An unique characteristic of the spectra of rare earth ions in ionic crystals is the sharpness of many lines in the absorption and emission spectra. These lines can be as narrow as those commonly observed in the spectra of free atoms or free molecules. These atomic-like spectra can be explained by looking at

the electronic configuration of the rare earth. In divalent and trivalent cases the 4f electrons are not the outermost ones. They are shielded from the external crystalline field by two electronic shells. Thus the 4f electrons are only weakly perturbed by changes in the surrounding ligands. An electronic shell in a solid is atomic-like the deeper its position is below the top of the valence band, which is the highest occupied level. Since the position of 4f states is at least 5 eV below the top valence band they can be considered with a good approximation *atomic-like*. For these states the crystalline field can be considered like a small perturbation in the atomic energy levels. Therefore to describe the energy levels of rare earth ions inside solids the wave functions of the free ions constitute a good zero order approximation for the description of rare earth ions in solids. The crystalline field contribution can be considered as a perturbation of the Hamiltonian of the free ions producing a splitting of the energy level.

2.3.1 Free ions

To interpret the levels of the free rare earth ion, the interaction between the $4f$ electrons and the other electronic shells is not taken into account, assuming this interaction is equal for each $4f$ electron in a spherical symmetry. This means it is not taken into account that the aspherical $4f$ (because it is nonclosed) shell can distort the closed spherical shell. For this limit, the Hamiltonian of the free rare earth ion can be written as:

$$H = T + V_{en} + V_{ee} + V_{so} = -\frac{\hbar^2}{2m}\sum_{i=1}^{n}\nabla_i^2 - \sum_{i=1}^{N}\frac{Ze^2}{r_i} + \sum_{i<j}^{n}\frac{e^2}{r_{ij}} + \sum_{i=1}^{N}\zeta(r_i)\vec{s_i}\cdot\vec{l_i}, \quad (2.8)$$

where the first term (T) is the kinetic energy of the electrons, the second (V_{en}) is their Coulomb interaction with the nucleus and the last two terms are the mutual Coulomb interaction between the 4f electrons and their spin-orbit interactions with

V_{ee} and V_{so} respectively. Since we have neglected the closed shells, Ze^2 is the screened of the charge of the nucleus, N = 1...14 is the number of the $4f$ electrons, $\vec{s_i}$ and $\vec{l_i}$ are the spin and the orbital momentum for the i-th electron, then $\zeta(r_i)$ the spin-orbit coupling function is:

$$\zeta(r_i) = \frac{1}{2m^2c^2}\left(\frac{\partial U(r_i)}{\partial r_i}\right), \tag{2.9}$$

where $U(r_i)$ is the potential in which the electron i-th is moving.

In systems with more than one electron it is not possible to obtain an exact solution for the Schröedinger's equation 2.8. The most common approximation for a complex atom is the central field approximation. In this approximation each electron is assumed to move independently in the field of the nucleus in a central field made up of the spherically averaged potential fields of each of the other electrons. The Hamiltonian H_{cf} for the central field is:

$$H_{cf} = \sum_{i=1}^{n}\left[-\frac{\hbar^2}{2m}\nabla_i^2 + U(r_i)\right] \tag{2.10}$$

where $U(r_i)$ is the central field potential and is composed of V_{en} and the spherical symmetric part of V_{ee}. Schröedinger's equation for the central field,

$$H_{cf} = \sum_{i=1}^{n}\left[-\frac{\hbar^2}{2m}\nabla_i^2 + U(r_i)\right]\Psi = E_{cf}\Psi \tag{2.11}$$

can be separated by choosing a solution like:

$$\Psi = \prod_{i=1}^{n}\Psi_i \quad \text{with} \quad E_{cf} = \sum_{i=1}^{n} E_i \tag{2.12}$$

The solution of the equation is the same as for the hydrogen atom (with the potential $-U(r_i)/e$ instead of $-e^2/r$):

$$\left[-\frac{\hbar^2}{2m}\nabla_i^2 + U(r_i)\right]\Psi(k_i) = E_{cf}\Psi(k_i) \tag{2.13}$$

where $(k_i\ )$ represents a set of quantum numbers (nlm_l) which specify the state of motion of the single electron in the central field. Being that all the terms in equation 2.13 are spherically symmetric, the degeneracy of the $4f$ electronic configuration:

$$\binom{2(2l+1)}{n} = \binom{12}{n}, \tag{2.14}$$

can not be removed.

Introducing polar coordinates and separating the one electron eigenfunctions into radial and angular parts the solution becomes:

$$\Psi(k_i = (r_i,\theta_i,\varphi_i)) = \frac{R_{nl}(r_i)}{r}Y_l^{m_l}(\theta_i,\varphi_i) \tag{2.15}$$

where $Y_l^{m_l}(\theta_i,\varphi_i)$ are the spherical harmonic functions and $R_{nl}(r_i)$ the radial functions, the solution of equation 2.13 is then:

$$\Psi = \sum_{i=1}^{N}\Psi(k_i) \tag{2.16}$$

This solution is not unique since other solutions may be obtained by permutations of the coordinates of any of the N-electrons. To satisfy the Pauli exclusion principle we must choose a linear combination of these solutions to obtain antisymmetric wavefunctions with respect to the permutation of spin and spatial coordinates of any pair of electrons. The resulting antisymmetrical solution of the central field wave equation may then be written as:

$$\Psi = \frac{1}{\sqrt{N!}}\sum_{i=1}^{N}(-1)^p P\Psi_1(k_1)\Psi_2(k_2)\ldots\Psi_N(k_N) \tag{2.17}$$

where P represents a permutation of the electrons and p is the parity of the permutation with the summation extending over all the permutations of the N-electron coordinates. At this level the principal quantum number n, the orbital angular momentum l and its component along the quantization axis m_l are good quantum numbers.

To obtain the rare earth energy level structure we have to investigate also the non spherically symmetric part: $V = H - H_{cf}$. This potential splits the highly degenerate free ion states, and the energy levels can be found calculating the matrix elements of V . Unfortunately, such an approach assumes a large amount of calculations and fails to solve the problem of labelling the energy levels. In atomic theory there are two limiting cases: $H_c \gg H_{so}$ and $H_c \ll H_{so}$. The first is the Russell-Saunders coupling, the spin-orbit is considered like a small perturbation in the energy level scheme that is obtained diagonalizing the H_c term. The second is called j - j coupling and the H_c results from a perturbation to the energy level scheme. Both cases can be solved by the perturbation theory. In rare earth ions these two terms are comparable and this regime is called intermediate coupling.

To calculate the energy levels in the intermediate coupling approximation we have to calculate the matrix element for the V potential in a set of basis functions and diagonalize the matrix for the specific $4f$ configuration. Usually a basis set of Russel-Sanders eigenfunctions is used. The V is diagonal in J, and therefore the total matrix of energies for the $4f^N$ configuration can be split up into submatrices for states with the same J. These states are then still degenerate in M_J and are a linear combination of states with different L and S but the same J. There are also configurations with the same L and S that occur more than once; to distinguish them, new quantum numbers must be introduced.

2.3.2 Rare earth in the crystal field

In order to define the energy level structure of rare earth ions inside a crystal, the interaction with the crystalline field must be taken into account. Two different ways have been used to solve this problem: by means of the ligand field theory introduced by Ballhausen [42], and the crystal field theory introduced by Bethe [37]. The first theory supposes that the interaction between the ions and the surrounding environment is predominant creating molecular orbitals with the surrounding ions. Since we are focused on the $4f$ orbitals, that are not the most external ones, this way is not applicable, but it is useful for the $3d$ valence-shell of transition metals. Consequently, the interaction between the rare earth ions and the crystalline field will be approached considering the potential provided by the crystal environment (V) as a perturbation that removes partially or totally the degeneracy of the component of J along the quantization axis. The new sublevels are named Stark levels.

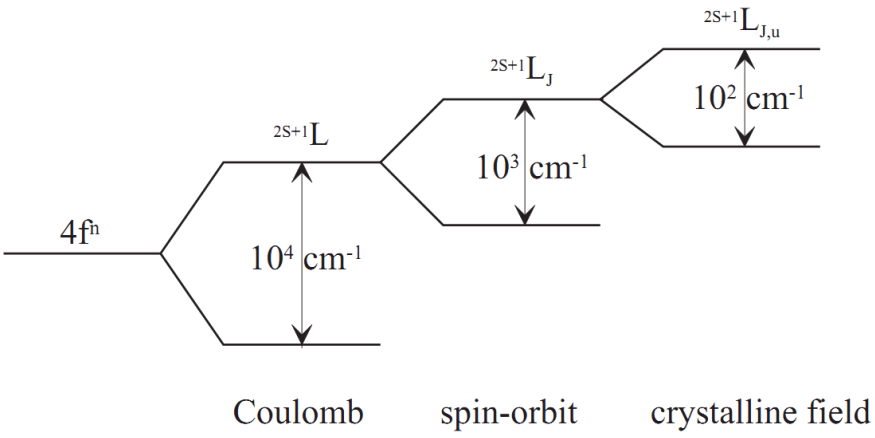

Figure 2.5. Typical values or the level splitting in rare earth ions.

In Figure 2.5, we report the typical order of magnitude of energy level splitting inferred from absorption and emission spectra that are characterized by relatively narrow and well separated bands made up of several distinct absorption or emission

peaks which correspond to the Stark sublevels. Considering the crystal field is generated by the superposition of the electrostatic potential of the other ions, it is assumed V may be expanded in terms of spherical harmonics:

$$V = \sum_{q,k,i} B_q^k C_q^k(i) \tag{2.18}$$

where the summation involving i is over all the electrons of the ions of interest. The quantities B_q^k can be seen as a simple coefficient of the expansion, determinable empirically from the experimental data. The first term of eq. 2.18 has $k = q = 0$ and is thus spherically symmetric. In a first approximation this term gives a uniform shift of all the levels of the configurations. When only f-electrons are involved, group theory and punctual symmetry determine $k \leq 6$. Since the Hamiltonian must be invariant under the operations of the point symmetry group, the values of k and q are limited by the point symmetry of the rare earth ion site [43].

The degree to which the $(2J + 1)$ fold degeneracy is removed will depend on the point symmetry about the rare earth ion. The Kramer theorem demonstrates that for an odd number of electrons, what ever the punctual symmetry, every Stark sublevel is at least two-fold degenerate due to the Hamiltonian symmetry for temporal inversions. Since the odd part of the crystalline field causes a little mixing of various sublevels with different quantum numbers n, the electronic transitions between $4f$ electrons, parity forbidden, become partially allowed. The rare earth ions reach excited states showing radiative transitions with very long decay times up to tens of milliseconds: such a phenomenon suggests one to adopt the name of metastable levels for these relatively long lived states. The scheme of the energy levels (Dieke scheme) for all triple-ionized rare earth ions is shown in Figure 2.6.

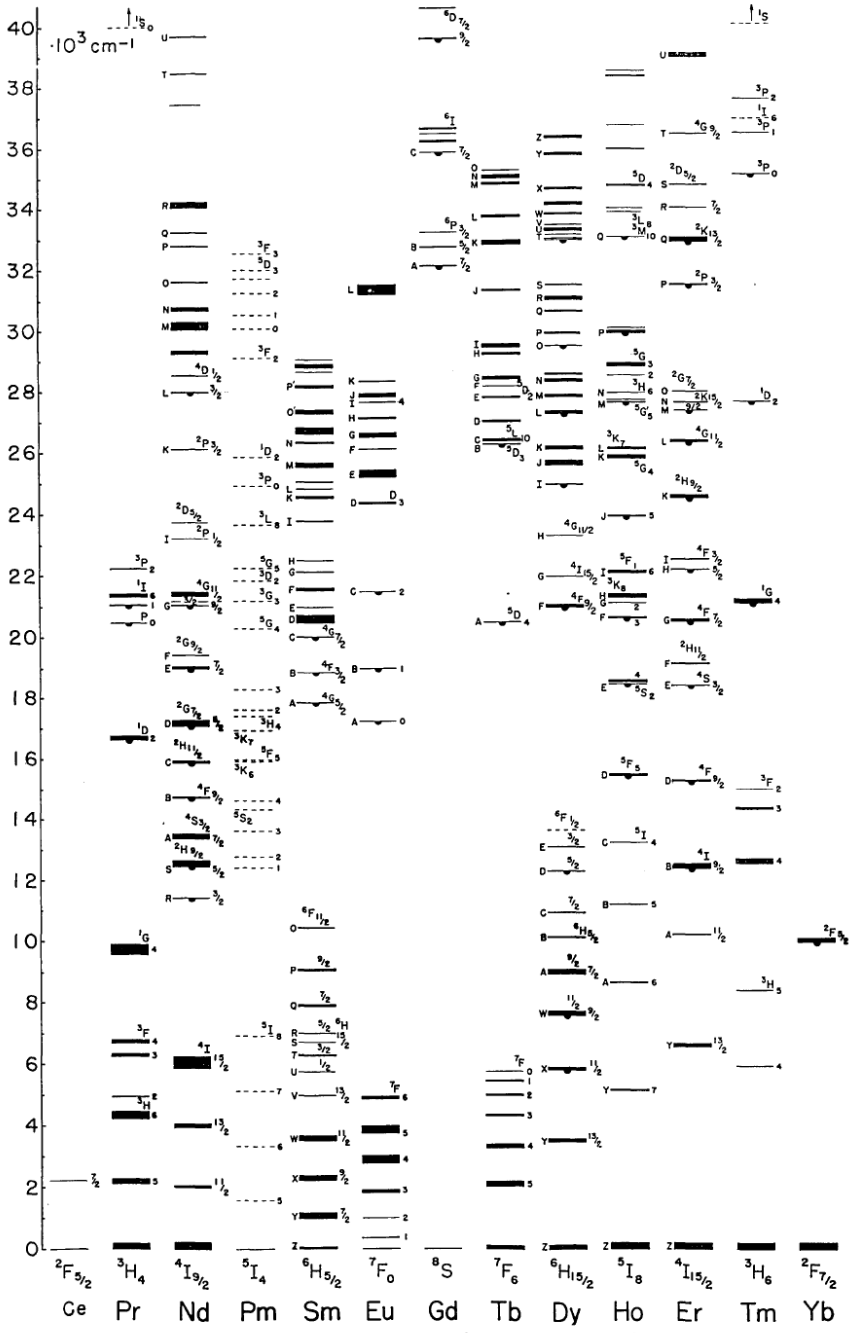

Figure 2.6. Scheme of the energy levels of all triply ionized rare-earth ions [44].

2.4 Energy transfer in rare earth doped crystal

The three main categories for the energy transfer among energy levels of the same ion or different ions of rare earth doped crystals are:

- radiative relaxation;
- non-radiative relaxation;
- cooperative mechanisms.

The life time of an excited multiplet a can be expressed as:

$$\tau_a = \frac{1}{\sum_b W_{ab}^R + W_{ab}^{NR}} \tag{2.19}$$

where the index b runs on the final states, W_{ab}^R is the radiative decay rate and W_{ab}^{NR} represents the rate for non-radiative decays and cooperative mechanism between ions.

2.4.1 Radiative relaxation

A decay is radiative if there is emission of photons from an excited state that decays to an other one. A fast thermal equilibrium (10^{-12} s 10^{-13} s) among the different Stark sublevels of a manifold permits to consider the initial manifold as a single level. The spontaneous emission rate between the starting Ψ_i and the final level Ψ_f is expressed by the A_{fi} Einstein coefficient:

$$A_{fi} = \frac{64\pi^4 \nu_{fi}^3}{3hc^3 g_i} |\langle \Psi_f \left| P \right| \Psi_i \rangle|^2 \tag{2.20}$$

where ν_{fi} is the frequency of the transition, g_i is the degeneracy of the starting level and P represents the operator responsible for the transition. All the transitions under investigation occur between electronic levels of the same configuration

$4f$: these decays would not be allowed in the electric dipole approximation due to the parity selection rule. The magnetic dipole and electric quadrupole induced transitions (free from parity selection rule) are not able to explain the complexity and the intensity of the experimental spectra. The weak oscillator strengths and other experimental evidence suggest that the transitions occur due to induced dipoles produced by the influence of the crystal field, by means of its odd components that mix 4f states having different parity. A further contribution to the decay rate that can be treated as a correction arises because of lattice vibrations: due to the coupling with the electronic levels vibrational side bands appear. Following the Born-Oppenheimer approximation it is possible to write the wavefunction as the product of an electronic part and a vibronic one:

$$\Psi = \Psi_e \Psi_v \tag{2.21}$$

the vibronic part adds a factor to the emission rate that takes into account the phonon effective density of states $\mathrm{D}^*(\nu_{if})$:

$$A_{fi} \propto \langle \Psi_f \left| P \right| \Psi_i \rangle \frac{D^*(\nu_{if})}{\nu_{if}^3} \tag{2.22}$$

Those vibrational side bands correspond to transitions between the fundamental vibrational state of the excited level and the excited vibrational states of the low lying electronic level: they are less energetic than the purely electronic transition (the so called zero phonon line) and are observed at longer wavelength; as the temperature increases the vibrational levels of the excited state become populated and sidebands appears even at wavelengths shorter than the zero phonon line. The intensity of those sidebands is a measure of the strength of the coupling with the phonon field.

2.4.2 Non radiative relaxation

In the case of non-radiative decays the excitation energy is released to the crystalline lattice as phonons. To describe this process I refer to ref [45, 46]. Evidence of non-radiative decay is the shortening of the decay time of the excited levels as the energy gap between them decreases, till the extreme case, in which the fluorescent signal is completely quenched if levels are close enough. Considering the ions as a point charge, it is possible to expand the crystal field Hamiltonian H_{cf} in a Taylor series around the equilibrium ion position as:

$$H_{cf} = V_{cf} + \sum_i \frac{\partial V_{cf}}{\partial Q_i} Q_i + \frac{1}{2} \sum_{ij} \frac{\partial^2 V_{cf}}{\partial Q_i \partial Q_j} Q_i Q_j \tag{2.23}$$

where V_{cf} is the static crystal field of equation 2.18 and Q_i represents the i-th normal mode coordinate; experimental data allow us to adopt the approximation up to temperatures of several hundreds of ^{0}C. Since the cut-off of the phononic spectrum is of the order of hundreds of cm^{-1} (the maximum is reached in oxide crystals with 1000 cm^{-1}), non-radiative relaxation must involve many phonons. Presently equation 2.23 can only give an order of magnitude because of the uncertainties or lack of knowledge of the terms in equation 2.23. To calculate the non radiative decay rate a single-frequency phonon model with weak electron-phonon coupling is used. Assuming the weak phonon-electron coupling and using the energy conservation it is possible to write:

$$\Delta E_{gap} p_i \hbar\omega_i \qquad \frac{W^p}{W^{p-1}} = \epsilon \ll 1 \tag{2.24}$$

p_i is the number of phonons necessary to bridge the energy gap ΔE_{gap} to the next-lowest level having frequency ω_i. Defining n_i as the occupation number of the i-th phonon mode and W_0 as the low temperature transition rate ($W(T=0) = W_0$), the dependence of the non radiative decay rate from the temperature can be written as:

$$W(T) = W_0(n_i + 1)^{p_i} \tag{2.25}$$

Since phonons are bosons, we can substitute n_i with the corresponding Bose-Einstein distribution:

$$n_i = \left[exp\left(\frac{\hbar\omega_i}{kT}\right) - 1 \right]^{-1} \tag{2.26}$$

that can be replaced in the equation 2.25

$$W(T) = W_0 \left[\frac{exp\left(\frac{\hbar\omega_i}{kT}\right)}{exp\left(\frac{\hbar\omega_i}{kT}\right) - 1} \right]^p \tag{2.27}$$

In Figure 2.7 we show the temperature dependence of the rate for different orders of the process as from equation 2.27. The hypothesis of single-energy phonons seems reasonable because the most important parameter is the number of phonons involved in the relaxation rather then their precise energy.

In the previous model the degeneracy of each manifold was neglected. If a is the index for the Stark sublevels of the upper multiplet and b that for the lower ones, and assuming the validity of the Boltzmann distribution in every manifold,the corrected rate reads:

$$W(T) = \frac{\sum_a \sum_b W_{ab}(T) g_a exp\left(-\frac{\Delta_a}{KT}\right)}{\sum_a g_a exp\left(-\frac{\Delta_a}{KT}\right)} \tag{2.28}$$

where W_{ab} is the rate for the decay from the upper multiplet sublevel a to the lower multiplet sublevel b, g_a is the degeneracy and Δ_a is the energy of the a level of the upper state measured from the bottom of the upper manifold. The multiphonon decay experimentally shows a dependence on the energy gap between the two manifolds involved in the transition. This can be explained with the convergence of the perturbative expansion guaranteed by equation 2.24 that leads easily to:

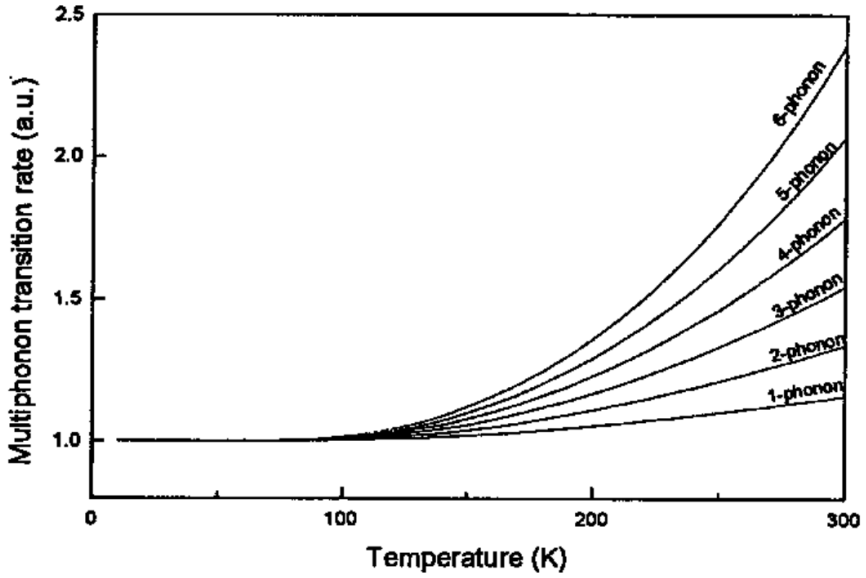

Figure 2.7. Multiphonon relaxation rate as a function of the temperature for different number of phonons.

$$W^n = A\epsilon^n \tag{2.29}$$

with A a constant and n determined by equation 2.24, gives the phenomenological expression:

$$W = \epsilon^{\frac{\Delta_{gap}}{\hbar\omega_{max}}} = Ce^{-\alpha\Delta E_{gap}} \tag{2.30}$$

The values of α and C depend on the crystalline host, where C is measured in the range of $10^{-12} - 10^{-13}s^{-1}$, as previously stated. Experimental evidences of the validity of equation 2.30 can be seen in Figure 2.8.

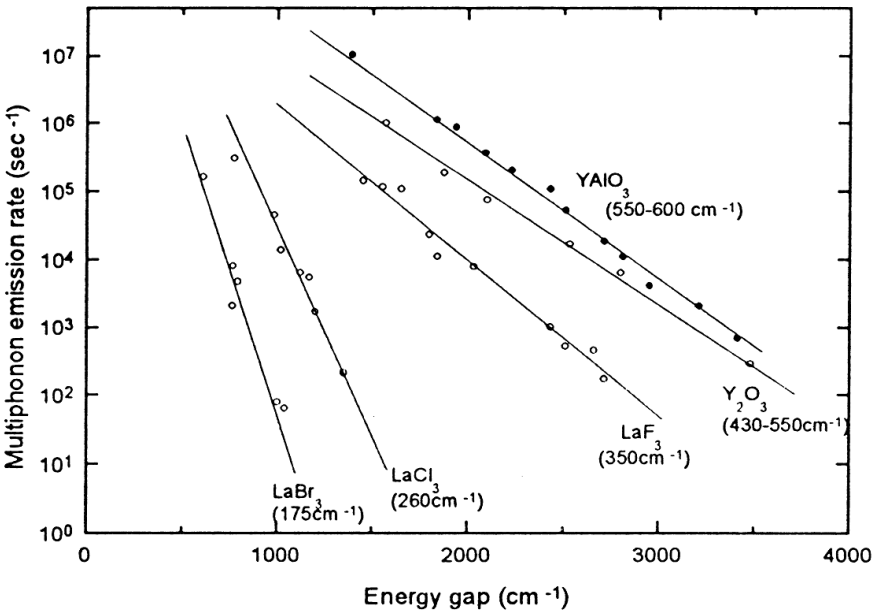

Figure 2.8. Multiphonon relaxation rate as a function of the energy gap in different matrices.

2.4.3 Cooperative mechanisms

When the dopant concentration increases, the relaxation mechanism cannot be described as single particles processes. As ions get spatially closer to one another, a coupling process could happen via exchange interactions in the case of wavefunction overlapping, via super-exchange interactions when intervening ions are involved, or via electro-magnetic multipolar interactions. The excitation can be transferred between two ions called *donor* and *acceptor* respectively. Since the decay-times are so long, different mechanisms of energy transfer, which could not take place if the lifetime of the excitations were not long, enough, are allowed. Historically, Förster [47] and Dexter [48] laid out the basics of the theory for the energy transfer in rare earth doped crystals. After them various theoretical methods were developed in order to describe the mechanisms that take place in samples of this kind. Omitting the lattice-ion interaction, the energy transfer rate W_{AB} between the ions A and B is

expressed as:

$$W_{AB} = \frac{2\pi}{\hbar}|\langle\Psi_A(2')\Psi_B(1')|H_{int}|\Psi_A(2)\Psi_B(1)\rangle|^2 \int f_A(E)f_B(E)dE \tag{2.31}$$

where H_{int} is the ion-pair coupling Hamiltonian, $\Psi_A(2)$and $\Psi_B(1)$ are the initial states, while$\Psi_A(2')$ and $\Psi_B(1')$ are the final ones and $f_A(E)$ and $f_B(E)$ represent the normalized line-shape functions for the transitions of ions A and B Figure 2.9. In the case of electrostatic interactions between electronic clouds of the two ions A

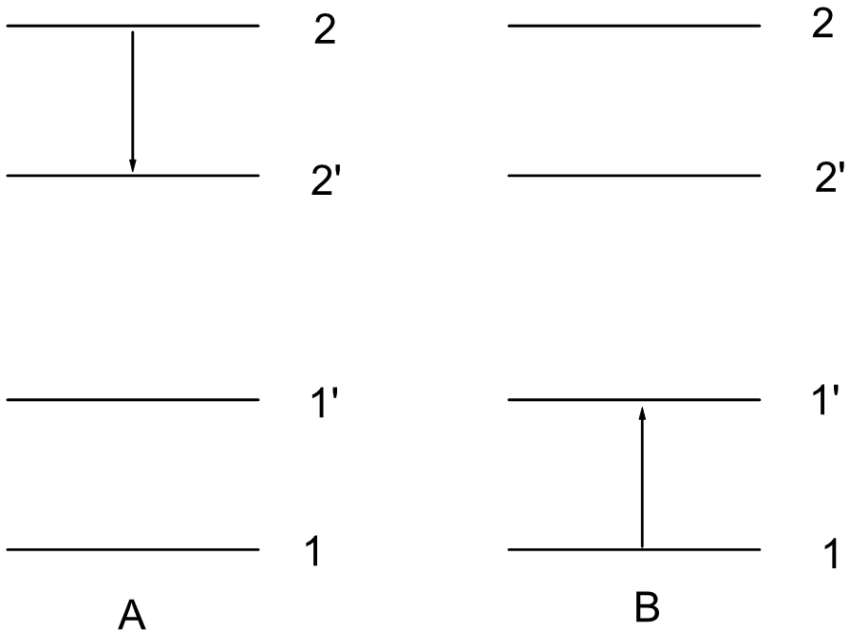

Figure 2.9. Cooperative relaxation.

and B, H_{int} can be written as:

$$H_{int} = \frac{1}{\epsilon}\sum_{i,j}\frac{e^2}{R - r_{A,i} + r_{B,j}} \tag{2.32}$$

where ϵ is the dielectric constant of the medium, $r_{A,i}$ and $r_{B,j}$ represent the coordinate vectors of the i-th electron with respect to donor A and the j-th electron with respect to acceptor B, and R is the inter nuclear separation A - B.

The equation 2.31 can be expanded in spherical harmonics around the equilibrium position of the ions, obtaining:

$$H_{int} = \frac{1}{\epsilon} \sum_{k_i,k_j} \sum_{q_i,q_j} \frac{e^2}{R^{k_i+k_j+1}} G^{k_i,kj}_{q_i,q_j} D^{k_i}_{q_i}(A) D^{k_j}_{q_j}(B) \tag{2.33}$$

where $G^{k1,k2}_{q1,q2}$ is a factor that takes into account the orientation of the crystallographic axes with respect to the incident light and D^k_q is the multipole operator defined as:

$$D^k_q = \left(\frac{4\pi}{2k+1}\right)^{\frac{1}{2}} \sum_i r^k_i Y_{kq}(\theta_i,\phi_i) \tag{2.34}$$

The leading terms of equation 2.33 are the electric dipole-dipole, dipole-quadrupole and quadrupole-quadrupole having radial dependencies of R^3, $\mathrm{R}^4$and R^5 respectively. A more detailed description takes into account the contribution for the magnetic dipole:

$$H_{md} = \sum_{i,j} \left[\frac{\vec{\nu_i} \cdot \vec{\nu_j}}{R^3} - \frac{3(\vec{\nu_i} \cdot \vec{R})(\vec{\nu_j} \cdot \vec{R})}{R^5} \right] \tag{2.35}$$

where $\vec{\nu_i} = \vec{l_i} + 2\vec{s_i}$.

As a result, the contribution of the electromagnetic terms to W_{AB} of equation is:

$$W^{em}_{AB} = \frac{a^{d-d}}{R^6} + \frac{a^{d-q}}{R^8} + \frac{a^{q-q}}{R^{10}} + \ldots \tag{2.36}$$

Since *ab initio* calculation are not possible. The coefficients a are left as phenomenological parameters that must determined experimentally.

Besides the electromagnetic interactions, the exchange mechanism can be represented by:

$$H_{ex} = \sum_{i,j} J_{i,j} \vec{S_i} \cdot \vec{S_j} \tag{2.37}$$

where $\vec{S_i}$ and $\vec{S_j}$ are the spin moments of the two ions and $J_{i,j}$ is the exchange integral. Using hydrogen-like wavefunctions to perform the calculations, it is possible to express the radial dependence as:

$$W_{AB}^{ex} \propto exp(-2R_0)/L) \tag{2.38}$$

where L is an effective Bohr radius and R_0 is the distance where the exchange interaction is equal to the radiative de-excitation. As the ion-lattice coupling is considered, the processes can also be non-resonant and require the creation or destruction of phonons. The different processes are presented in Figure 2.4.3 and can be classified as:

- **Migration**: the transfer of the energy from an excited ion to another one. A previously excited ion relaxes and transfers its energy to another one. This process can occur either between two ions of the same kind or between two different ones. Moreover it can be a resonant transfer or a non-resonant one (i.e. a transfer involving one or more phonons).

- **Cross-relaxation:** in this process an ion decays from an excited state to another one (with the exception of the ground state!) and transfers the energy to another ion, usually of the same kind. As a result, at the end of the process, two ions are excited and the sum of their energy is equal to the initial energy. This process can also involve phonons. In this case, the conservation of the energy is still fulfilled provided that one takes into account the phonon energy.

- **Up-conversion:** this process happens when two excited ions, usually of the

same kind, transfer their energy resulting in an ion which will acquire the sum of the energy of the previous ones. Also in this case one or more phonons can be involved in the transfer. This process is used to produce visible light by IR-diode pumping using Yb as the donor and Pr, Er, Tm and Ho as the acceptor in different materials.

- **Excited state absorption (ESA)** this takes place when an excited ion absorbs the pump radiation thus reaching a higher level, even if it is not an energy transfer process between ions inside the crystals.

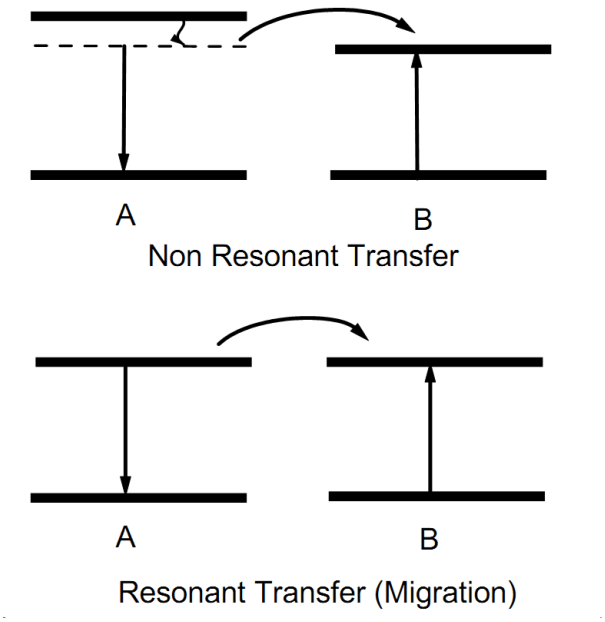

(a) Resonant transfer (migration) and non-resonant transfer.

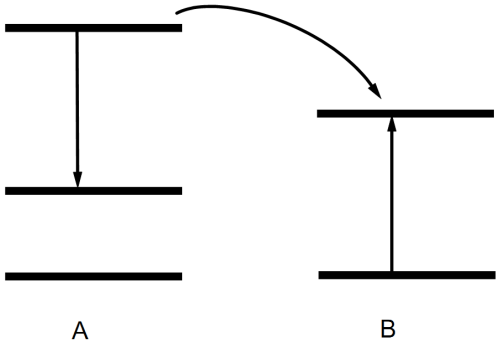

(b) Cross-relaxation

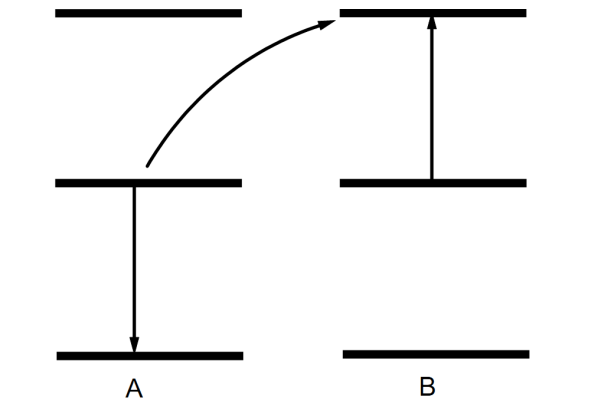

(c) Up-conversion

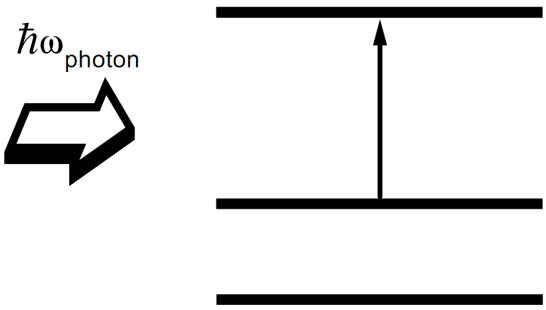

(d) Excited state absorption (ESA)

Figure 2.10. Schemes representing the various energy transfer mechanisms.

Chapter 3

Experimental apparatus and crystals

3.1 Crystals

During this work, I analysed different fluoride and oxide crystals with cubic, monoclinic, and uniaxial structure doped prevalently with trivalent Pr ions. All the fluoride crystals studied have been grown in the Pisa NMLA laboratories using the Czochralski method [49]. A lot of information about the crystal structure and the growth method can be found in the literature, but for the sake of clarity some general data about the growth method will be reported in the following section. In order to investigate polarization-dependent optical properties the crystals were oriented by X-Ray Laue technique, then cut and optically polished with alumina powder.

The oxide crystals analysed in this work were grown by the E. Cavalli et. al. in the University of Parma, using the flux growth methods, some generals details about the growth were reported in the following sections. Due to the small dimension of the sample, compared with the CZ boules, the oxides were used directly in the spectroscopic measurements, without cutting and polishing the surface. Obviously

the crystals were oriented using the X-ray back scattering technique, in order to perform polarized investigation.

3.2 Czochralski growth method

As mentioned before, all the fluoride investigated crystals were grown by the Czochralski method. Appropriate powders, depending on the crystalline matrix, are inserted in a furnace with resistive heating. When the melting point temperature of the mixing powders is achieved, a seed crystal is brought into contact with the melt. The growth continues pulling upwards and rotating the seed at the same time. The vertical growth against the gravitational force and the rotation of the seed are the main difference between the Czochralski and other growth methods. The used growth apparatus is completely home-made at ours laboratories. Depending on the crystal that is grown, crucibles of different materials are used in order to avoid any chemical reaction with the molten powders. The growth powders were purified at AC Materials (Orlando, FL) to a purity of 99.999%. During the growth to avoid any contamination that can affect the optical quality of the crystal, special care has been devoted to the quality of the vacuum before the growth starts, which has an ultimate pressure limit below 10^{-7} mBar. The growth process was carried out in a high-purity (99.999%) Argon atmosphere. The furnace is equipped with an optical computer-controlled apparatus for diameter control. The single crystalline character of the samples was checked, after the growth, using the X-ray Laue technique that allows us to identify the crystallographic axis of the crystal and to cut oriented samples.

3.2.1 BaY_2F_8

BaY_2F_8 (BYF) has a monoclinic crystalline structure with C2/m space group [43]. Due to this structure BaY_2F_8 is an optically anisotropic media (biaxial). Based on [50] the average refractive index n is about 1.5 around 578 nm. The reticular constants are a = 6.972 Å, b = 10.505 Åand c = 4.260 Å, the angle between the a-axis and the c-axis is $\beta = 99.4°$ [51] see Figure 3.1; each primitive cell contains two molecules of BaY_2F_8 .

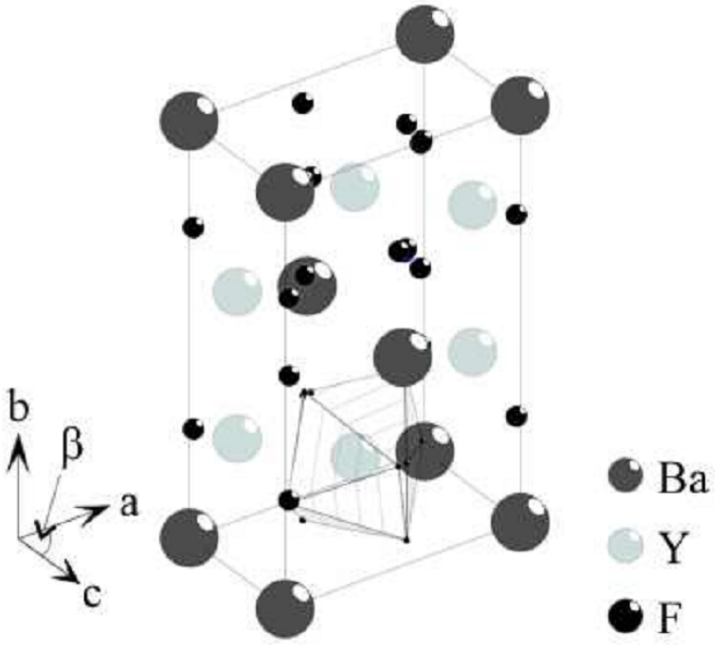

Figure 3.1. View of the unit cell of BaY_2F_8 . The polyhedron defined by the surrounding fluoride ligands of an Y^{3+}-ion is marked [50].

Rare earth ions enter the Y^{3+} sites having C_2 symmetry, therefore the crystal field completely removes the degeneracy of the levels of the ions with an even number of electrons in the $4f$ shell. Since the ionic radius of Y^{3+} (1.26 Å) is smaller than the Pr^{3+} one (1.27 Å), the distribution coefficient is less than 1. In the BaY_2F_8 crystals

the Pr^{3+} distribution coefficient k_{seg} runs from 0.4 to 0.5. The principal structural and optical BaY_2F_8 properties are reported in Table 3.2.5 ([52, 53, 54]). One of the most important features of this crystal is the large transparency window that ranges from the UV (200 nm) up to the IR (9 μm) region, and the very low phonon energy (≤ 350 cm^{-1} [52]) that makes this matrix suitable for laser applications in the near IR region, as well as in the UV and visible regions.

Five Pr^{3+} nominal doping levels on BaY_2F_8 crystal matrix are studied in this work: 0.3%, 0.5%, 1.25%, 2% and 3% (atomic concentration refereed to the raw material concentration). All of them were grown using BaY_2F_8 powder as raw material for the crystal and the doping density was achieved by adding a proper amount of PrF_3 powder. A 1% Sm^{3+} and 1% Eu^{3+} samples were growth and in order to investigate the behaviour of these dopants.

3.2.2 KYF_4

KYF_4 structure has been studied by Aléonard et al. [55]. KYF_4 has a trigonal non-antisymmetrical structure with space group $P3_1$. KYF4 like $NAYF_4$ derives from the basic CAF_2 structure [56, 57]. The cell parameters are a = 14.060 Å, c = 10.103 Å and the cations are arranged in an abc sequence perpendicular to the c axis [58, 59]. In the literature, we can and two different theories about the position of cations in the unit cell. KYF_4 has either been considered as a multiple host material [58, 60, 61, 62] or a disordered crystal [63]. Recently it has been proven [64] that KYF4 has a multiple structure where some of the sites in the unit cell are occupied either by Y^{3+} or K^+ in a statistical manner. According to [58, 59, 65, 66] two main classes of sites exist but the number of their subclasses varies for every class from two to three and up to five. These can depend on the different rare-earth ion doping, for example some authors state that for the Er doping ions only a class of sites is occupied [67]. A cation plane of the KYF_4 unit cell is shown in Figure 3.2.

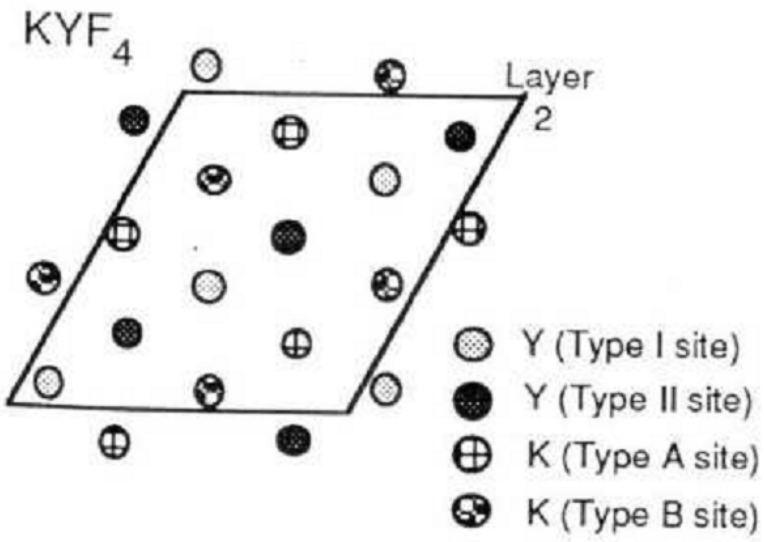

Figure 3.2. Structure of KYF_4 [58]. The illustration is the z = 1/3 cation plane projected along c.

Two different samples from the same grown bulb were investigated, to check the dependence of the CIE coordinates and of the efficiency from the dimensions of the crystal. The larger sample is 10.6 x 3.01 x 2.35 mm^3 (w x l x h) and the crystallographic axes c and a are along l and h respectively. The smaller sample is 4.94 x 4.40 x 2.79 mm^3 (w x l x h) with the a and c axes directed along h and l, respectively. The volume of the larger is 74.98 mm^3 , whereas the smaller one is 60.64 mm^3.

3.2.3 KY_3F_{10}

KY_3F_{10} is an isotropic crystal with a cubic-face-centred structure Fm3m (O_h^5) similar to the fluorite structure. The elementary cell contains eight formula units and has a cell parameter a = 11.54 Å. The trivalent rare-earth dopants substitute for the Yttrium ions in sites of C_{4v} symmetry [68] (Figure 3.3). Like in the BaY_2F_8 case its

distribution coefficient is less than one. It was determined by ICE-OEM- and AA-measurements to be $k_{seg} = 0.5$. The melting point is around 1030°C. The properties of this crystalline host are reported in Table 3.2.5 [53, 69].

The sample investigated in this thesis is 0.3 at.% Pr^{3+} nominal doped. Its dimension are 3.37 x 3.9 x 3.39 mm^3 (wxlxh). The crystalline axis a is directed along each side.

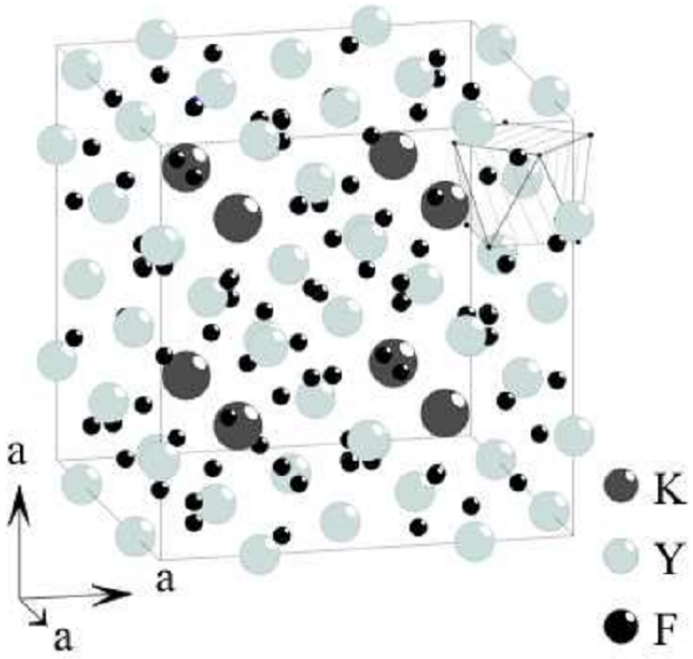

Figure 3.3. Scheme of the unit cell of KY_3F_{10} crystal. The polyhedron defined by the surrounding fluoride ligands of an Y^{3+}-ion is marked.

3.2.4 $LiLuF_4$

The $LiLuF_4$ (LLF) crystal is an isomorph to the well known $LIYF_4$ (YLF) and therefore belongs to the tetragonal system with C_{4h}; $I4_{1/a}$ symmetry. The lattice parameters are a = b = 5.167 Å and c = 10.375 Å. In the $LiLuF_4$ crystal the rare

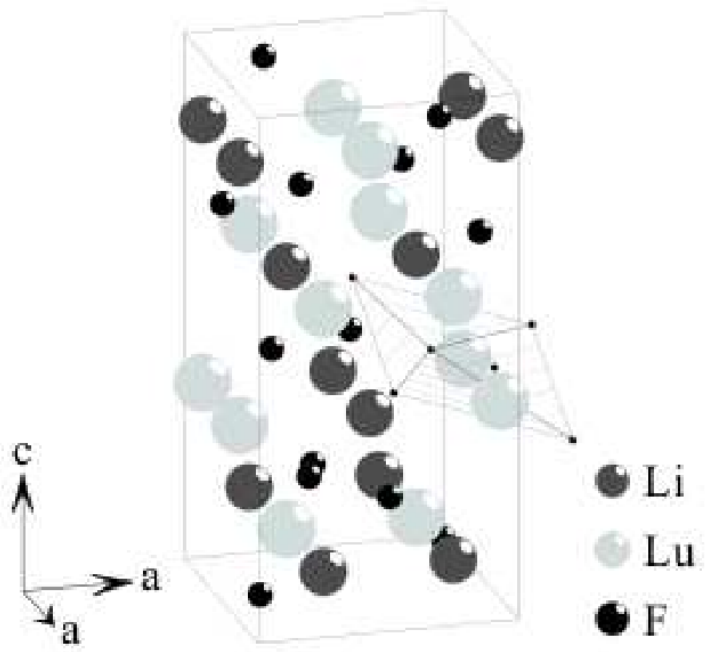

Figure 3.4. View of the unit cell of $LiLuF_4$. The polyhedron defined by the surrounding fluoride ligands of an Y^{3+}-ion is marked [70]

earth ions substitute the Lu^{3+} ions in sites with S_4 symmetry with coordination number equal to 8 [71, 72](Figure 3.4). The Lu^{3+} (1.12 Å) ion is very small compared to the Pr^{3+} (1.27 Å) ion, and this causes an enhanced possibility for crystal distortions and a low distribution coefficient (0.1 - 0.2). The melting temperature of $LiLuF_4$ is $\sim$ 830°C. In Table 3.2.5 the main optical and structural features are reported [73, 53].

Three samples of $LiLuF_4$ with different nominal doping levels (0.5 at.%,1.25 at.%,2 at.%) are investigated for the white light emission

3.2.5 $LiYF_4$

$LiYF_4$ is is an insulating crystal with a tetragonal structure like the Scheelite ($CaWO_4$): this means that it is uniaxial. Its transparency region extends from the visible up to infrared ($\approx$ 5 μm). This crystalline host is now widely used in commercial devices (even operating at high power), and it has been used as an active laser medium when doped with almost all rare earth ions, because of its low index of refraction (n_σ = 1:45 when E $\perp$ c and n_π = 1:47 when E $\parallel$ c at 1000 nm), low phonon energies and negative coefficient for thermal lensing. The symmetry group is $C_{4h}^6(I4_1/a)$ [74]. The primitive cell has four molecules and its dimensions are: a=b=5.160 Å, c=1.085 Å; rare earth ions substitute Y^{3+} site, that has point symmetry S_4. A 8%at Tm doped crystal was growth in order to investigate a Passive Q-switching laser pumped by a laser diode.

Table 3.1. Summary or the Pr-studied crystals [75, 64, 68, 71]

Host	Symmetry	cell parameter	Pr^{3+} doping (at.%) levels	dimension (mm)	label
BaY_2F_8	monoclinic	a=6.972 Å	0.3	1.5 x 4.3 x 7.1	A
		$b = 10.505$ Å	0.5	10.1 x 3.03 x 1.64	B
		$c = 4.260$ Å	1.25	10.2 x 4.0 x 4.5	C
		$\beta = 99.4$	2	4.36 x 3.97 x 2.29	D
			3	11.6 x 2.7 x 4.2	E
$LiLuF_4$	tetragonal	$c = 10.375$ Å	0.5	11.17 x 3.93 x 2.95	F
		$a = b = 5.167$ Å	1.25	2.8 x 6.4 x 8.7	G
			2	4.67x3.74x1.19	H
KYF_4	trigonal	$a = 14.060$ Å	1.25	10.6 x 3.0 x 2.3	I
		$c = 10.103$ Å		4.9 x 4.4 x 2.8	L
KY_3F_{10}	cubic	$a = 11.535$ Å	0.3	3.4 x 4.0 x 3.4	M

3.3 Flux growth methods

3.3.1 YPO_4

YPO_4 crystals doped with 0.5, 3 and 10% Dy (molar ratio with respect to Y) were grown by the 'flux growth' technique using $Pb_2P_2O_7$ as a solvent in the 1300-800 °C temperature range [76]. Their tetragonal structure was confirmed by means of single-crystal x-ray diffraction. In agreement with literature data, the space group is $I4_{1/amd}$ with Z = 4 [77, 78]. The cell parameters are a = 6.894 Å, c = 6.293 Å. The Dy^{3+} doping ions enter the Y^{3+} sites having eightfold oxygen coordination and D_{2d} point symmetry. The zircon-type structure of the title compound can be described as built from chains of alternating edge-sharing PO_4 tetrahedra and YO_8 dodecahedra (bisdisphenoids) extending parallel to the crystallographic **c** axis and joined laterally by zigzag chains parallel to the **a** axis.

3.3.2 $Ba_2NaNb_5O_{15}$

Single crystals of BNN singly doped with Pr^{3+} were grown by means of the 'flux growth' method. Pure BaO, Nb_2O_5 and $Na_2B_4O_7$ were used as starting materials. The doping ions were added as Pr_6O_{11} with nominal 0.5%, 2% and 8% molar ratios with respect to Ba. The starting mixture was placed in a Pt crucible and heated to melt (1250°C) in a horizontal furnace. After a 12 h soaking time, the temperature was slowly lowered (2-3°C$\times$ h^{-1}) to 400 °C, then the furnace was turned off. Crystals with size up to of 2 x 2 x 3 mm^3 and of sufficient optical quality were separated from the flux by dissolving it in hot diluted HCl.

The structural properties of the grown crystals will be discussed in detail in chapter 6. For the moment it is sufficient to point out that the incorporation of Pr^{3+} ions into the BNN lattice requires charge compensation that, combined with the intrinsic disorder of the TTB structure, results in the formation of different

non-equivalent optical centres and a significant inhomogeneous broadening of the absorption and emission features.

3.4 Experimental apparatus

In this section the experimental apparatus that was used for the analysis of the previously described crystals as new white light emitting sources is briefly describe.

3.4.1 X-Ray crystal orientation

All the samples under investigation, except the KY_3F_{10} one, are not cubic and, consequently, their spectroscopic features have to be studied as a function of the crystal orientation. The samples have been oriented using the Laue method. The X-ray source is a HAT Generator PW1830/40 and a Copper tube 38 Experimental apparatus and crystals PW2273/30 by Philips. The X-rays are emitted through a Beryllium window with no selection of the output wavelength. They scatter on the sample mounted on a precision goniometer ($\pm$ 0.1^0 in the x and y directions and $\pm$ 0.2^0 along z) and the Laue diffraction pattern is acquired in back-refraction scheme by means of a photographic plate and a Laue chamber (Flat Chamber 801 by Huger). The image is then digitalized using a scanner and analysed using the Orienting program. From this procedure it is possible to individuate the crystallographic axes and cut the crystals along their directions.

3.4.2 Crystals preparation

To use the oriented crystals for the spectroscopic investigation each fluorides sample was mechanically cut and polished . To cut the crystals with the desired orientation and dimensions a precision cutter with a diamond wire is used. The polishing of the sample surfaces is performed using alumina and diamond powders of decreasing

diameters. The optical quality of the obtained samples is tested by observing with a microscope the scattering of visible light. The polishing procedure has to be carefully carried out in the case of laser samples since the quality of the polished surfaces can affect the performance of the conversion efficiency of the crystals.

3.4.3 Absorption measurements

The acquisition of the room temperature absorption spectra have been performed by means of a two beam spectrophotometer VARIANT CARRY 500 operating in the range 180-3200 nm. The signal on the UV-Vis region is obtained using a 1200 gr/mm grating and a R928 photomultiplier as a detector. The dispersion is 0.98 nm/mm. A 300 gr/mm grating and a cooled PbS photodiode are used for the NIR part of the spectrum with a dispersion of 3.92 nm/mm. The grating change is automatic at 800 nm. Figure 3.5 shows a scheme for the CARY 500 spectrophotometer.

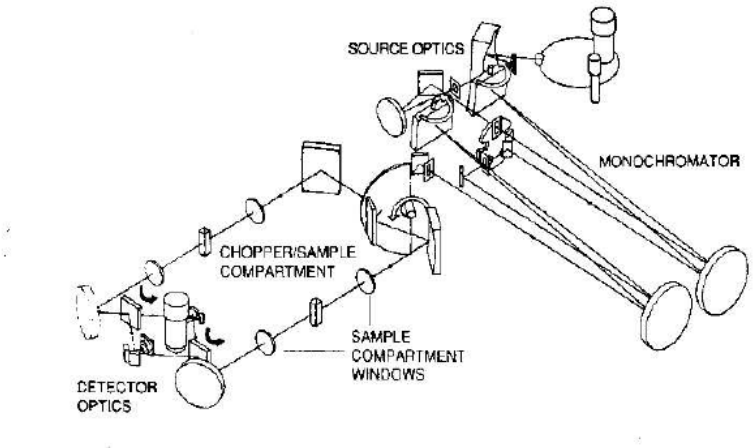

Figure 3.5. Internal scheme of Cary 500 spectrophotometer.

3.4.4 Excitation source

In this section, the several laser sources used in the thesis work, are briefly described.

Argon Laser

The Coherent-Innova 305 Argon laser was used for the fluorescence spectra acquisition of sample doped with trivalent Pr. Its active medium is an Argon ion plasma, obtained by electrical discharge in an Argon gas. This laser can be used in single line mode or in the multiline mode. In the first case the emission is monochromatic and the wavelength is selected by a prism inserted in the cavity. In the second one, the Innova 305 model has two multiline configurations: one for the UV emission (33.4-368.9 nm) and an other in the visible region (457.9-514.5 nm). For the multilines settings the emission is a composition of many wavelengths and the absence of the prism implies a higher emission power.

GaN laser diode

Two different GAN laser diode was used during this work. A Nichia (NDB7112E) laser diode , with emission wavelength around 445 nm and a maximum power of 600 mW, was used for steady state measurements on Pr ions. A 405 nm Nichia GaN laser (NDV4313) with an emission wavelength of 405 nm and a maximum power of 120 mW, was used for the measurements on the crystals doped with Sm and Eu ions.

UV Light emitting diode

A 385 nm Led with a maximum power of 4mW and a FWHM of about 15nm is used for the excitation of Dy, Sm, and Eu ions.

Pulsed Sapphire laser

In the measurements requiring a short pulse duration we used a pulsed tunable Ti:Al_2O_3 (pulse duration $\approx$ 30 ns) laser pumped by the second harmonic of a Q-switched Nd:YAG laser (Surelite I-10 by Continum)with 10Hz repetition rate. The

pump wavelength can be varied between 980 nm and 750 nm by means of a Sapphire prism with a maximum energy available, without any attenuation, of 9.1 mJ. In most of the case this laser is used for second harmonic generation thought a BBO crystal to operate in the 400-450 nm range.

3.4.5 Monocromator

The TRIAX 320 by Jobin-Yvon monochromator was used for the fluorescence measurement and for the intrinsic efficiency measurements. This monocromator is equipped with slits variable up to 2 mm and three different selectable gratings: 300 gr/mm blazed at 2 μm, 600 gr/mm blazed at 1 μm and 1200 gr/mm blazed at 0.5 μm. The slits dimension and the grating are computer controlled by software. The internal scheme of the TRIAX 320 is reported in Figure 3.6

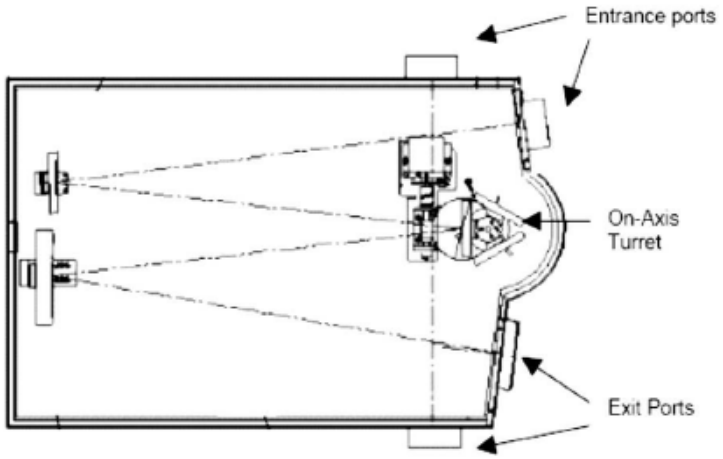

Figure 3.6. Internal scheme of Triax 320 monochromator.

3.4.6 Detectors

The detector used for the fluorescence measurements is a photomultiplier with S20 cathode useful between 300 and 800 nm, its sensibility at 700 nm is equal to 16 mA/W. For the intrinsic efficiency measurements two different detectors are used: one for the absorbed fraction determination and an other one for the emitted signal measurements. The first is a silicon detector useful between 400 nm and 1000 nm. The second one is the phototube R1464 by Hamamatsu for the 150-850 nm region. Its sensibility at 420 nm is 51 mA/W.

3.4.7 Integrating Sphere

The integrating sphere used for the intrinsic efficiency determination is the UMBB-100 by Gigahertz. The integrating sphere has a diameter of 4 inches. The interior of the sphere is machined from $BaSO_4$ painting which is characterized by a reflectance $> 97\%$ over the wavelength range from 400 to 780 nm. This wide range of higher reflectance allows to use this sphere in the visible regions of the spectrum. This sphere can be used under different ambient conditions where a coated sphere would be impractical. The sphere is equipped with four ports, three 0.5 inch diameter ports, one 2.0 inch port, and one baffle. The port locations are respectively at 0°, 60° and 90° and 180°. The buffer is posed at an angle of 135°. In order to connect our instruments and to insert the crystals on the sphere, new port adapters have been designed and manufactured in the Pisa Laboratories. In particular two new port plugs for the 0.5 inch and 2.0 inch ports have been manufactured: the first one equipped with an hole as an entrance for the laser beam, the second one equipped for mounting the sample holder and a disk used as diffusing element. The new port plug, the sample holder and the diffusive element were painted with a $BaSO_4$ painting in order to have the same reflectance properties of the integrating sphere.

3.5 Experimental set-up

3.5.1 Steady state fluorescence

A similar setup was used for the the measurements on Dy:YPO_4, Pr:BNN, Pr:KYF_4, and Tm:$YLIF_4$. Figure 4.7 shows a schematic of the set-up. The steady state fluorescence were obtained by exciting the sample with a blue, UV radiation, or IR for Tm dopant, depending on the absorption of the doping ions present in the single-crystal. CW laser beam or the UVLED fluorescence was focused onto the sample with a 10 cm focal length lens. The sample was placed on the cold finger of a cryocooler for low temperature measurements (10-300K) or on a oven tailored for small solid samples for high temperature measurements (300-700K). The fluorescence signal was detected perpendicularly to the pump laser direction to avoid pump spurious scattering. The luminescence was chopped and focused by a 75 mm focal length lens on the input slit of a Join-Yvon monochromator with 32 cm focal length (a diagram is shown in Figure 3.6). To obtain the polarized emission spectra a Glan-Thomson was put in front of the monochromator input slits. The emission radiation was directly filtered with a proper long pass filter, in order to suppress any pump signal. The monochromator was equipped with a 1200 gr/mm grating for the 360-750 nm region. The signal was detected using a S20 phototube in the visible and InSb in the IR regions, then processed by a lock-in amplifier and subsequently stored on a PC. The spectra were corrected for the spectral response of the system using a black body source at 3000 K temperature.

3.5.2 Decay-time measurements

Room temperature decay time curves were recorded with an apparatus similar to the fluorescence one described in the previous section, using as excitation source a Ti:Al_2O_3, or the second harmonic of this laser, depending on the absorption channel

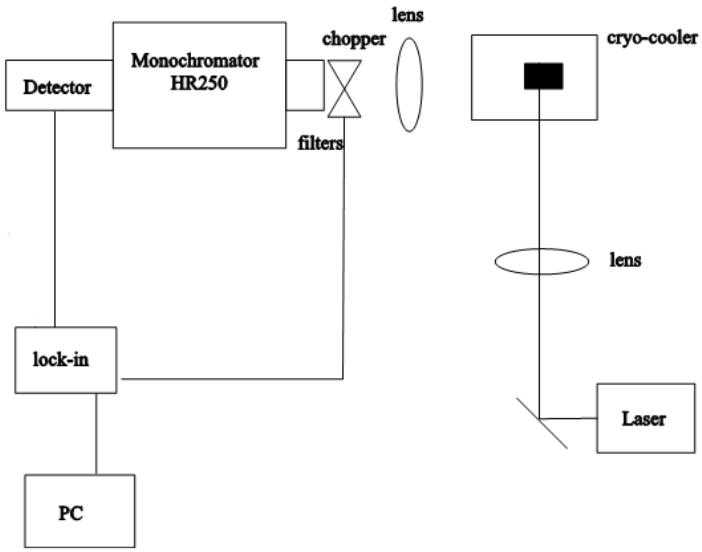

Figure 3.7. Scheme of the experimental apparatus for fluorescence measurements

considered. The samples were pumped near an edge and the fluorescence was collected from a thin section ($\sim$ 1 mm) of the sample to observe a uniformly pumped volume and reduce radiation trapping effect; furthermore the power incident on the sample was reduced by means of attenuators to suppress as much as possible non-linear effects. The signal from the detector (photomultiplier with S20 cathode or liquid nitrogen cooled InSb) was amplified, by fast amplifiers, and then processed by a Fluke digital oscilloscope, connected to a PC for the storing.

3.5.3 Intrinsic efficiency measurement

Usually two kinds of efficiencies are distinguished: the "raw efficiency" and the "intrinsic efficiency" The raw efficiency is the ratio of total visible emitted power (either in radiometric or photometric units) to the average pump power incident on a sample:

$$\eta_{raw} = \frac{P_{em}}{P_{inc}} \tag{3.1}$$

The intrinsic efficiency is the ratio between the total visible power emitted and the pump power absorbed by a sample:

$$\eta_{int} = \frac{P_{em}}{P_{abs}} \tag{3.2}$$

The absorbed power is related to the incident power by:

$$P_{abs} = f_{abs} \times P_{inc} \tag{3.3}$$

where f_{abs} represent the absorbed fraction. Efficiencies are either given in radiometric units, usually % or W/W (unit-less), or in photometric unit, usually in lm/W.

Since this work is a physical and preliminary study to produce a white light emitting device based on the proposed crystals, I will refer only to the intrinsic efficiency. It represents the maximum efficiency obtainable from a future engineered device. The raw efficiency will depend on the intrinsic efficiency and on the efficiency of the other device components. This value can be optimized in founding the best design.

In order to calculate the intrinsic efficiency we need to know the fraction absorbed of incident power by each sample and their emission luminescence in the region from 450 to 750 nm. In order to measure the two quantities a diffusive method presented by Rohwer and Martin [79] with some changes to adapt it to our experimental set-up was used. The technique is based on the excitation of the samples with diffused light inside an integrating sphere.

The absorbed fraction is calculated in the sphere instead of a calculation based on the measured absorption coefficients since we want to obtain a measurement independent from the pump radiation direction. Inside the sphere in fact, the diffused light is absorbed from the crystal for many different optical paths and hitting on different surfaces with different incident angles. This fact makes this measurement

completely independent from the sample geometry and for any kind of pumping design.

3.5.4 Absorbed fraction determination

The measurement of absorption were performed in the integrating sphere by using, as pumping source, a GaN laser diode (Nichia NDB7112E) emitting at $\sim$ 444 nm. The laser beam was split, as show in Figure 3.8 by a beam-splitter . The first beam was directed inside the integrating sphere, chopped and focused with a 200 mm focal lens on a diffuser inside the sphere. The laser beam hit on the diffuser disk with an angle of $\sim \pi/2$, in order to create a gas of photon inside the sphere. The sample was inside the sphere, behind the diffuser disk to avoid to pump directly the sample. The second beam chopped at a different frequency than the other hit a diffuser outside the sphere, this beam was used as reference.

Both the beams were detected by a Si Photodiode, placed in front of the exit port of the integrating sphere. The signal that came from the integrating sphere was filtered using a interferential filter, in order to detect the laser emission only. The signal coming out from the sphere was called primary. The photodiode was then plugged with two different Lock-in amplifiers, using the two different reference frequency, in order to detect both the reference signal and the signal that came from the integrating sphere at he same time.

3.5.5 Efficiency measurements

The set-up was quite different from that used for the absorption measurements (see Figure 3.9). The pumping source was not split, it was chopped and focused with 200 mm lens inside the integrating sphere, as the primary beam of the absorption set-up. For the measurement of the emitted intensity we used an optical fibre inserted at the out port of the sphere and we focused the collected radiation on a monochromator

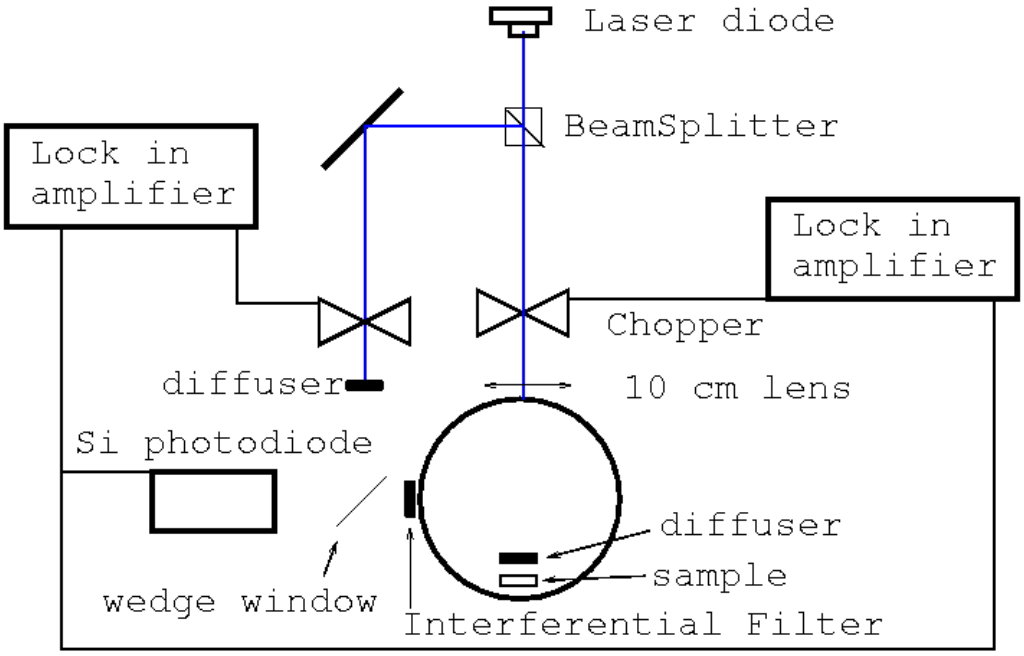

Figure 3.8. Experimental setup for the absorption measurements

of 320 mm focal length equipped with a 1200 g/mm grating for the $360 - 750$ nm region. In front of its input slits we inserted a long-pass filter (cut-off 455 nm) to cut the laser radiation. For each sample, we measured the input laser power. With the same setup, but without the long-pass filter in place, we also acquired the laser emission spectrum from 435 to 455 nm. Both spectra were then corrected for the spectral response of the system using a black body source at a temperature of 3000 K coupled inside the sphere with the same geometrical setup.

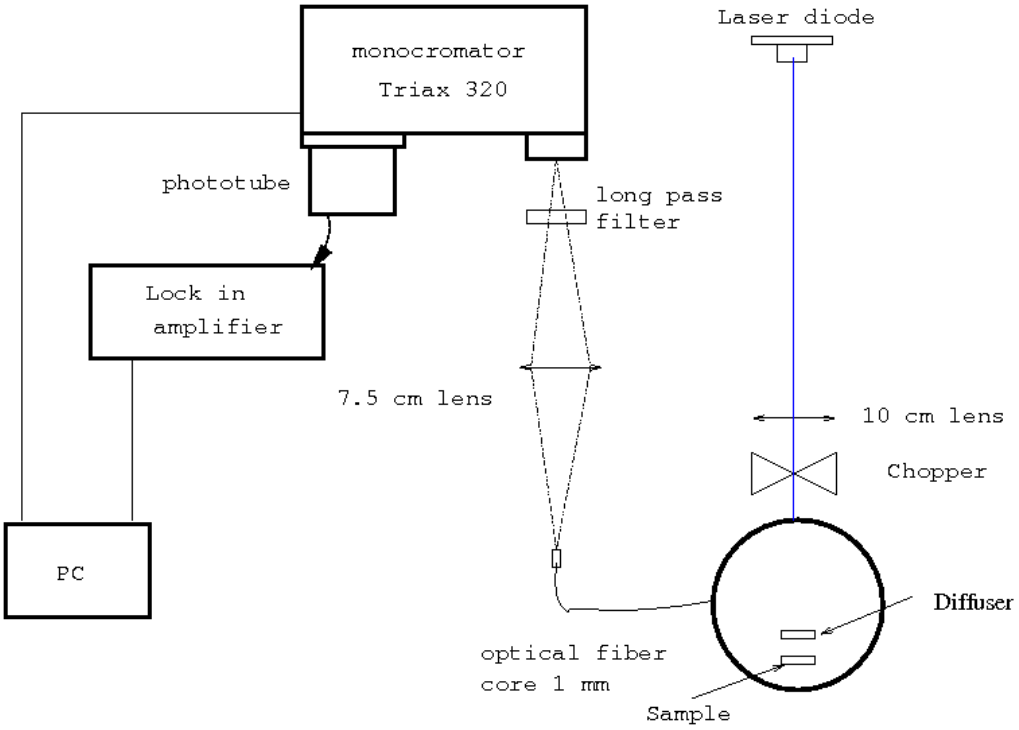

Figure 3.9. Experimental setup for the fluorescence measurements

Chapter 4

White light generation

In this chapter the results of measurements performed on Pr doped fluorides are presented and discussed. Different host crystals, and different doping concentrations are analysed, in order to understand what could be the best combination of lattice and doping concentration to achieve the highest efficiency in visible light generation.

4.1 Pr Levels

Pr is the third lightest element of the lanthanides with an atomic number of Z = 59. In the trivalent state Pr^{3+}-ions have two $4f$-electrons which can occupy 13 energy states inside the $4f$-orbitals. The $^3H_4$-state is the ground state. In this thesis we will focus on the transition between the $4f$ levels in which are involved several emissions in the visible spectral range: from the blue to near IR (Figure 4.1).

For our purpose we choose to pump $^3P_2$ manifolds using a GaN laser diode. After a non radiative relaxation to the $^3P_0$ energy levels we can observe the visible transition to the $^3H_4$ levels in the blue region ,$^3H_5$ in the green region, and to the $^3H_6$,^3F_i with i=2,3,4 in the red region. The high number of discrete emissions cover the entire visible spectral range, and thus allow the use of crystals doped with Pr

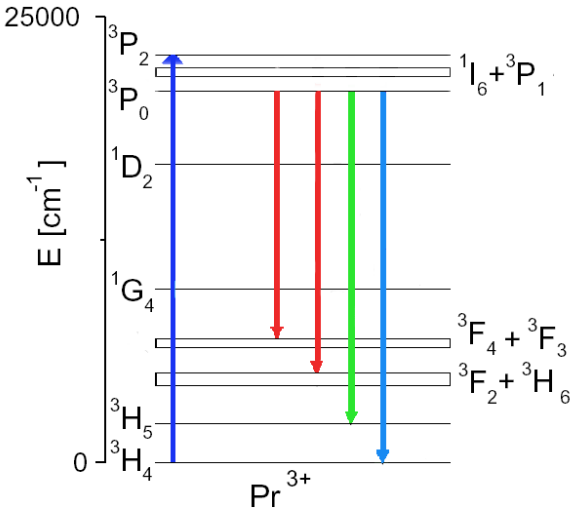

Figure 4.1. Energy levels of the Pr^{3+} ion and the transition studied

as white light sources. Obviously, as previously mentioned, an investigation of the influence of both lattice and doping concentration on the efficiency of the emission is necessary in order to find the combination giving rise to the best emission efficiency

4.2 Absorption measurements

As described in the section 3.4.3, the absorption measurement was performed using a Carry500 in the interval between 420-500 nm with a resolution of 0.1 nm and using polarized light. In this interval is possible to detect the ground state absorption of the ^3P_j j = 0,1,2 and $^1I_6$ manifold, we are in fact interested in characterize the absorption of the crystals in the blue range, and the fluorescence in the entire visible spectra. Each spectrum is automatically computer-corrected for the background signal obtained by the spectrum acquisition of a blank spectrum. Inserting two polarisers on the reference and on the sample beams, the different crystal polarizations have been investigated. The polarizations refer to the relative direction between the incident electric field polarization and the crystallographic axes of each sample.

The absorption coefficients are obtained by the following relationship:

$$\alpha(\lambda) = \frac{A(\lambda) \times \log_e(10)}{d}, \tag{4.1}$$

where d is the sample thickness and A(λ) the absorbance obtained from the CARY 500 defined as:

$$A(\lambda) = \log_{10}\left(\frac{I_0}{I_1}\right), \tag{4.2}$$

I_0, and I_1 respectively are the incident intensity on the sample and its transmitted intensity. The absorption transitions of the Pr^{3+} ions in the investigated region (from 420 to 500 nm) are:

- $^3H_4 \rightarrow ^3P_0$ around 480 nm;
- $^3H_4 \rightarrow ^3P_1$ and $^1I_6$, around 470 nm;
- $^3H_4 \rightarrow ^3P_2$, around 445 nm.

4.2.1 Absorption spectra

In this section, some of the absorption spectra acquired during the all experimental activity are shown. In order to compare the behaviour of the different lattice available, the absorption spectra for doping concentration equal to 1.25%at are shown. As any KY_3F_{10} with this concentration was available we shows the absorption spectra for a concentration of 0.3%at. As expected, the shape of the spectra do not change, only the absolute absorption value changes.

KY_3F_{10}

Since KY_3F_{10} has a cubic structure of the crystalline cell, the use of polariser in the two beams (E ‖ a) is not needed. As previously mentioned, for this crystalline host only a doping concentration (0.3% Pr^{3+}:KY_3F_{10}) was available. The absorption

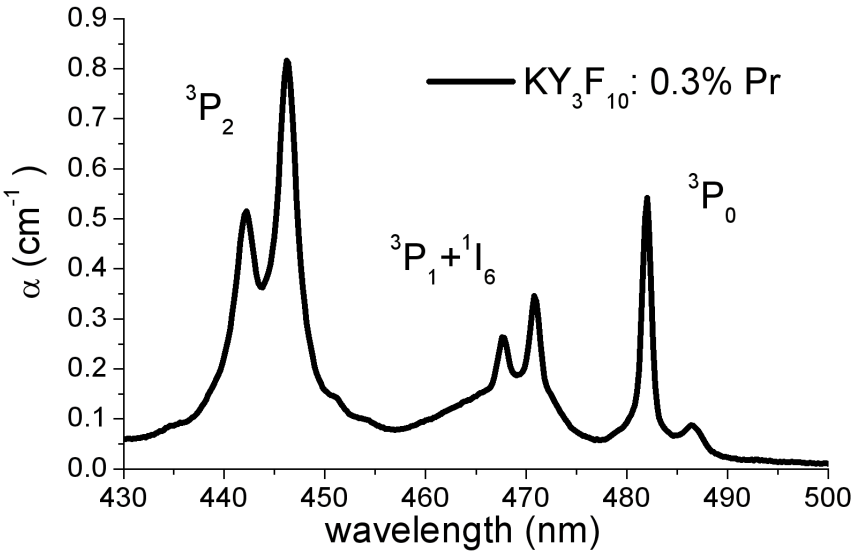

Figure 4.2. Absorption of KY_3F_{10} 0.3% Pr^{3+} in the 420-500nm regions.

spectrum is reported in Figure 4.2. The wavelength resolution is 0.6 nm. In the graph are visible 6 different peaks. The first two peaks correspond to the transition $^3H_4 \rightarrow ^3P_2$. The maximum of the absorption for this transition is at 446.2 nm, and has an intensity of 0.77 cm^{-1}. The others two couples of peaks correspond respectively to the transitions $^3H_4 \rightarrow ^3P_1+^1I_6$ (0.39 cm^{-1} at 470.8 nm), and to the transition $^3H_4 \rightarrow ^3P_0$ (0.52 cm^{-1} at 482 nm). The spectrum is quite broad, the narrowest line, corresponding to the $^3P_0$ level, has a full width to half height of 1 nm.

KYF_4

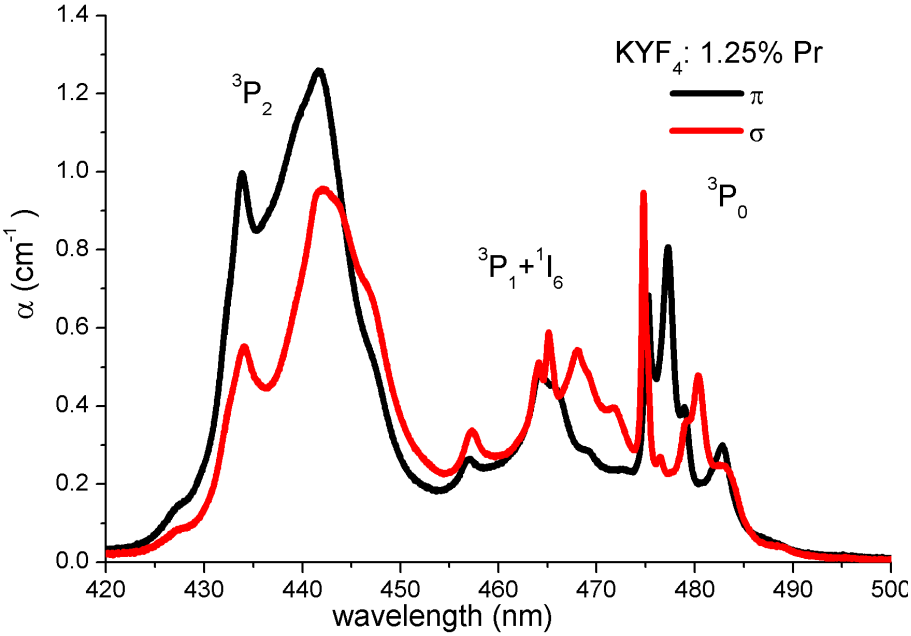

Figure 4.3. Polarized absorption of KYF_4 1.25% Pr^{3+} in the 420-500nm interval

For the 1.25% Pr^{3+}:KYF_4 sample both the π (E$\|$c) and σ (E$\|$a) polarizations was collected. Two different sample with different dimensions were investigated. We want to use them to investigate the volume dependence in the following efficiency measurements. In order avoid any difference in real Pr concentration the two sample were cut from the same boules at the same vertical growth position. Both samples has the same absorption spectra and in Figure 4.3 the RT absorption spectra of one of them is reported. The wavelength resolution is 0.1 nm. In the graph it is possible to identify the absorption relative at the three transition. The maximum absorption for the $^3H_4 \rightarrow ^3P_2$ transition is observed for π polarization with a peak value of 1.3 cm^{-1} at 441.6 nm. For the transition $^3H_4 \rightarrow ^3P_1+^1I_6$ the maximum absorption is still observed for π polarizations, with a peak value of 0.59 cm^{-1} at 465.1 nm. The maximum for the transition $^3H_4 \rightarrow ^3P_0$ is instead observed for σ polarization

with a peak value of 0.95 cm^{-1} at 474.8 nm. Also the widths of each transition line are different to respect the previous sample. More specifically, the KYF_4 absorption spectrum is broader than the KY_3F_{10} one in the regions of the $^3P_2$ and $^3P_1$ $+^1I_6$ transitions but narrower for the $^3P_0$ transition.

$LiLuF_4$

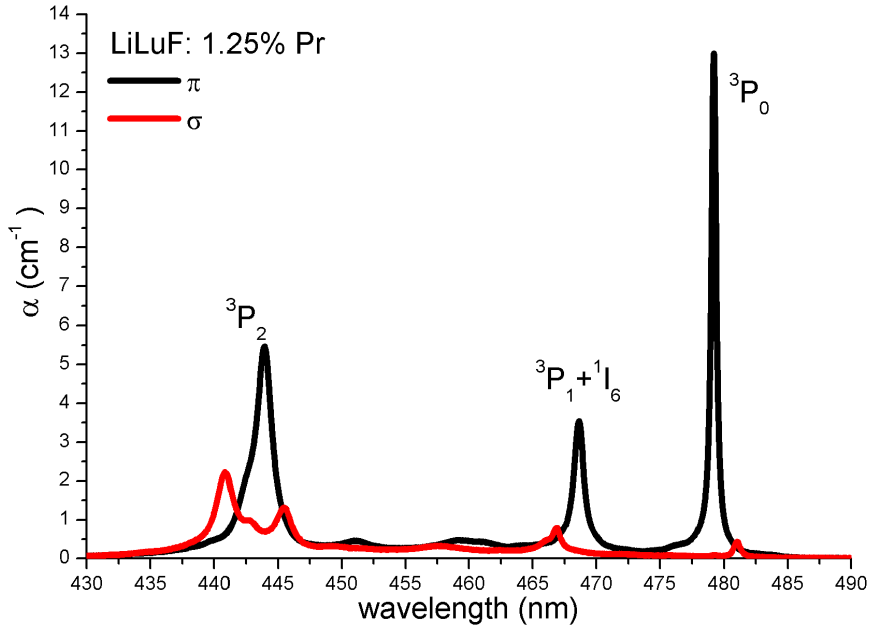

Figure 4.4. Polarized absorption of $LiLuF_4$ 1.25% Pr^{3+} in the 430-490nm regions

The room temperature absorption spectra for the 1.25% Pr^{3+}:$LiLuF_4$ sample is shown in Figure 4.4. Since the unit cell of the $LiLuF_4$ crystal is tetragonal, the acquired polarizations are π (E||c) and σ (E⊥c), as for the 1.25% Pr^{3+}:KYF_4 sample. The wavelength resolution is 0.1 nm. The absorption peak values relative to each transition belong to the π polarization. The absorption peak value of the $^3H_4 \rightarrow ^3P_2$ transition is 5.5 cm^{-1} at 443.9 nm, for the $^3H_4 \rightarrow ^3P_1 + ^1I_6$ transition the peak value is 3.45 cm^{-1}at 468.7 nm and for the same polarization at 479.2 nm the

peak value for the $^3H_4 \rightarrow ^3P_0$ is equal to 12.9 cm^{-1}. The absorption closer to the laser diode peak (444.4 nm) is 3.7 cm^{-1} very similar to the maximum absorption of the $^3H_4 \rightarrow ^3P_2$ transition. The width of each absorption transition is narrower than the Pr^{3+}:KY_3F_{10} and Pr^{3+}:KYF_4 samples.

BAY_2F_8

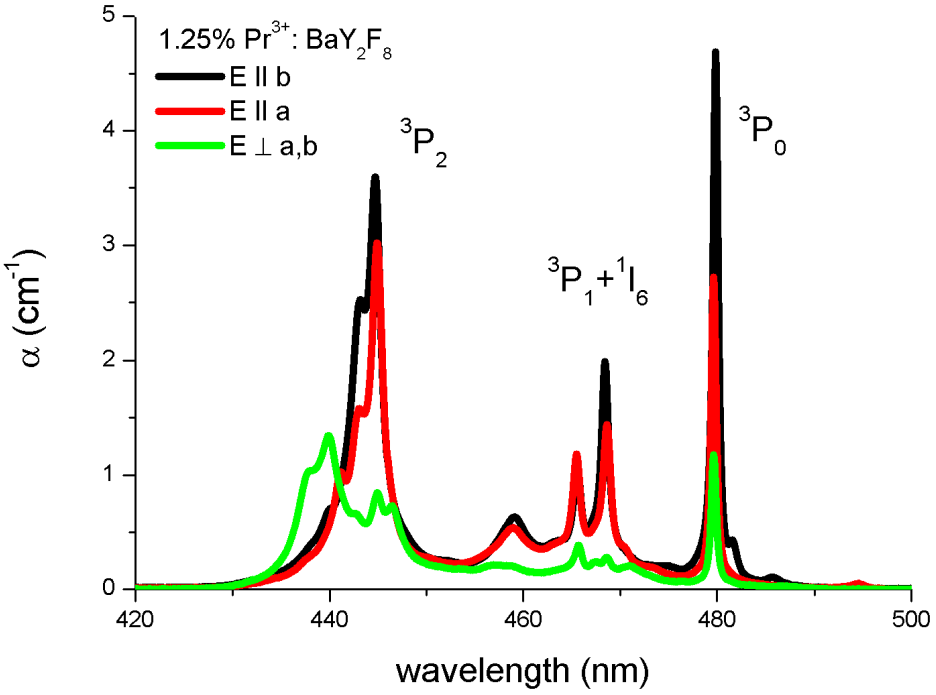

Figure 4.5. Polarized absorption of BaYF 1.25% Pr^{3+} in the 420-500nm regions

For this crystal host matrix five different Pr^{3+} nominal doping levels have been investigated: 0.3%, 0.5%, 1.25%, 2% and 3%. The wavelength resolution used in each sample investigation is 0.2 nm.

The absorption spectra for the 1.25% Pr^{3+}:BaY_2F_8 crystal are shown in Figure 4.5 for the three polarizations (E‖b, E‖a, and E⊥a,b). The maximum peak

absorption values relative to each transition belong to the E‖b polarization. The absorption peak value of the $^3H_4 \rightarrow ^3P_2$ transition is 3.6 cm^{-1} at 444.8 nm. For the $^3H_4 \rightarrow ^3P_1 + ^1I_6$ transition the peak value is 1.99 cm^{-1}at 468.4 nm, while for the $^3H_4 \rightarrow ^3P_0$ the peak value is of 4.69 cm^{-1} at 479 nm. The absorption close to the laser diode peak (444.4 nm) is 3.3 cm^{-1} very close to the maximum absorption of the $^3H_4 \rightarrow ^3P_2$ transition. Although the doping concentration of the sample of BaY_2F_8 is the same of the KYF_4, the absorption measured is almost three times bigger.

The absorption spectra for the 3.0% Pr^{3+}:BaY_2F_8 crystal are shown in Figure 4.6 for three polarizations (E‖b, E‖a, and E⊥a,b). For this sample the maximum peak absorption values relative to each transition belong to the E‖b polarization. The absorption peak value of the $^3H_4 \rightarrow ^3P_2$ transition is 13.45 cm^{-1} at 444.8 nm, while for the transitions $^3H_4 \rightarrow ^3P_1 + ^1I_6$, and $^3H_4 \rightarrow ^3P_0$ are respectively 7.6 cm^{-1} at 468.4 nm, and 14.0 cm^{-1} at 479.8 nm

It was expected that the α is proportional to the rare earth doping levels, but the two BaYF sample does not follow the expected relations. Indeed the ratio between the the doping levels is $1.25/3 = 0.46$ while the ratio between the absorption coefficient at 444.8 nm in E‖b polarization is 0.26. As already say the segregation coefficient of the Pr ions in Bayf (K_{seg}) is about $0.4 - 0.5$, that means that a real concentration is lower than the nominal one, about half the nominal concentration. Furthermore the concentration varies inside the boules along the growth axis. For this reason in this thesis I'll refer only to the nominal doping of the crystals corresponding to the Pr^{3+} powders inserted in the crucible to start the growth. A deeper study of the dependence of the absorption spectrum and the position of the sample on the bulb could be very interesting. However in our case there is not a measured position on the bulb of the obtained samples.

The different shape of the spectra for the two polarization, observed for both 1.25% Pr^{3+}:BaY_2F_8 and in the 3% Pr^{3+}:BaY_2F_8, is probably due to an experimental

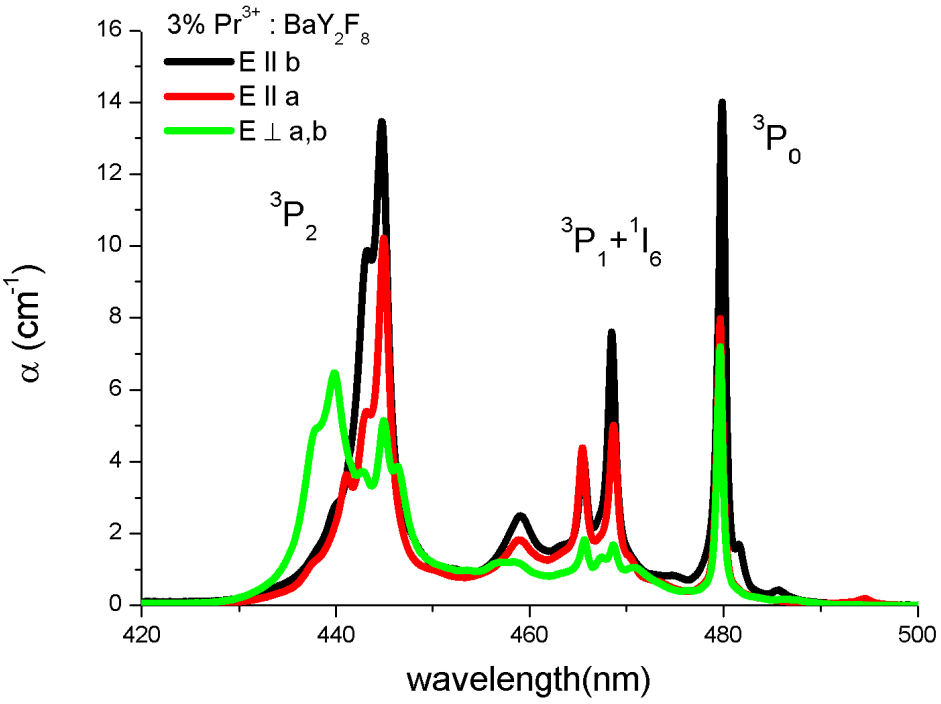

Figure 4.6. Polarized absorption of BaYF 3% Pr^{3+} in the 420-500nm regions

error in the orientation and cutting procedure. In fact, the error in orienting and thus catting the sample is of around 2°.

4.3 Efficiency measurements

To measure the intrinsic efficiency of our samples we used the diffusive method presented by Rohwer and Martin [79] with some changes to adapt it to our experimental set up. The set-up is reported in Figure 3.8. The method consists in creating a uniform pump-photon gas inside an integrating sphere. The diffused laser light is absorbed by the samples and the fluorescence is emitted inside the sphere and collected with an optical fibre. Even if this configuration makes the measurements more

difficult (the power absorbed is much lower than in case of direct excitation, therefore the emitted signal is much weaker) , it has the advantage to grantee the same experimental conditions for all the samples, and give rise to results independent from the pumping geometry.

In our experimental set-up we measured both the emitted and pump light intensity with a photomultiplier. After proper calibration the signal from the photomultiplier (I) is proportional to the fluorescence power hitting the detector; the emission efficiency(EE) η is defined as:

$$\eta = \frac{I_{emis}}{I_{exc}}, \tag{4.3}$$

where I_{emis} is the detected emission intensity and I_{exc} is the laser excitation intensity.

The emission efficiency depends on the intensity fraction absorbed by the material, and thus on the experimental set up. As we are interested in characterizing a physical property of the material, so we calculated the intrinsic EE (η_{int}) defined as:

$$\eta_{int} = \frac{I_{emis}}{I_{abs}}, \tag{4.4}$$

where I_{abs} is the absorbed light intensity.

The intrinsic EE is a meaningful quantity because it sets an upper limit to the maximum efficiency attainable by an engineered device, whose real efficiency strongly depends on its realization details. To determinate the intrinsic E.E. we need to measure independently two different quantities: the power absorbed by the sample and the power emitted. The two quantities were measured independently using basically the same setup in which we apport some changes in the two cases as described in the following paragraphs.

4.3.1 Absorption

In this section are shown the results of the measurement of the absorbed fraction of power. The acquired data will be used in the calculation of the intrinsic efficiencies. In the measurement of the absorbed fraction, one of the most crucial parameters is the position of the sample inside the sphere. To reduce the influence of this parameter we used a diffuser located inside the sphere, to create a photon gas and thus avoid the direct illumination of the sample, and the dependence on its location.

As described in the section 3.5.4, the set-up allow us to monitor the laser beam (reference beam) and the laser radiation exiting from the integrating sphere (the primary beam). The idea is to measure the laser radiation exiting from the integrating sphere with and without the sample under investigation inside the sphere, and then calculate the absorbed fraction using the formula:

$$f_{abs} = \frac{I_0 - I_s}{I_0}, \tag{4.5}$$

where the I_0, and I_s are, respectively, the intensity of the signal exiting form the integrating sphere without and with the sample. Obviously a requirement of this measurements is the power stability of the laser; in order to remove any dependence form the power drift of the excitation source, the reference beam is used to monitor it. So every intensity acquired was then normalized dividing it by the laser intensity, defining the ratio:

$$R_s = \frac{I_s}{I_{rs}} \tag{4.6}$$

where I_{rs} is the intensity of the laser acquired during the acquisition with the sample in the sphere. A similar quantity R_0 can be defined for the acquisition without the sample. Consequently the f_{abs} become:

$$f_{abs} = \frac{R_0 - R_s}{R_0} = 1 - \frac{R_s}{R_0} \tag{4.7}$$

In order to reduce the error we actually take the average value of different measurements. To check the repeatability, we repeated the measurement even after have replaced the crystal inside the sphere. We estimate an accuracy of the order of 0.1% on the abs fraction. In Table 4.1 are reported the calculated f_{abs} values, the dimension of the samples, the doping concentration, and the assigned label. The double beam and the use of the same detector for the reference and the signal beam allow us to estimate also the absorption of the most diluted crystals, that are not possible in a single beam set-up, as described in the previsions measurements performed on these samples [34].

Looking at the KYF_4 samples (I, and L) with different volumes it can be noted that the absorbed fraction is proportional to the volumes within the experimental accuracy. Moreover the volume of the two sample is similar, the ratio of the volume is 0.8, and the the f_{abs} value is the same for both the sample within the experimental accuracy. A deeper study in the volume dependence could be interesting, but it requires at least two samples with a ratio of the volume of 0.5 and it will be

Table 4.1. Absorption results, for any sample we report the absorption.

crystal	Pr^{3+} doping	absorption(%) fraction	dimension (mm^3)	label
BaY_2F_8	0.3%	1.07	45.8	A
	0.5%	0.82	50.5	B
	1.25%	2.48	183.6	C
	2%	1.14	39.6	D
	3%	3.05	131.5	E
$LiLuF_4$	0.5%	0.80	129.5	F
	1.25%	1.74	155.9	G
	2%	1.04	20.8	H
KYF_4 big	1.25%	1.15	73.1	I
KYF_4 small		1.10	60.4	L
KY_3F_{10}	0.3	0.56	46.2	M

investigate in the future.

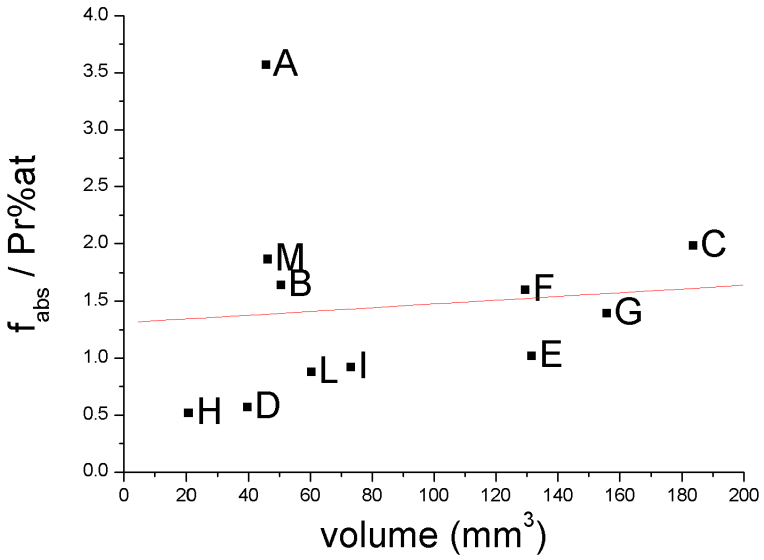

Figure 4.7. Normalized f_{abs} plotted versus the volume of the sample, the label indicated in Table 4.1 are used to discriminate the different sample.

As you can see in Table 4.1, the samples with a doping percentage equal to 2%, both LiLuF and BaYF (label H and D) have a small absorption fraction compared to samples less doped. This is, obviously a consequence of the smaller volume of these samples, to respect other samples with the same lattice.

In Figure 4.7 is shown a plot of the ratio between f_{abs} and the Pr %at as a function of the sample volume. The ratio f_{abs}/Pr %at can be considered as a sort of normalized f_{abs}.

A linear dependence of the absorption fraction from the sample volume is observed, with some exception as sample A, which value of f_{abs} diverge from the linear behaviour observed for the other samples. As previously mentioned, the measurement of a value that diverge from the linear trend, may be ascribed to an error done

in estimating the actual doping concentration of the sample. In fact, the concentration here reported refers to the raw material, that can be considerably different from the actual crystal doping. The actual concentration depends on the segregation coefficient K_{seg}, that for $LiLuF_4$ is equal to 0.1-0.2, while for other crystals is 0.4-0.5. In other words, the actual concentration is surely smaller than the raw material, and can vary along the growth axis due to the change of concentration in the melt during the growth. Therefore the normalization of the f_{abs} does not complete remove the dependence from the doping concentration.

4.3.2 Fluorescence

The unpolarized fluorescence spectra for the Pr-doped sample was acquired using the set-up presented in 3.5.5. In the following is shown a spectra for every lattice: 1.25%Pr:$LiLuF_4$ (Figure 4.8), 1.25%Pr:KYF_4 big sample(I)(Figure 4.9), the 1.25%Pr:BaY_2F_8 (Figure 4.10), and the 0.3%Pr:KY_3F_{10} (Figure 4.11).

The laser emission spectrum from 435 to 450 nm was acquired using the same set-up, in which the long-pass filter was obviously removed. The monochromator setting is the same used for the visible emission but the power is now attenuated by a couple of neutral filters, with nominal transmission value of 0.23%. The laser spectrum was recorded just before inserting a new sample in the integrating sphere. As an example, the laser radiation acquired with the same resolution used for the fluorescence measurements, is reported in Figure 4.12.

In order to obtain a total intensity in arbitrary units for the emission and the laser signal, the spectra are integrated:

$$I(\lambda) = \int I_{acq}(\lambda) dI \tag{4.8}$$

where $I_{acq}(\lambda)$ is the acquired spectrum. The emitted signal was integrated in the

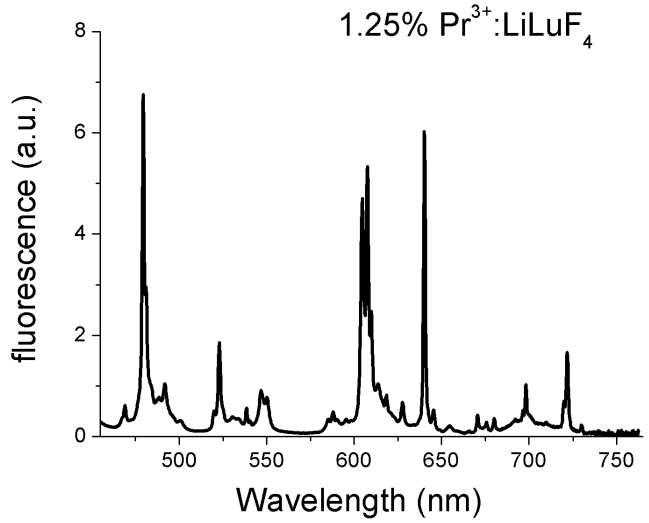

Figure 4.8. Unpolarized fluorescence at room temperature of 1.25%Pr:$LiLuF_4$.

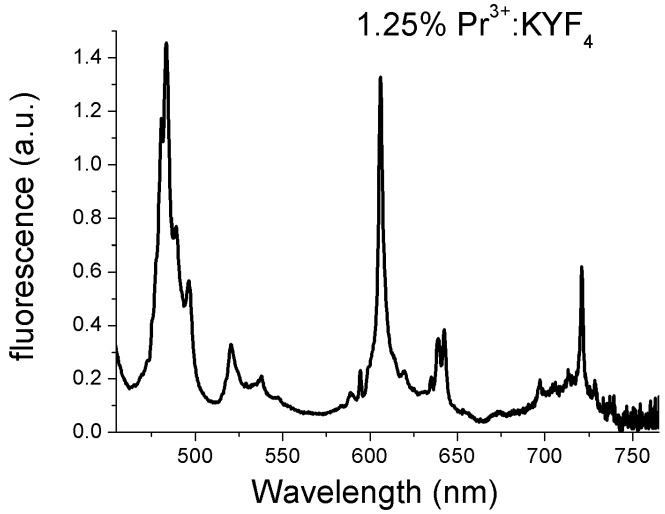

Figure 4.9. Unpolarized fluorescence at room temperature of 1.25%PrKYF_4 sample.

interval 460-720 nm. Even if it possible to observe fluorescence after 720 nm, the colour matching functions (x, y and z) are very low, and it has no sense to integrate for longer wavelengths. The laser signal was instead integrated between 437 nm and

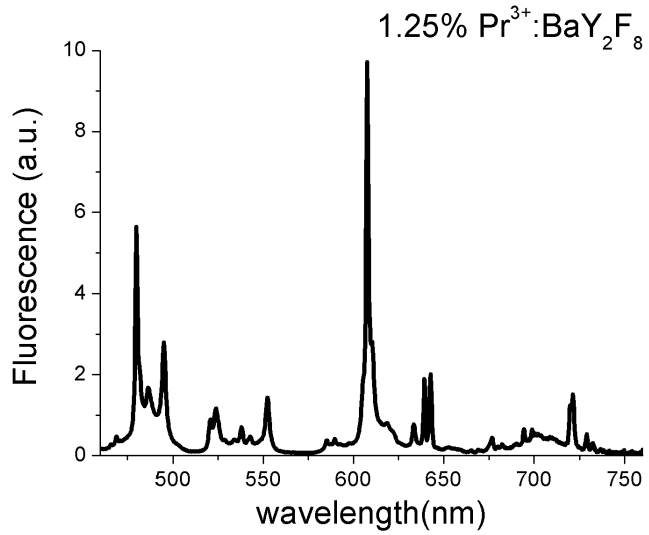

Figure 4.10. Unpolarized fluorescence at room temperature of 1.25%Pr:BaY_2F_8 samnple.

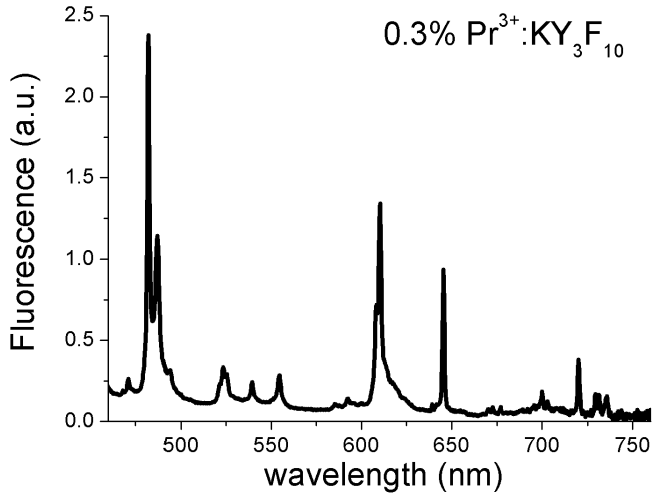

Figure 4.11. Unpolarized fluorescence at room temperature of 0.3%Pr:KY_3F_{10} sample.

450 nm. After these integrations we obtained two values of the total intensity in arbitrary units: one for the emitted radiation in the visible region and one for the

incident radiation. Since these two intensities refer to different incident powers on the diffusing element inside the sphere, they are not directly comparable.

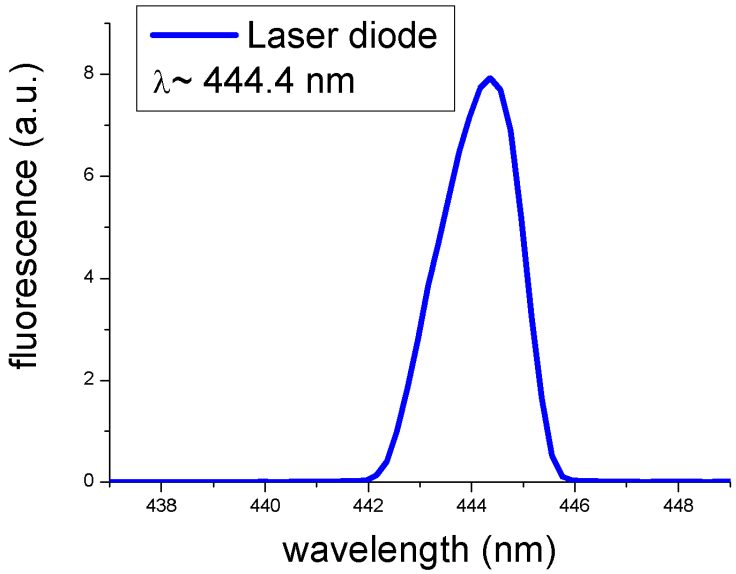

Figure 4.12. GaN laser diode spectrum for the efficiency measurement

During the measurements the linearity of the system was verified by reducing the incident power and observing a corresponding equal reduction of the acquired signal. It means that it is possible to rescale the intensity of the laser signal in order to compare the two signals. To do that I used the following relation between the power and the integrated intensities, where I_{P_i} is the integrated intensity corresponding to an incident power P_i.

$$I_{P_2} = \frac{P_2}{P_1} I_{P_1}. \tag{4.9}$$

Up to now all of the intrinsic efficiency calculations refer to the integrated intensity rescaled to the same incident power. The intrinsic efficiency is now defined as:

$$\eta_{int} = \frac{I_{emi}}{I_{abs}}; \tag{4.10}$$

the ratio between all the emitted intensity (I_{emi}) in the all solid angle and the absorbed intensity(I_{abs}).

The absorbed signal is:

$$I_{abs} = f_{abs} \times I_{exc}; \tag{4.11}$$

where f_{abs} is the absorbed fraction previously calculated, while I_{exc} is the excitation laser intensity. Substituting equation 4.11 into equation 4.10 one obtains the formula for the intrinsic efficiency calculus:

$$\eta_{int} = \frac{I_{emi}}{I_{exc} \times f_{abs}}. \tag{4.12}$$

The experimental intrinsic efficiency in percent are reported in Table 4.2.

Table 4.2. Intrinsic efficiency evaluated for the sample.

crystal	Pr^{3+} doping	efficiency(%)	label
BaY_2F_8	0.3%	35	A
	0.5%	35	B
	1.25%	56	C
	2%	48	D
	3%	18	E
$LiLuF_4$	0.5%	41	F
	1.25%	60	G
	2%	46	H
KYF_4 big	1.25%	36	I
KYF_4 small		36	L
KY_3F_{10}	0.3%	52	M

4.3.3 Results

The obtained values are labelled in Table 4.2. The estimated error on our measurements is 5% and comes from the statistical spread of a series of independent

measurements. The most efficient sample is the 1.25% Pr^{3+} $LiLuF_4$ with an intrinsic efficiency as high as 60%. Very close to the LiLuF sample we have the 1.25%Pr^{3+}:BaY_2F_8 (B) with an intrinsic efficiency of 55% . The obtained EE values are very high because they indicate that 55% of the absorbed pump power is converted into visible emission. The other sample of BaYF and LiLuF show a lower efficiency, this lead us to think that probably the better doping levels for our purpose is around the 1% in the melt. This is clearly showed in the Figure 4.13, indeed for the LiLuF and BaYF samples the maximum efficiency is achived with the 1.25% doping levels.

From Table 4.2 we can deduce that the intrinsic EE values are dependent on the host crystal but not on the nominal doping concentration. The intrinsic EE of the samples C and F with 1.25% of Pr^{3+} doping level are comparable, and the small difference among them is probably to be assigned to the different host crystals.

Since the two KYF_4 samples (I and L) show the same efficiency the geometrical shape does not affect the intrinsic EE value, but they show an efficiency lower than the other 1.25% Pr doped crystals, this is probably due to the disordered nature of the crystals [59]. This host materials can be interesting for his emission band larger than the other fluorides, this fact can lead to a better rendering response than the other fluorides investigated. A more complete spectroscopic study of the sample are presented in chapter 5.

The value obtained for the sample E (3% Pr in BaYF) is much lower than the others, but it is probably affected by the crystal quality of the sample. In fact the sample presents some inclusions of unknown origin, visible using a microscope.

Has to be noted that the sample M (0.3%at Pr in KY_3F_{10} lattice) shows a very high efficiency (EE=55%) despite the low doping concentration. The analysis of a sample with a higher doping level can be very promising, in order to achieve a higher efficiency, unfortunately the growth of sample of this material with higher

concentration is still under investigation.

The comparison between our results and the results obtained by others groups and researchers is not easy, especially because the published efficiencies are always referring to the raw efficiency characteristic of a developed device. Few works present the intrinsic efficiency measurement of the emitter material.

Table 4.3. Luminous efficiency for common light emitters, sources: PHILIPS and OSRAM and [80].

Lamp	luminous efficiency (lm/W)
Incandescent	4-24
Fluorescent (T12,T5,T8)	60-100
Metal halide lamp	65-115
High pressure sodium	85-150
Low pressure sodium	100-200
White LED	10-150

Looking at the display technology based on the up conversion process, Bass research group at the University of central Florida obtained a raw efficiency (ratio between the incident and the visible emitted intensity) of 8.5% for the white emission [81, 7]. The OLED internal efficiency is the number of generated photon per number of injected charge pairs. Then usually OLED efficiencies reported in the literature refer to quantum external efficiencies. External quantum efficiencies of 0.5% and 5.2% were obtained by Lim et al. [4] and by D'Andrade et al. [82] respectively. A power efficiency of 1.5% was reported by Dugall et al. [83].

Using eq. 2.1 it is possible to convert the intrinsic efficiency from the radiometric units to the photometric ones. The 1.25% Pr^{3+} $LiLuF_4$, and the 1.25% Pr^{3+} :BaY_2F_8 intrinsic efficiencies in photometric units are about 200 lm/W and 150 lm/W respectively. In this case the two intrinsic efficiencies have a larger difference than in the radiometric units. This is because the photometric units take into account the eye response using the $V(\lambda)$ function which is not constant for different wavelengths

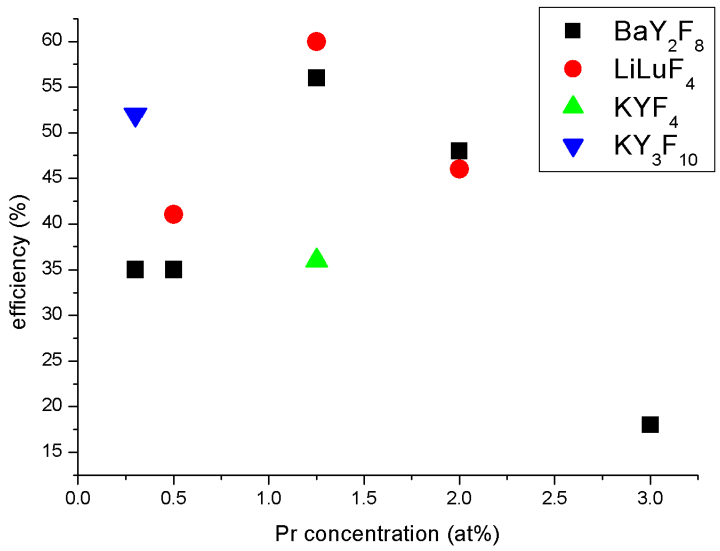

Figure 4.13. Plot of the efficiency measured versus the nominal doping levels.

(Figure 2.1). Considering a 100% absorption efficiency and a 15% efficiency of the pump sources like blue laser diodes already available in the market, the theoretical maximum wall plug luminous efficacy of a hypothetical device is about 20 lm/W for the 1.25% Pr^{3+}:$LiLuF_4$ sample. This results could be compared with that obtained with the a-Ca2P_2O_7:Eu^{2+},Mn^{2+} phosphor [84] that shows a luminous efficacy of 9 lm/W when integrated into a LED. Looking at Table 4.3, this value is comparable with the incandescent lamp but lower than the modern emitting light devices like the white LED sources and the more common fluorescence lamp. If visible laser diodes would show an efficiency similar to infrared diodes, that is 50-60%, the luminous efficacy of a fluoride-based device could be even higher than 60 lm/W.

4.4 Chromatic characterization

The fluorescence used for the determination of the intrinsic efficiency can be used for the determination of the chromatic characteristic of the samples, such as the colour coordinates and the CCT (Correlated Colour Temperature). The fluorescence acquired is unpolarized, and either the excitation used, so it is possible to exclude polarization effects, from both excitation and emission.

As previously mentioned, fluorides doped with Pr^{3+} have emissions that are composed by a series of sharp emission lines. As a consequence, a poor colour rendering is expected for this kind of sources. It is any way well known, that even sources as commercial Neon lamps have an emission composed by a series of sharp lines.

The CIE coordinates have been calculated, as described in 2.2.2, using the 1931 colour-matching functions [85, 38] using Eq. 2.2 was used to calculate the three standard primaries X, Y and Z and Eq. 2.5 to calculate the chromatic coordinates x, y and z. The colour matching functions x, y and z used in the tristimulus value determination are sampled with an interval of 1 nm, between 360 nm and 830 nm [85, 38].

The E(λ) in Eq. 2.2 is the acquired emission signal. The integral interval taken into account for the tristimulus value was from 455 - 760 nm. The reduction of the integral range can lead to an underestimation of the tristimulus values. In our case, no significant emissions are present at wavelengths shorter than 455 nm and longer than 760 nm and the colour matching functions have a very low relative contribution.

The values of the CIE coordinates obtained for the different samples analysed are reported in Table 4.4. In Table 4.4 are even shown the chromatic coordinates for an incandescent lamp at a temperature T=2800 K (a standard value for a commercial lamp) and for a Neon lamp, to compare our results with these commercial sources.

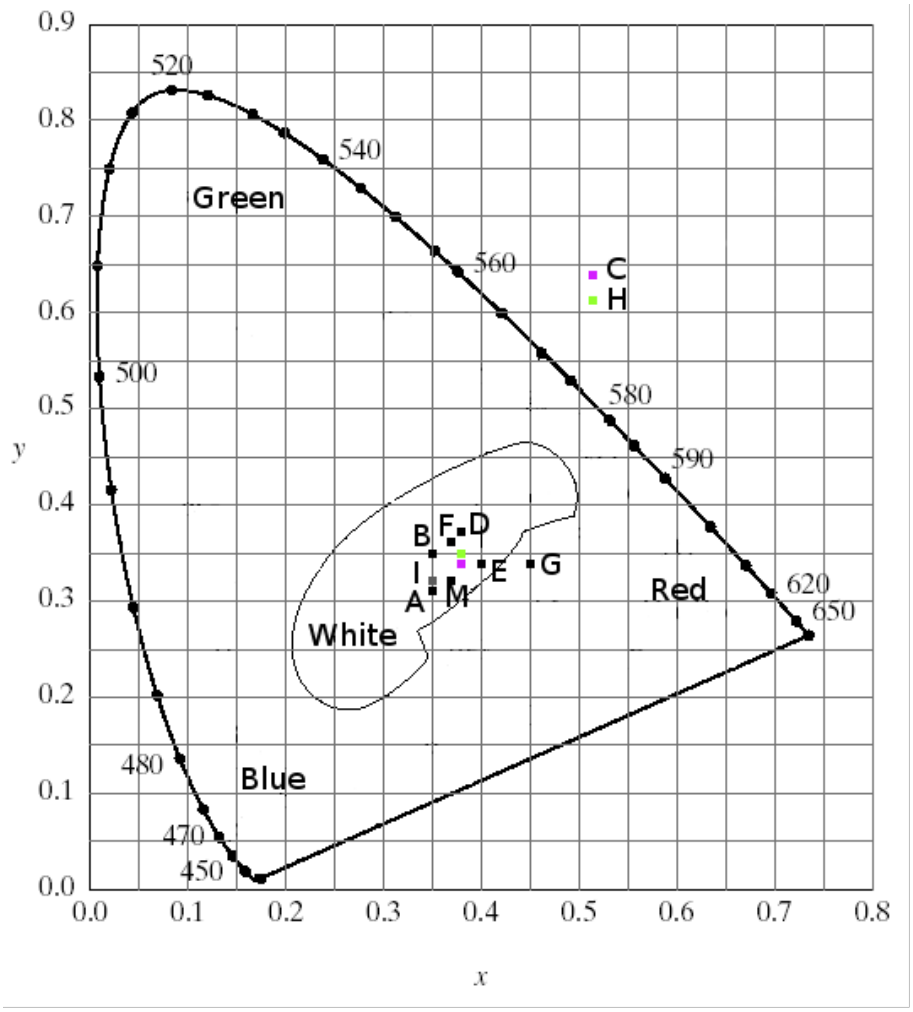

Figure 4.14. Colour coordinate of the samples reported in the CIE 1931 diagram, the white regions is reported

In Figure 4.14 is shown the CIE chromatic diagram on which are reported all the calculated (x,y) coordinates. All the samples we investigated show CIE coordinates close to the white point (0.33,0.33). The samples that show CIE coordinates closest to the "perfect white" point are: the Pr^{3+}:BaY_2F_8 A (0.3 %at), and B (0.5%at), with coordinates respectively (0.33,0.35) and (0.34,0.34); the Pr^{3+}:KYF_4 I (1.25 %at) with coordinates (0.34, 0.35); and Pr^{3+}:KY_3F_{10} M (0.3 %at) with coordinates (0.34, 0.35). Even if the other samples shows coordinates farther from

the achromatic point, it has to be noted that all the samples have coordinates well inside the white region of the CIE diagram, with the exception of the sample G (1.25%Pr^{3+}:$LiLuF_4$). It has also to be noted that the coordinates of incandescent and Neon lamps are respectively (0.45, 0.41), and (0.37, 0.37). This means that even samples that shows coordinates farther from the achromatic point are good candidates for lighting applications, if compared to commercially available sources.

Table 4.4. CIE 1931 colour coordinate of the sample studied pumped with GaN laser diode(λ=444nm).

Host	Pr^{3+} doping(%) levels	CIE coordinate	label
BaY_2F_8	0.3	(0.33;0.35)	A
	0.5	(0.34;0.34)	B
	1.25	(0.40;0.36)	C
	2	(0.37;0.37)	D
	3	(0.40;0.38)	E
$LiLuF_4$	0.5	(0.38;0.37)	F
	1.25	(0.44;0.36)	G
	2	(0.40;0.36)	H
KYF_4	1.25	(0.34;0.35)	I
		(0.34;0.35)	L
KY_3F_{10}	0.3	(0.34;0.35)	M
Incandescent lamp	-	(0.45, 0.41)	-
Neon lamp	-	(0.37, 0.37)	-

The CIE coordinates are not the only important parameter for the characterization of a light source.

Another important parameter is the Correlated Colour Temperature (CCT), that indicates the equivalent temperature that a black body radiator would need to have in order to produce light of the same colour. The CCT can be calculated according to the McCamy approximation ([86, 87]) and with the most recent method developed by Javier Hernández-Adrés, Raymond L.Lee and Javier Romero ([88]). The MacCamy,

the Hernández-Adrés and other methods are showed in the appendix A. The values obtained are reported in Table 4.5. As one can notice, the values obtained from the two methods are in agreement if we consider an experimental error of about 5%. The largest discrepancy is obtained for sample G but in this case the CCT is also the lowest, and it is well known that both methods rely on a series of approximations that make the result less reliable when the colour temperature is lower than 3000 K. In Table 4.6 we report the CCTs and the chromatic coordinates for some standard emitters to be used for comparison with our results. The principal commercial light emitters chromatic features are shown in Table 4.7.

Table 4.5. Correlated colour temperature for every investigated sample calculate using the McCamy approximation ([86, 87]) and according to the most recent method developed by Javier Hernández-Adrés, Raymond L.Lee and Javier Romero([88]).

Host	Pr^{3+} doping(%) levels	CCT (K) [Mc Camy] [86, 87]	CCT (K) [Hern] [88]	label
BaY_2F_8	0.3	5411	5406	A
	0.5	5278	5288	B
	1.25	3304	3304	C
	2	4217	4222	D
	3	3578	3565	E
$LiLuF_4$	0.5	3872	3883	F
	1.25	2620	2573	G
	2	3405	3422	H
KYF_4	1.25	5006	5001	I
		5006	5001	L
KY_3F_{10}	0.3%	5269	5267	M

Confusingly enough, the concept of a colour temperature is somewhat contrary to what we would describe as "warm" or "cold" colours. The light produced by an incandescent lamp, for instance, has a low colour temperature, whereas daylight has a very high one. This is because when a body is heated up, its light goes through red, orange, yellow, white and finally blue as it becomes hotter and hotter. The CCT

temperature is defined warm below the 3300 K (red), intermediate from 3300 K to 5300 K and cold over 5300 K (blue). The calculated CCT exeeds the 5300 K only in sample A (0.3% $Pr^{3+}BaY_2F_8$)(Table 4.5), this is a quantitative indication of the slight pinkish colour of the samples we measured. The sample G (1.25%Pr:LiLuF) is the only that fall in the warm regions, while the others fall in the intermediate region.

The BaYF sample shows different CCT, covering with the different sample the intermediate regions, the sample A (0.3%) exceed in the cold regions for 100 K (5400 K) and the sample C (1.25%) is at the border between the warm and intermediate regions ($\sim$ 3300 K), the other crystals ranging in the interval defined by the two sample, also we observe that the two more diluted sample (0.3% and 0.5%) shows the colder light. The LiLuF samples have a warmer light, with a temperature ranging form 2620 K for the sample G (1.25%), to a maximum of 3872 K for the more dilute sample F (0.5%), this lattice has a warmer light compared with the other studied.

It is possible to observe that samples with a concentration lower than 0.5% have a CCT higher than 5200K with the exceptions of the LiLuF, but this lattice has a warmer light of the other studied. It is not easy to individuate a clear relation between concentration and CCT value, but from the two series of BaYF and LiLuF we can clearly see that the most diluted sample has the higher CCT, and the lower is for the 1.25% doped sample; even if for higher concentration the temperature increase again, it remain lower than the less doped sample.

4.5 Other dopants

The results obtained with the Pr^{3+} doped fluoride are very interesting, indeed we want to extend this kind of analysis on other rare earth dopants and in particular

Table 4.6. CIE Standard illuminants [41].

Description	CIE Coordinates (x,y)	Colour Temperature
Incandescent light	(0.4476, 0.4075)	2854 K
Direct sunlight	(0.3840, 0.3516)	4874 K
Indirect sunlight	(0.3101, 0.3162)	6774 K
Bright incand. light	(0.3457, 0.3586)	5000 K
Natural daylight	(0.3127, 0.3297)	6504 K
Normalized reference	(0.3333, 0.3333)	5500 K

Table 4.7. Chromatic characterization of the principal commercial white light sources [89] and Kodak catalogue.

Classification	Material	colour	CIE coordinates (x,y)
LED	InGaN/YAG	white:6500K	(0.31, 0.32)
	InGaN	blue	(0.13, 0.08)
	InGaN	blue-green	(0.08, 0.40)
	InGaN	green	(0.10, 0.55)
	InGaN	green	(0.17, 0.70)
	GaP:N	yellow-green	(0.45, 0.55)
	AlInGaP	yellow-green	(0.45, 0.54)
	AlInGaP	yellow	(0.57, 0.43)
	AlInGaP	red	(0.70, 0.30)
	GaAlAs	red	(0.72, 0.28)
Incandescent lamp	W-filament	white:2856K	(0.45, 0.41)
Fluorescence lamp	phosphor	white:6500K	(0.31, 0.33)
OLED low voltage		white	(0.29, 0.31)
OLED long lifetime tandem		white	(0.33, 0.35)
OLED high-efficiency tandem		white	(0.29, 0.32)

to Samarium (Sm^{3+}), and Europium (Eu^{3+}). The pumping scheme that we intend to analyse for the two dopants are:

- *Samarium* and Praseodymium energy levels are similar (see Figure 4.15(a)). Using a UV-LED the ions can be exited to the $^4F_{7/2}$ manifold. Once exited the

ions decay non radiatively, to the $^4G_{5/2}$ level. From this level it is possible to observe radiative transitions to the $^6H_{5/2}$ (green), to the $^4H_{7/2}$ (orange), and to the $^4H_{9/2}$, and $^4H_{11/2}$ (red).

- *Europium* can be exited using an UV-LED to the level $^5L_6$. Once exited the ion decade non radiatively to the level ^5D_i, with i=0,1,2,3. A further radiative decay to the level ^7F_j, with j=1,2,3,4 give rise to a series of emissions that cover the entire visible spectra.

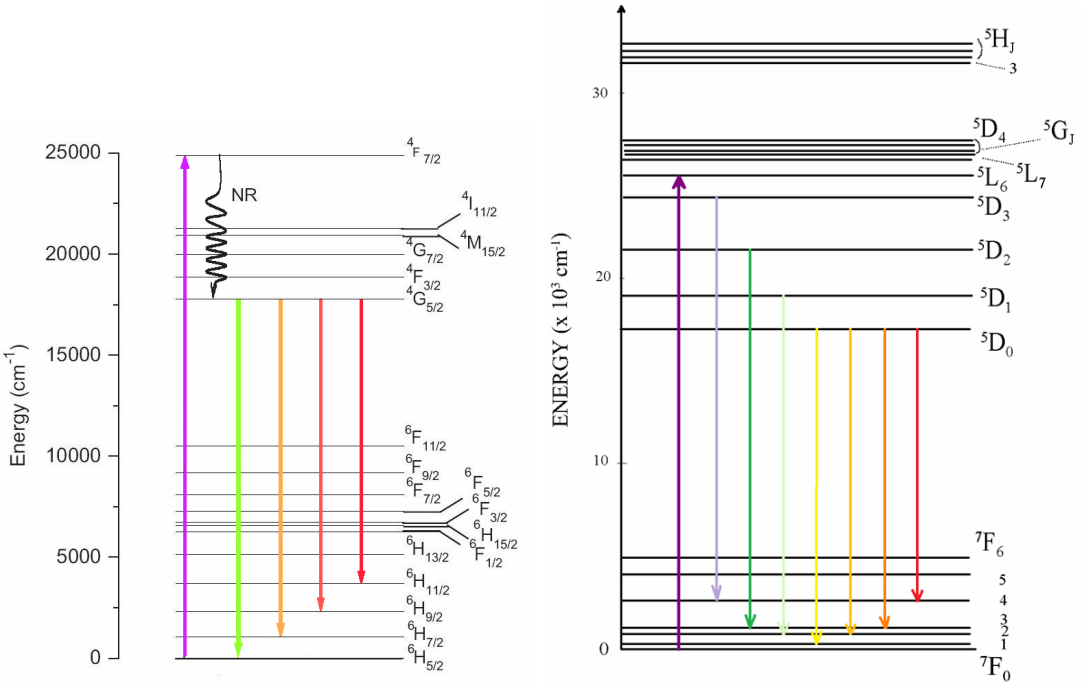

(a) Sm^{3+} energy levels [90] (b) Eu^{3+} energy levels [91]

Figure 4.15. Energy levels of Sm^{3+} and Eu^{3+} and studies transition

To test the behaviour of those two ions (Sm and Eu), we choose as host the crystal with which we had the best results when doped with Pr, the BaY_2F_8.

Crystals were grown using an home-made Czochralski furnace, oriented, and cut as previously described. The grown sample are 1% Sm^{3+}: BaY_2F_8, and 1% Eu^{3+}:

BaY_2F_8. Both have nearly parallelepiped shape and dimensions in the mm range.

Luminescence spectra were acquired at room temperature after pumping with the UVLED ($\lambda \sim 385$ nm FWHM ~ 15 nm). The setup for this measurements was similar to the one illustrated in the Figure 3.7.

The luminescence spectra of the Sm doped sample is reported in the Figure 4.16(a). In this spectra it is easy to identify the emissions of the Sm^{2+} already reported by Reisen and Kaczmarek [92]. Figure 4.16(b) shows a plot of the emission in the interval 680-730 nm, where these transitions are situated. The presence of these transition it is probably ascribable to the reduction of the Sm^{3+} ions in Sm^{2+} ions inside the crystal lattice. The reasons of such reduction are not already clear. Reisen *et al.* [92], suggested that the generation of stable Sm^{2+} centres can be ascribed to the X-ray excitation of the sample, that in our case, is performed during the orientation determination by X-ray backscattering Laue technique. However this behaviour was reported for nanoparticles and not for bulk crystals like our sample. A more reliable explanation is a reduction of the Sm^{3+} ions during the growth process, as already proved for other lanthanides, as for example in Yb doped fluorides [93].

As the emission of this sample is confined on the red side of the visible spectrum, with a colour coordinate of (0.58,0.41) calculated as described in 2.2.2, it is not a good candidate for white light. It could be interesting to study the behaviour of some codoped materials containing Sm^{3+}, or Sm^{2+}. The Eu^{3+} sample shows a large number of emission (Figure 4.17(a)), that covered all the visible spectra, and show a slightly yellowish-orange emission: x=0.41 y=0.34 (Figure 4.17(b)), calculated as described before in section 2.2.2. This crystal can be very interesting as visible emitter, also the great number of emission in the visible rage can lead to a good rendering, better than in the other crystals. As reported in [94], even Eu doped crystals emissions are affected by the reduction of the ion Eu^{3+} in Eu^{2+}, but differently from the case of Sm, the emission relative to the Eu^{2+} are concentrated

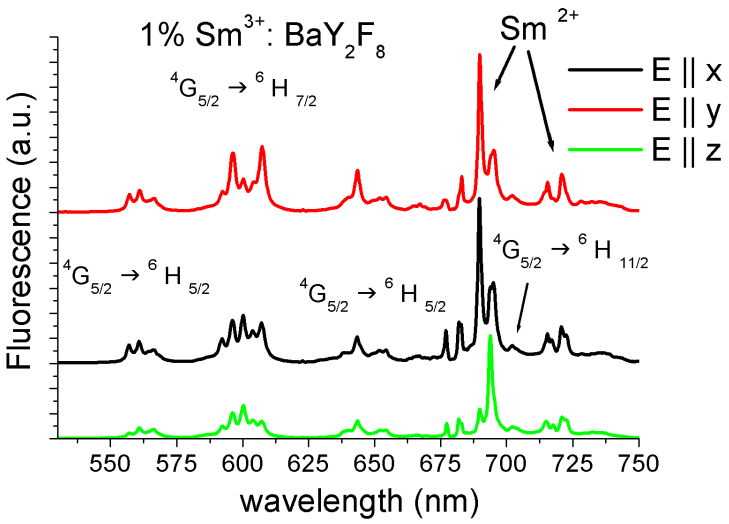

(a) visible spectra of $Sm^{2+/3+}$ sample

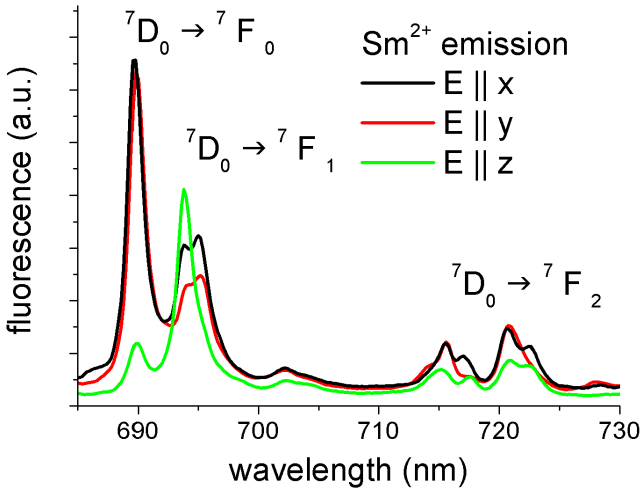

(b) Sm^{2+} emission

Figure 4.16. 1% $Sm^{3+/2+}$:BaY_2F_8 polarized fluorescence

in the UV region and do not affect the visible emission spectra.

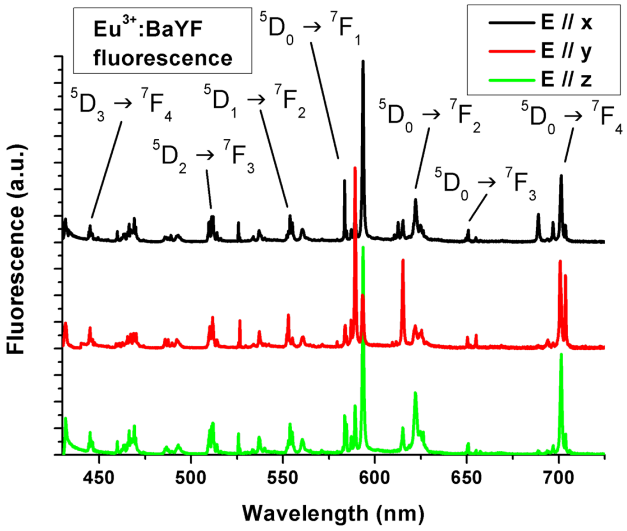

(a) polarized emission of Eu^{3+}

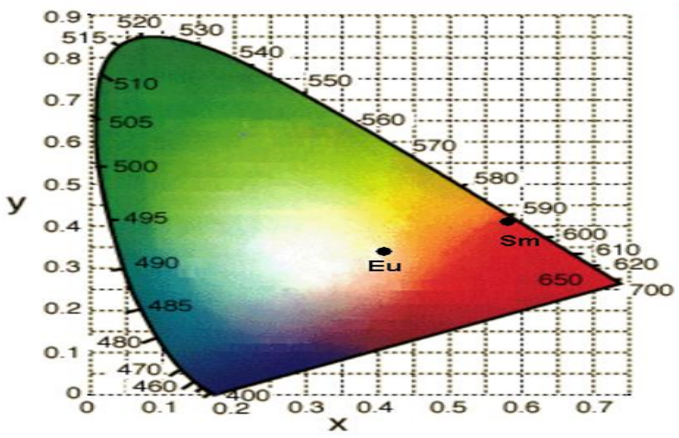

(b) CIE 1931 Colour coordinate of Sm an Eu doped samples

Figure 4.17. (a)1% Eu^{3+}:BaY_2F_8 polarized fluorescence (b) colour coordinate of the sample investigated.

As a further step in the characterization of these crystals, we evaluated the intrinsic efficiency. For that purpose we used the same experimental set-up used previously for the Pr doped crystals, with the only difference that in this case we used a GaN laser with emission at 405 nm, to stimulate the light emission of the

samples. Unfortunately with our set-up we were not able to register any fluorescence, because the efficiency is too low. From previous measurements we estimated that the precision of our set-up in measuring the intrinsic efficiency is of about the 5%, this means that we can estimate the EE of the Sm and Eu samples lower than 5%.

4.6 Conclusion

From the emission spectra, based on the CIE theory presented in Chapter 2, the CIE chromatic coordinates were calculated and reported in this section. From these values the corresponding correlated colour temperatures were calculated using the McCamy [86, 87] and the Javier Hernàndez-Adrès et al. [88] approximations (appendix A). As previously discussed the CIE coordinates calculated of our the samples are close to the white point (0.33, 0.33) on the CIE chromatic diagram. These results are very promising. Indeed the CIE coordinates are comparable with the more common light sources: incandescent filament and neon lamp. The CCT are in the range of the most common fluorescence lamps. It has to be noted that in the calculation of the CIE coordinates of the CCT calculations the pump radiation is not taken into account. In the measurement of the radiative emission, the pump source intensity was cut using a OG45 filter. This is, in fact, the hypothetical working condition of a future device, where the halo effect has to be minimized.

As previously mentioned, the CIE chromatic coordinates of our samples, are all pretty close to the white point at coordinates (0.33, 0.33). The sample that shows a set of coordinates closest to the white point is the 0.5% Pr^{3+}:BaY_2F_8 with (0.34,0.34). Unfortunately, the sample that shows the higher intrinsic efficiency measured (60 %) is the 1.25% Pr^{3+}:$LiLuF_4$ that shows the worse set of coordinates (0.44, 0.36). It has any way to be noted that this set of coordinates, although different from the ideal values, is comparable and better than the coordinates of incandescent

lamps commercial sources (0.45,0.41). Other samples with good set of chromatic coordinates (0.34, 0.35), are the 1.25% Pr^{3+}:KYF_4, and the 0.5% Pr^{3+}:BaY_2F_8. These samples shows both absorption and emission spectra broader than the for the other samples. This could be exploited to to create a more uniform white light source, than in case of more narrow emissions, even if this has not avoided the development of neon sources, that are characterized by the same kind of narrow emissions.

To obtain a broader emission spectrum, a possible solution is to incorporate in the same host, crystalline matrix or glass, powders of different crystals doped with trivalent Pr . In this way, the different shift in the Pr^{3+} energy levels caused by the different external crystal field can produce a boarder emission spectrum. Since the shift due to the crystalline field is not so large, to cover a wavelength region without any emission line, we could insert also other doping rare earth ions with emission in the missed interval. As deducible by the spectra the trivalent Pr lacks of transition in the green spectral region of which the trivalent Er is reach, so good rendering can be achieved by inserting Er ions in the crystal matrix.

We also try to extend this kind of analysis on different dopant, in particular Europium and Samarium, but with our equipment we were not able to estimate the efficiency of the samples. The low efficiency of the sample could be ascribed to the presence of Sm and Eu in the bivalent form, this obviously reduce the efficiency of the sample, increasing the non radiative processes inside the crystals. A solution to avoid reduction process of these dopants could be the growth in CF_4 atmosphere, as already reported for Yb doped crystals, for which a similar behaviour was observed [95]. Future work will be devoted to improve the growth process of crystals hosting Sm and Eu ions. Moreover, an interesting use of the properties of the bivalent Sm ions, could come from the coupling with other dopants, even if the emissions in the red spectral range of this ions, does not solve the lack of green transitions for the Pr ions.

Chapter 5

KYF_4: Praseodymium

In this chapter are reported the results of a spectroscopic investigation on 1.25%at Pr^{3+}:KYF_4. Particular attention was dedicated to the effects of the multisite disordered nature of the crystal, on the optical properties. Some of the phenomena observed that are more deeply analysed are the broadening of the ^3P_J absorption lines, at room temperature, and the 570-665 nm orange-red polarized emissions obtained pumping the $^3P_2$ and $^3P_1$+$^1I_6$ manifolds, respectively at 445 and 457 nm. The $^3P_0$ lifetime was in agreement with that measured in other fluoride hosts. Moreover is is analysed the unpolarized emission as a function of the temperature in the range 300-700 K, which allowed an evaluation of a phonon energy of around 350 cm^{-1}

5.1 Absorption

A spectroscopic characterization of the crystal focusing the attention to the visible region was performed. The first measurements performed are the room temperature polarized absorption, between 420-500 nm that involves the $^3H_4 \rightarrow ^3 P_J$ transitions, pumping in all the three possible polarization: E parallel to c axis (π), E parallel to a axis (σ), E orthogonal to bot c and a axes (α). As it was expected the absorption

peaks are broader due to the multisite-disordered crystalline structure. The Pr:KYF polarized absorption spectra was already investigated in detail in [96] where it was possible to put in evidence the effect of the multisite-disordered host. To highlight once more this behaviour, in Figure 5.1 is shown a comparison between the absorption spectra in π polarization of KYF_4 and $LiLuF_4$, both doped with 1.25at% of Pr^{3+}. The black arrows pointing at the spectra curves shows the wavelength of the pump source used to acquire the luminescence spectra.

In particular it is possible to see that the $^3P_0$ singlet absorption is actually a single line in the ordered $LiLuF_4$ matrix but it exhibits a more complex structure in KYF.

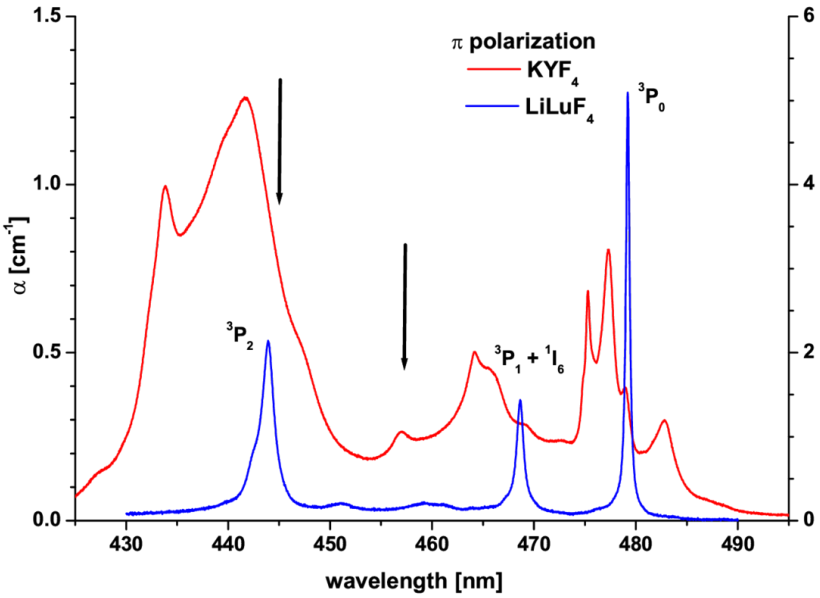

Figure 5.1. Comparison between the room temperature absorption, in π polarization, of KYF_4 (left axis) and $LiLuF_4$ (right axis). The level assignment refers to $LiLuF_4$.

From the comparison it is evident the multisite-disordered crystalline structure, in fact the lines are multiples and broadened. The absorption coefficients

at the pump wavelengths,in $\pi(\sigma)$ polarizations, are 0.74(0.81) cm^{-1} at 445 nm and 0.26(0.33) cm^{-1} at 457 nm. Due to the crystal symmetry the absorption coefficient in α polarization is very close to the σ one, with a difference smaller than 10%.

5.2 Fluorescence: diode vs argon

In this section the fluorescence measurements results are shown and discussed. More specifically are shown the room temperature fluorescence spectra, and the fluorescence as a function of the temperature.

Because the multisite-disordered nature and the crystal symmetry of the sample under investigation, the polarized fluorescence measurement have been performed, exciting with the pump polarization parallel to the a axis (σ polarization). Two different pump sources were used to excite the sample at two different wavelength: 445 nm with a laser diode, to pump the $^3P_2$ manifold, and 457 nm with an Ar-laser, to shift to the $^3P_1$+$^1I_6$ manifolds (see Figure 5.2). The pump power in the two cases was close to 12 mW.

It was observed that the influence of the different pump on the emission is particularly evident in the green and red regions [96]. For sake of clarity, I will show all the spectra limited to the yellow-red emission in the range 570-665 nm. As a starting point in Figure 5.3 is shown the fluorescence observed at σ, π and α polarization excited at 445 nm, relative to the transitions $^3P_0 \rightarrow {}^3H_6$ and $^3P_0 \rightarrow {}^3F_2$ (red arrows in Figure 5.2). Around 600 nm falls the $^1D_2 \rightarrow {}^3H_4$ transition too. In order to detect a possible contribution of $^1D_2$ manifold to the peaks around 600 nm, the lifetime of the main emissions centred at 595 and 606 nm, as reported in the following, were measured.

In Figure 5.3 it is possible to observe a line broadening with respect to an ordered host like LLF [71], together with the expected intensity variation due to the

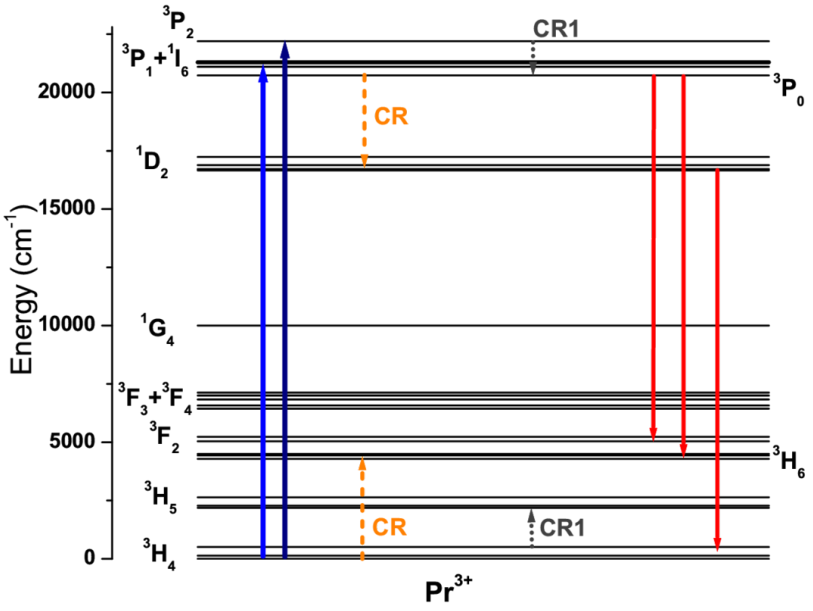

Figure 5.2. Simplified Pr^{3+} energy level scheme. Arrows indicate the pump wavelengths and the main transitions discussed in the paper.

symmetry selection rules. It is interesting to see that some of the emission lines are not broadened and their width is around 1 nm, which is comparable with those of LLF. This behaviour, that is presently under investigation, is presumably due to ions in a ordered position in the lattice or in a single site occupation. These features are peculiar of this host matrix. The same spectral region, observed pumping at 457 nm, exhibit a distinctly different behaviour. Figure 5.4 reports the emission for the same three different crystal orientations. Even if the absorption at 445 and 457 nm differs roughly of a factor 4, it is evident that the behaviour is opposite compared to Figure 5.3 with an inversion between the intensities of 595 and 606 nm peaks, while the line shape is the same.

To highlight this difference Figure 5.5 shows a direct comparison between the fluorescence spectra observed in σ polarization, where this effect is more pronounced.

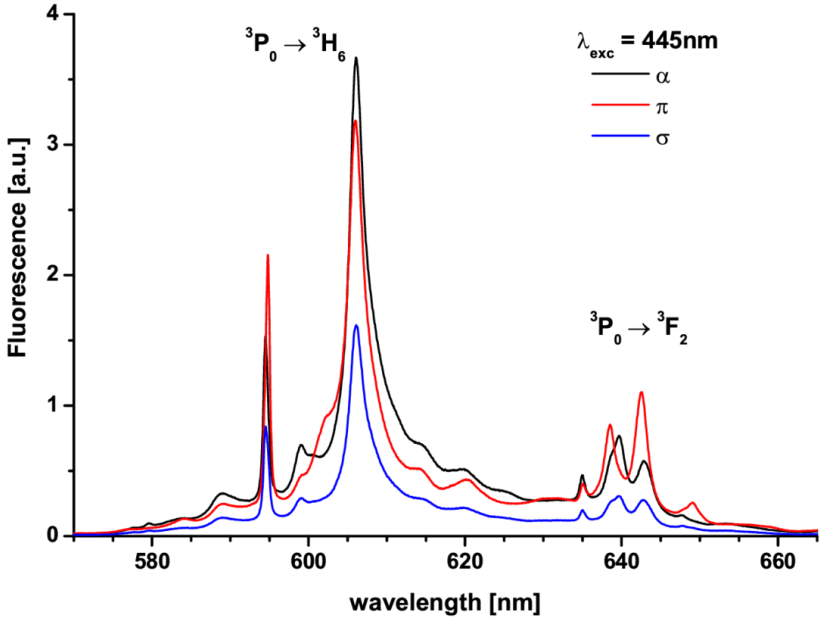

Figure 5.3. Polarized room temperature fluorescence pumping with the diode laser.

To take in account the different absorption coefficients at 445 and 457 nm the fluorescence has been opportunely scaled.

A possible explanation of the emission increase at 595 nm, exciting at 457 nm, could be based on a cross-relaxation mechanism between $^3P_0$ - $^1D_2$ and $^3H_4$ - $^3H_6$ which populate the $^1D_2$ manifold which decays to $^3H_4$ emitting around 595 nm (CR orange arrows in Figure 5.2). To check this hypothesis the lifetime of this line was measured. In fact the expected lifetimes are quite different, around 50 μs for the $^3P_0$ manifold and 300 μs for the $^1D_2$ one [97], allowing their discrimination. The lifetime measurements have been performed exciting the sample at 445 and 457 nm, and observing at 594.5 and 606 nm. The observation wavelengths correspond to the peaks marked with an arrow in Figure 5.5 and the resolution of the measurements apparatus was set in order to avoid a superposition between the two observation windows.

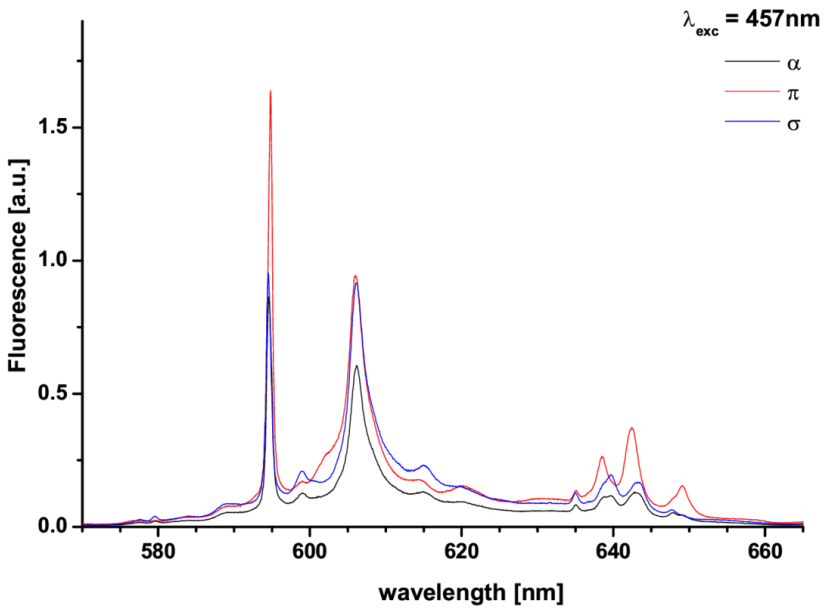

Figure 5.4. Polarized room temperature fluorescence pumping with the argon laser.

The decay curves are single exponential, within errors, and the measured lifetime values are those proper of $^3P_0$ manifold, in agreement with the values reported in [98, 97], summarized in Table 5.1.

Table 5.1. Lifetime values observed in KYF:Pr exciting at two different wavelength, 445 and 457 nm. The decay curves were recorded relatively to the two main emission peaks.

λ_{exc}(nm)	λ_{obs}(nm)	$\tau(\mu s)$
445	594.5	49(2)
	606.0	50(2)
457	594.5	46(2)
	606.0	49(2)

So the difference could be due to a symmetry selection rule. In fact pumping with the diode laser the manifold $^3P_2$ is populated, and the $^3P_0$ is populated by a cross-relaxation between $^3P_2$ - $^3P_0$ and $^3H_4$ - $^3H_5$ plus a multi-phonon relaxation (CR1

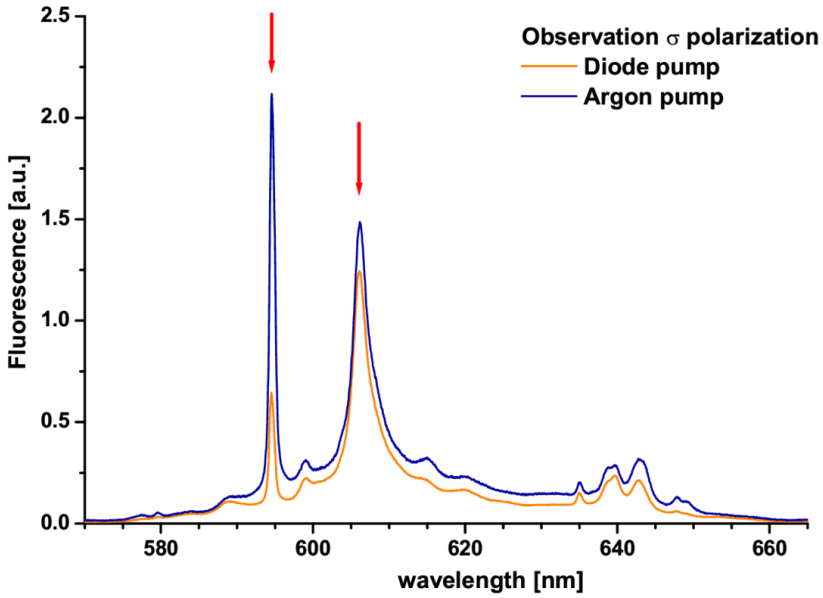

Figure 5.5. Room temperature fluorescence in σ polarization pumping with both argon and diode lasers. The red arrows indicate the observation wavelength in lifetime measurements.

grey arrows in Figure 5.2) . On the contrary, exciting at 457 nm, the $^3P_0$ manifold is only populated by the multi-phonon relaxation only. It can be hypothesize that this different population mechanism could favour the excitation of one of the possible $^3P_0$ sites whose symmetry enhance the 595 nm emission.

5.3 Fluorescence: temperature behaviour

The study of the luminescence as a function of temperature allow an estimation of the phonon energy of the host that, to our knowledge, has not yet been measured. A second important aspect is the temperature analysis of the laser media. In fact it is very important to understand the laser performances under strong pumping regime. The fluorescence behaviour between 300-700 K, that is a typical temperature of

the active volume in laser media, was investigated. As for the room temperature measurements both argon and diode pump sources was used. The holder of the heated cell allowed a fixed crystal position, forcing us to pump with the polarization parallel to the c axis (π polarization). Even if the pump polarization differ from that utilized until now, it does not affect the results. In fact we are interested in the influence of multiphonon relaxation processes on the luminescence and they are independent from optical selection rules so they give the same contribution independently from the pump polarization. The experimental results are shown in Figure 5.6, and 5.7 for diode and argon pump respectively.

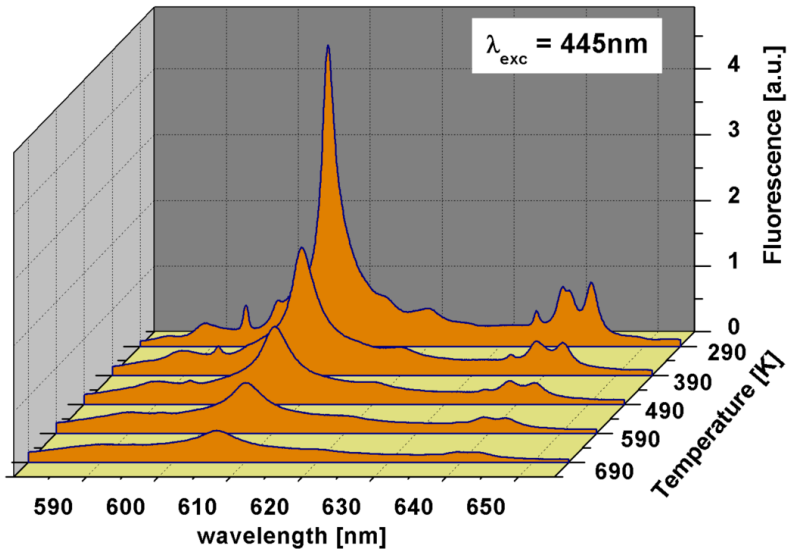

Figure 5.6. Unpolarized fluorescence vs temperature pumping with diode laser.

As it was expected the fluorescence intensity decrease with increasing temperature due to the multi-phonon relaxation processes [99, 100] In order to evaluate the temperature dependence of the fluorescence, we have selected the band around 600 nm, mainly involved in the pumping effect above described. The fluorescence spectra were integrated between 580 and 630 nm and the peaks area are reported

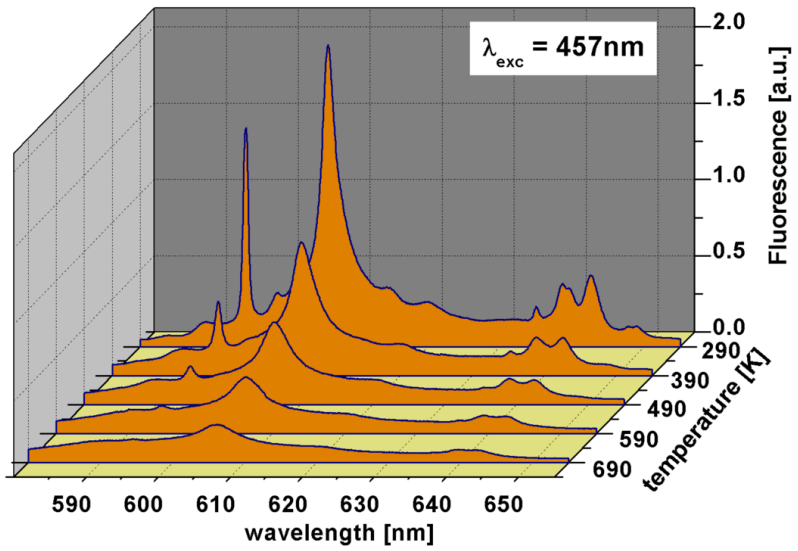

Figure 5.7. Unpolarized fluorescence vs temperature pumping with argon laser.

in an Arrhenius plot. In our case temperature acts as a de-activation process, in the fact multi-phonon relaxation subtract population from the upper level, and the slope is positive on the contrary to the usual Arrhenius behaviour for activated processes. The slope is a parameter that should be host dependent, so the energy that is involved in the Arrhenius equation should be strongly linked to the crystal phonon energy. In fact the fluorescence intensity is proportional, apart a geometrical factor, to the fluorescence quantum yield

$$\Phi = \frac{\int (P(t)/h\nu)dt}{N_2(0)V} = \frac{\tau}{\tau_r} \tag{5.1}$$

where P(t) is the spontaneously emitted power at time t, $N_2(0)$ is the population at t=0 ($^3P_0$ in particular), V is the volume of the material and τ_r is the radiative lifetime. If we consider τ as the inverse of the multiphonon rate [99, 100]

$$W(T) = W_s(\bar{n} + 1)^p \tag{5.2}$$

where W_s represent the spontaneous emission rate and p is the number of phonons involved, it is possible to infer the temperature dependence of the fluorescence intensity as

$$I(T) \propto (1 - e^{-\frac{\Delta E}{KT}})^p \tag{5.3}$$

where $\Delta E = h\nu_{ph}$. So for $\Delta E \gg KT$ we expect an Arrhenius behaviour with positive slope. As it is possible to see in Figure 5.8 the slope is fairly linear in the right end of the graph, that means low temperature, and it is present a deviation in the left end where $h\nu_{ph} \sim KT$. From the fitting of the data in Figure 5.8 we can estimate a $\Delta E_D \approx \Delta E_A = 350 \pm 30$ cm^{-1} for diode and argon pump, in agreement with the usual phonon energy in fluorides [52]. The reported error is the outcome of the fitting procedure. As underlined above it is the first evaluation of the phonon energy for this material.

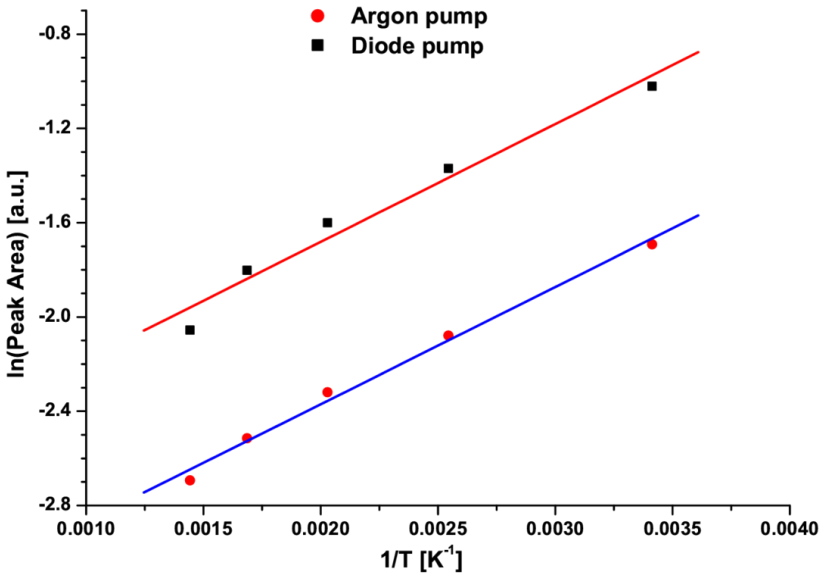

Figure 5.8. Arrhenius plot of the peak area pumping with both argon and diode lasers.

5.4 Conclusion

A spectroscopic characterization of 1.25at%Pr^{3+}:KYF_4 as a function of temperature has been presented. The broadening of the ^3P_J absorption lines due to the multisite-disordered nature of the sample and a comparison with an ordered host, at room temperature, is reported. Moreover it has been performed a detailed study of the 570-665 nm orange-red polarized emissions pumping the $^3P_2$ and $^3P_1$+$^1I_6$ manifolds at 445 and 457 nm respectively, in order to explain the peculiar behaviour of this host. The lifetime relative to the emission peaks around 594 and 606 nm correspond to the $^3P_0$ one for both peaks, in agreement with the values measured in other fluoride hosts. In order to evaluate the influence of local temperature increase in high power pumping regime on laser performances, the unpolarized emission in the temperature range 300-700 K was investigated. The analysis of the emission peaks area allowed an evaluation of KYF_4 phonon energy around 350 cm^{-1} in agreement with the literature values for fluoride crystals.

Chapter 6

$Ba_2NaNb_5O_{15}$ Praseodymium

In this chapter is presented the characterization of the $Ba_2NaNb_5O_15$ (BNN) Pr doped crystal. My contribution to this work was limited to the optical spectroscopy measurements (dynamical and steady state) of the crystal, and to the discussion of the results. The crystal was growth by E. Cavalli at the University of Parma, while the structural analysis of the sample was performed by G. Calestani at the University of Parma. All the data at our disposal are here presented in order to allow the understanding of the spectroscopic behaviour of the crystal.

$Ba_2NaNb_5O_{15}$ (BNN) belongs to the family of the niobates with tungsten bronze (TB) structure. These compounds have attractive photorefractive, ferroelectric and nonlinear optical properties [101]. BNN is also an interesting host material for luminescent ions. Nd^{3+}-doped crystals have been investigated in order to develop self-doubling laser media [102, 103]. Studies extended to BNN activated with Yb^{3+} [104], Er $^{3+}$ [105], Tm^{3+} and Ho^{3+} [106, 107] have confirmed its potential as a host lattice for laser ions. We have recently explored the visible emission properties of BNN crystals activated with Eu^{3+},Dy^{3+},Tb^{3+} and Sm^{3+} [108], pointing out the issues concerning the site occupancy in this host lattice and the analogies with SBN: Ln^{3+} (Ln^{3+} = rare earth ions). The spectroscopic work is focused on the investigation

of the emission properties of Pr^{3+}-doped BNN crystals as a function of the temperature, the doping concentration and the excitation conditions. The interest in this system is related to different interconnected aspects: the development of a new visible emitting material, the analysis of its excited states dynamics and of the interactions between optical centres and lattice constituents in light of the structural properties of the host and of the Pr^{3+} site occupancy, the possibility of extending the obtained information to other members of the TB niobate family, and so on.

6.1 Structural characterization

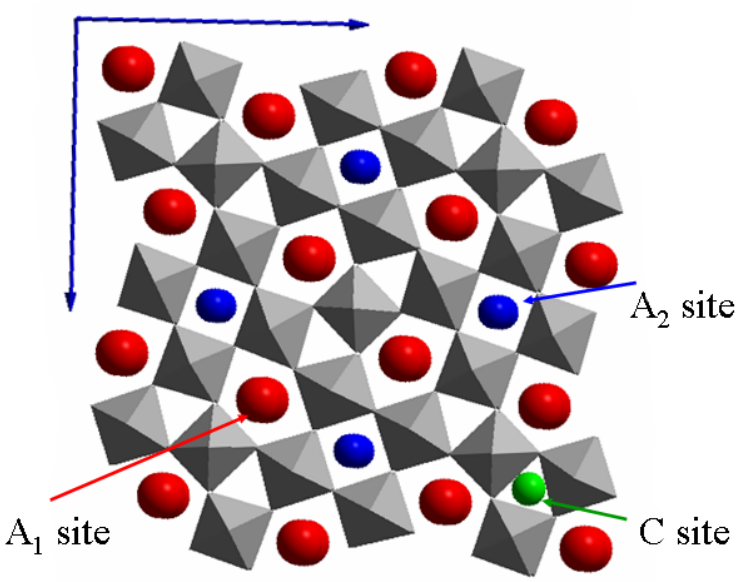

Figure 6.1. TTB structure with the conventional sites nomenclature.

Three single crystals with nominal Pr/Ba ratios 0.5%, 2% and 8% were characterized by single crystal XRD. Crystal data are very similar, as reported in Table 6.1, and are consistent with the typical tetragonal tungsten bronze (TTB) structure, characterized by the structural formula $(A_1)_x\ (A_2)_yC_zB_{10}X_{30}$, where x can ideally

vary in the 0-2 range and y,z in the 0-4 range. The typical framework (Figure 6.1) can be thought of as being derived from the perovskite structure by rotation of some [BX_6] polyhedra and is formed by corner sharing [BX_6] octahedral units whose linking produces three different types of channels (also called tunnels) containing the extra-framework cations in A_1,A_2 and C sites, respectively. In terms of coordination polyhedra, the A_2 cations are 15-fold coordinated in the tunnel with a pentagonal section, the A_1 cations are 12-fold coordinated in the surviving perovskite cage, and the C cations are 9-fold coordinated in channels characterized by a triangular section. In the studied case the structure was solved with SIR2002 [109] and refined with SHELX97 [110].

Table 6.1. Crystal data.

Compound	Pr:BNN (0.5%)	Pr:BNN (2%)	Pr:BNN (8%)
Formula weight	998.92	999.12	998.67
Crystal habit	needle	needle	needle
Crystal colour	colourless	colourless	colourless
Crystal dimensions, mm	0.53 x 0.07 x 0.05	0.41 x 0.07 x 0.07	0.50 x 0.08 x 0.08
Crystallographic system	tetragonal	tetragonal	tetragonal
Space group	P4bm	P4bm	P4bm
Cell parameters:			
a, Å	12.465(5)	12.464(4)	12.463(4)
c, Å	3.986(2)	3.986(2)	3.984(2)
α, °	90	90	90
β, °	90	90	90
γ, °	90	90	90
V, Å^3	619.3(5)	619.2(4)	618.8(4)
Z	2	2	2

After a preliminary structure refinement in which only the presence of Ba^{2+} and Na^+ (located in A_2 and A_1, respectively) as extra-framework cations was taken into account, different Fourier maps revealed in all cases a residual electron density in the triangular channels, suggesting partial cationic occupation of the corresponding

Table 6.2. Atomic coordinates and displacement parameters (Å).

Atom	multiplicity	x	y	z	U_{eq}	Site occupancy
Pr : BNN (0.5%)						
Nb2	2	0.0000	0.5000	0.5000	0.00457(17)	1
Nb1	8	0.074 04(3)	0.20942(3)	0.4994(6)	0.00176(13)	1
Ba2	8	0.3357(3)	0.1787(3)	0.0132(6)	0.0115(7)	0.4845(13)
Na1	2	0.0000	0.0000	0.007(3)	0.0074(7)	1
Pr2	4	0.1128(15)	0.3872(15)	0.051(7)	0.010	0.0183(16)
O1	8	-0.0064(3)	0.3437(3)	0.546(3)	0.0173(14)	1
O2	4	0.2160(3)	0.2840(3)	0.536(3)	0.0081(13)	1
O3	8	0.1410(4)	0.0698(3)	0.558(2)	0.0193(15)	1
O41	8	0.0914(10)	0.1952(9)	0.033(5)	0.0230(19)	0.50
O42	8	0.0572(10)	0.2150(10)	0.044(4)	0.0230(19)	0.50
O5	4	0.0141(7)	0.4859(7)	0.018(8)	0.020(3)	0.50
Pr : BNN (2%)						
Nb2	2	0.0000	70.5000	0.5000	0.00531(15)	1
Nb1	8	0.074 10(3)	0.209 39(3)	0.4971(6)	0.002 17(11)	1
Ba2	8	0.3365(2)	0.1793(2)	0.0103(7)	0.0105(5)	0.4809(12)
Na1	2	0.0000	0.0000	0.001(3)	0.0175(12)	0.970(4)
Pr1	2	0.0000	0.0000	0.001(3)	0.0175(12)	0.031(4)
Pr2	4	0.1162(19)	0.3838(19)	0.054(9)	0.010	0.0131(14)
O1	8	-0.0063(3)	0.3438(3)	0.544(3)	0.0172(13)	1
O2	4	0.2163(3)	0.2837(3)	0.536(3)	0.0073(13)	1
O3	8	0.1414(3)	0.0698(3)	0.555(2)	0.0192(15)	1
O41	8	0.0904(9)	0.1959(9)	0.025(6)	0.0258(19)	0.50
O42	8	0.0584(9)	0.2153(9)	0.033(5)	0.0258(19)	0.50
O5	4	0.0144(6)	0.4856(6)	0.023(6)	0.016(3)	0.50
Pr : BNN (8%)						
Nb2	2	0.0000	0.5000	0.5000	0.00611(12)	1
Nb1	8	0.07395(2)	0.209 72(2)	0.5031(5)	0.00527(8)	1
Ba2	8	0.33566(16)	0.178 68(17)	0.0146(5)	0.0139(4)	0.4720(10)
Na1	2	0.0000	0.0000	0.007(2)	0.0138(7)	0.920(4)
Pr1	2	0.0000	0.0000	0.007(2)	0.0138(7)	0.080(3)
Pr2	4	0.112(2)	0.388(2)	-0.025(15)	0.010	0.0084(13)
O1	8	-0.0065(3)	0.3436(3)	0.542(3)	0.0275(18)	1
O2	4	0.2162(3)	0.2838(3)	0.540(4)	0.017(2)	1
O3	8	0.1404(3)	0.0691(3)	0.554(4)	0.036(3)	1
O41	8	0.0909(8)	0.1962(8)	0.037(5)	0.0280(17)	0.50
O42	8	0.0568(8)	0.2139(8)	0.037(5)	0.0280(17)	0.50
O5	4	0.0131(6)	0.4869(6)	0.044(5)	0.020(3)	0.50

C sites. Since these residuals were not detected in undoped BNN crystals characterized previously, a possible site occupation by praseodymium was considered. Owing to the reduced cage dimension, this hypothesis could appear quite rash, unless to evaluate carefully the local effects produced by structural modulation. In fact TTB structures, known for a great number of oxides and fluorides, are usually characterized in the low temperature region of the phase diagram (very often extending well above RT) by a typical structural modulation along the [1 1 0] crystallographic direction, ranging from incommensurate to commensurate depending on chemical composition and connected to the doubling of the c parameter($\sim$8Å). The structural modulation, ascribed to the existence of a cooperative tilt of the [NbO_6] octahedra that reduces the real symmetry from tetragonal to orthorhombic, is at the basis of ferroelasticity in these systems.

The fundamental averaged structure of BNN at room temperature was determined at the end of the 1960s by Jamieson et al [111].

Table 6.3. Selected bond lengths and distances (Å).

	Pr : BNN (0.5%)	Pr : BNN (2%)	Pr : BNN (8%)
Nb2-O5	1.94(3)	1.92(2)	1.831(18)
Nb2-O1	4 x 1.958(4)	4 x 1.956(4)	4 x 1.958(4)
Nb2-O5	2.08(3)	2.10(2)	2.179(18)
Nb1-O42^a	1.830(17)	1.86(2)	1.870(19)
Nb1-O41^b	1.88(2)	1.90(2)	1.88(2)
Nb1-O3	1.944(4)	1.945(4)	1.949(4)
Nb1-O1	1.960(4)	1.961(4)	1.953(3)
Nb1-O3	2.000(4)	1.997(4)	1.991(4)
Nb1-O2	2.004(2)	2.006(2)	2.005(2)
Nb1-O41^a	2.15(2)	2.12(2)	2.14(2)
Nb1-O42^b	2.181(18)	2.15(2)	2.138(19)
Na1(Pr1)-O3	4 x 2.655(10)	4 x 2.651(10)	4 x 2.657(12)
Na1(Pr1)-O41	4 x 2.688(11)	4 x 2.690(11)	4 x 2.698(10)
Na1(Pr1)-O42	4 x 2.777(12)	4 x 2.783(11)	4 x 2.761(10)
Pr2-O5	2.24(3)	2.31(4)	2.22(4)
Pr2-O41^a	2 x 2.41(2)	2 x 2.37(2)	2 x 2.42(3)
Pr2-O42^b	2 x 2.26(2)	2 x 2.22(2)	2 x 2.29(2)
Pr2-O1	2 x 2.53(2)	2 x 2.53(3)	2 x 2.34(5)
Pr2-O1	2 x 2.56(3)	2 x 2.59(3)	2 x 2.76(5)
Pr2-O2	2.65(3)	2.61(4)	2.53(5)
Pr2-O2	2.74(3)	2.72(4)	2.91(5)
Pr2-Nb (av.)	2.89(3)	2.91(4)	2.88(5)
Pr1-Nb (av.)	3.412(7)	3.412(8)	3.413(5)
Pr-Nb weighted av.	2.89(3)	3.18(2)	3.319(12)

Note: Bonds denoted by *a* and *b* superscripts represents possible alternatives produced by the disordered description of the modulation in the fundamental cell.

The first attempt to describe the modulated structure was made by Lin and Bursill [112] on the basis of electron diffraction (ED) data in an orthorhombic supercell with a≈ b ≈ $2a_{TTB}\sqrt{2}$, c = $2c_{TTB}$ and space group *Im2a*. Further studies on detwinned crystals by Labbè et al [113] demonstrated that the supercell describing the quasi-commensurate modulation is in reality half in volume, being b ≈ $a_{TTB}\sqrt{2}$, and

its symmetry is consistent with the *Bbm2* space group. The results of Labbè were then confirmed by Fabbrici et al. [114] for $K_{0.525}FeF_3$ and by Mezzadri et al [115] for $K_{0.6}FeF_3$, confirming this modulation as generally distinctive of TTB phases and not only of BNN. The use of detwinned crystals revealed to be fundamental in structural studies of BNN,where ferroelastic domains connected to the exchange of the a and b axes of the superstructure occur on a scale that is below the coherence length of the x-ray, so that the modulation satellites are usually observed only by ED. In spite of the typical absence of modulation satellites, the existence of the structural modulation leaves a characteristic trace in single crystal XRD data, consisting of an anomalous elongation of the anisotropic displacement parameters of the atoms that is indicative of static disorder. The phenomenon is particularly significant for the apical O atoms of the [NbO_6] octahedra (the most affected by the cooperative tilt) and for the Ba atoms hosted in the large pentagonal channels (that moves in the ab plane in agreement with the displacements of the apical O atoms lying on the same plane). Once the structural modulation is taken into account (at least partially) by refining these atoms on disordered positions, the triangular channels become able to host Pr^{3+} ions (Figure 6.2).

Following this idea, the occupancies of the extra-framework cations were refined in the final cycles by constraining the total charge to compensate the anionic framework. The Pr^{3+} concentration of the most diluted crystal estimated by this approach significantly exceeds the nominal doping level and cannot be considered quantitatively reliable. Nevertheless, these results allow us to conclude that in this sample praseodymium occupies the C site, compensating a small Ba deficiency in the A_2 site. The presence of some Pr^{3+} in the A_1 site of BNN: Pr (0.5%) cannot be ignored. However, being the refined occupancy of the order of the standard deviation, the Na occupancy of the A_1 site was fixed to the unit in the last refinement cycles. The occupation of the C site by Pr is probably forced by the large Na excess in the flux

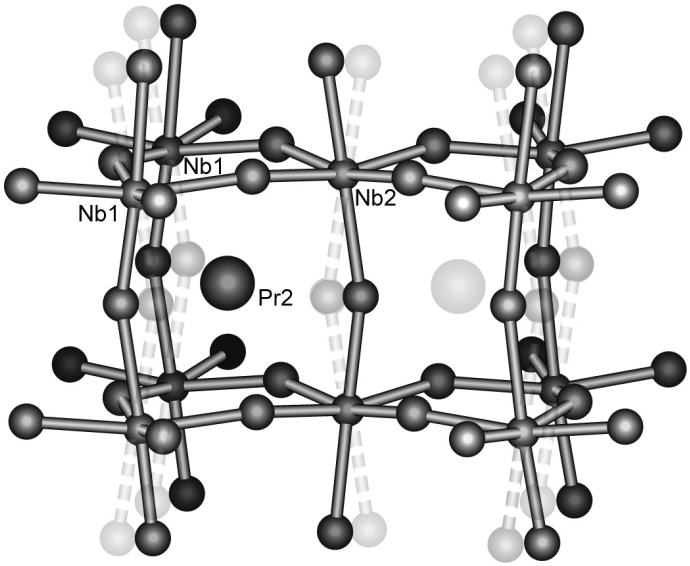

Figure 6.2. Configurations of the triangular channels resulting from the modulation of the BNN structure and allowing the accommodation of the Pr^{3+} ions in the C site

that inhibits the competitor role of Pr for the A_1 site. As the doping level increases Pr $^{3+}$ starts to preferentially occupy the A_1 site as is usual for lanthanides in TTB structures, decreasing its occupancy in the C site. Atomic parameters are reported in Table 6.1 selected bond lengths are reported in Table 6.3. In Table 6.2 and 6.3 we have indicated with Pr_1 and Pr_2 the Pr^{3+} ions located at the A_1 and C sites, respectively. The distribution of Pr^{3+} over the two sites influences the shortest Pr-Nb distance that represents a critical spectroscopic parameter, that it is reflects in the IVCT (Inter Valence Charge Transfer) analysed below .

6.2 10 K emission spectra

The 10 K polarized emission spectra of 0.5%, 2% and 8% Pr : BNN measured upon 476.5 nm CW laser excitation are shown in Figure 6.2 and Figure 6.4. They are composed of four emission manifolds: the intense $^3P_0 \rightarrow ^3H_4$ transition at 495 nm, the weak $^3P_0 \rightarrow ^3H_5$ multiplet at around 550 nm, a complex band system in the 600-670 nm range, including the $^1D_2 \rightarrow ^3H_4 (\sim 605\ nm)$,$^3P_0 \rightarrow ^3H_6$ (610-650 nm) and $^3P_0 \rightarrow ^3F_2$ (650-670 nm) transitions, and the weak $^3P_0 \rightarrow ^3F_{3,4}$ emission at around 750 nm.

The intensity ratio between the observed manifolds as well as the polarization behaviour of their components change with the doping level. This in our opinion is the consequence of the presence of different (and interacting) optical centres whose relative concentrations vary with the total Pr^{3+} content independently from one another. As expected, all features are inhomogeneously broadened, the sharpest ones having FWHM (full width at half maximum) values of the order of 30-40 cm^{-1}.

The broadness of the emission features depends on the excitation wavelength: as an example, Figure 6.5 compares the emission spectra measured upon 476.5 and 458 nm laser excitation. The latter is significantly broader, indicating that the 458 nm radiation excites a number of non-equivalent centrers larger than that excited by the 476.5 nm one. It is clear from Figure 6.6 that the relative intensity of the $^1D_2 \rightarrow ^3H_4$ emission transition strongly decreases with the doping level. This is an expected result, since the emission properties of Pr^{3+}-doped compounds are significantly affected by the activator concentration. In the case of the $^3P_0$ level the concentration quenching is ascribed to cross relaxation processes of the type [116]:

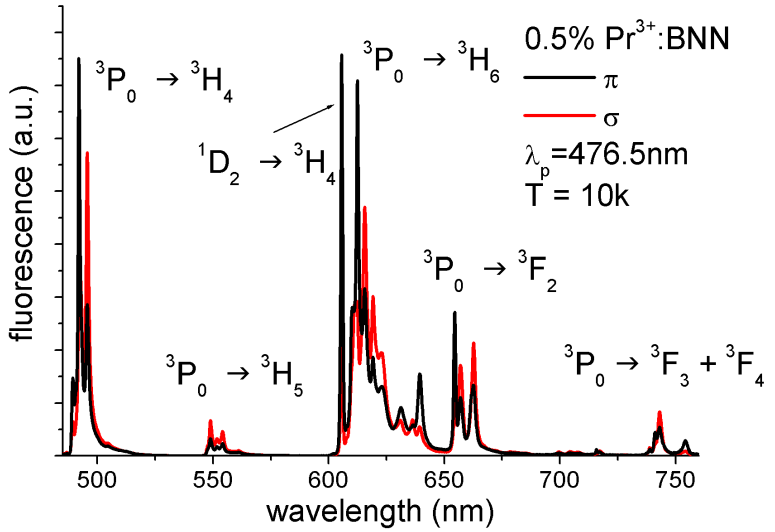

(a) 0.5% at Pr^{3+}

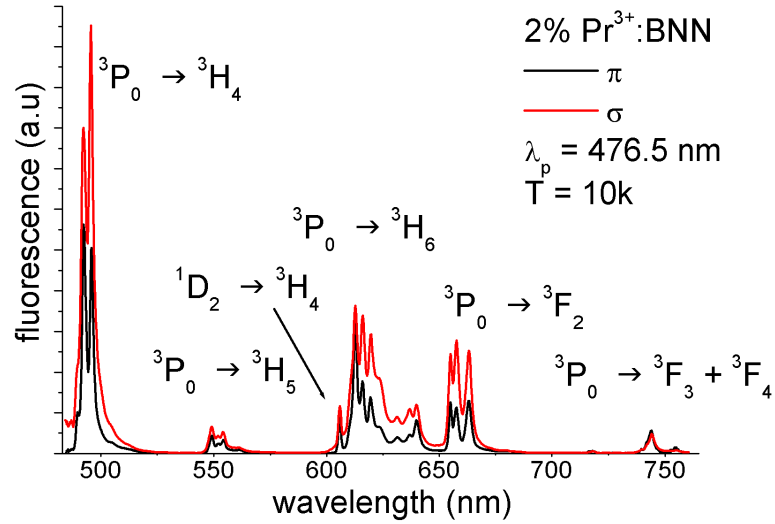

(b) 2.0%at Pr^{3+}

Figure 6.3. Polarized emission spectra of Pr BNN samples measured upon 476.5 nm laser excitation.

$$[^3P_0, {}^3H_4] \rightarrow [^1G_4, {}^1G_4]; \tag{6.1}$$

$$[^3P_0, {}^3H_4] \rightarrow [^1D_2, {}^3H_6]. \tag{6.2}$$

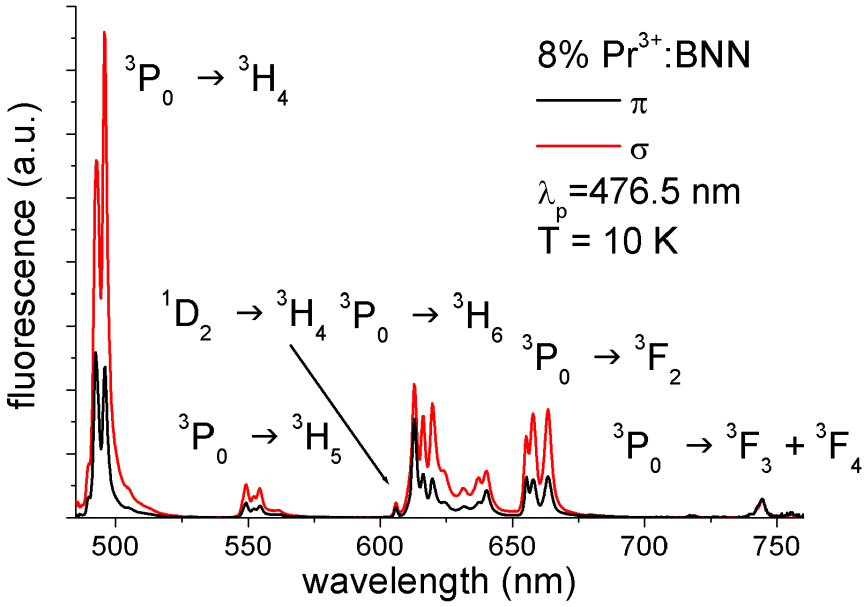

Figure 6.4. Polarized emission spectra of the most Pr BNN doped sample,measured upon 476.5 nm laser excitation.

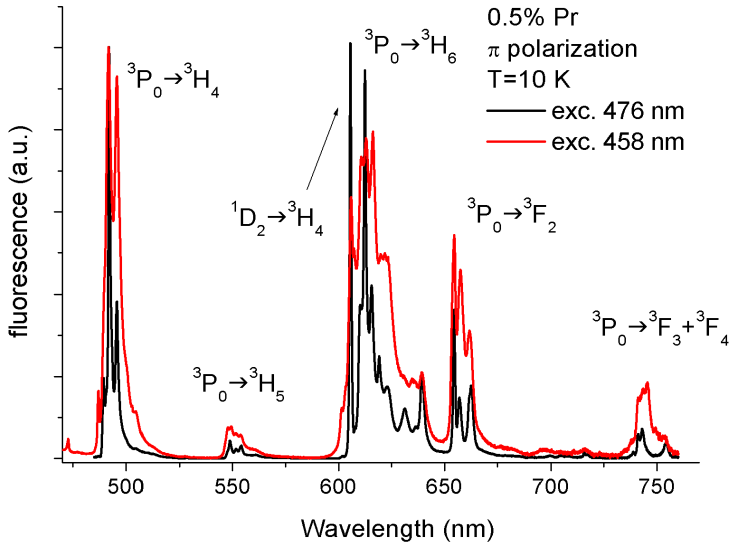

Figure 6.5. The 600-680 nm emission manifold (π polarization, E parallel c axis) measured (a) for different excitation wavelengths for the 0.5% sample

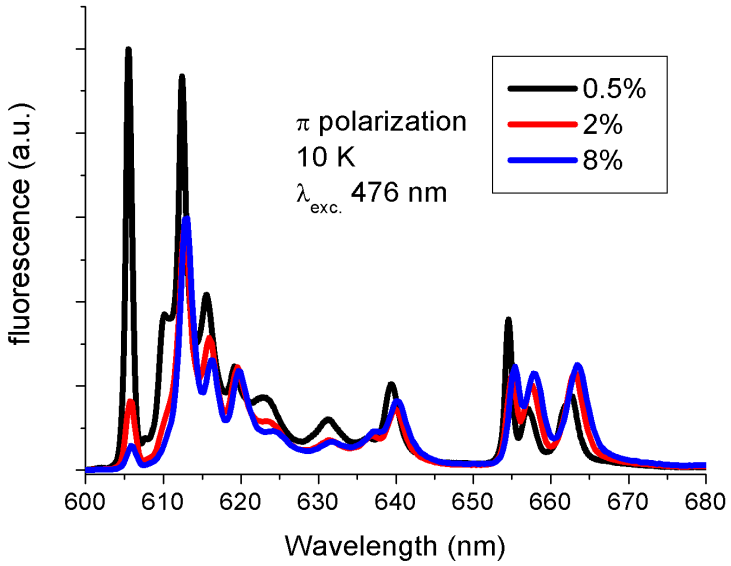

Figure 6.6. The 600-680 nm emission manifold (π polarization, E parallel c axis) measured for different Pr^{3+} concentrations.

shown in Figure 6.7).

Process 6.1 is not resonant, since the two involved transitions occur at energies differing by about 950 cm^{-1}, and process 6.2 is nearly but not fully resonant. In consequence, both are expected to be favoured by phonon assistance, since phonons of suitable energy are available in the IR or Raman spectrum [117]. This mechanism is concomitant with the $^3P_0 \rightarrow {}^1D_2$ multiphonon relaxation. The cross relaxation involving the $^1D_2$ state (Figure 6.7),

$$[^1D_2, {}^3H_4] \rightarrow [^1G_4, {}^1F_4] \tag{6.3}$$

is in practice a resonant process, so we have to expect a strong concentration and a weak temperature dependence. In addition to these processes, the mechanism involving charge transfer states has to be considered.

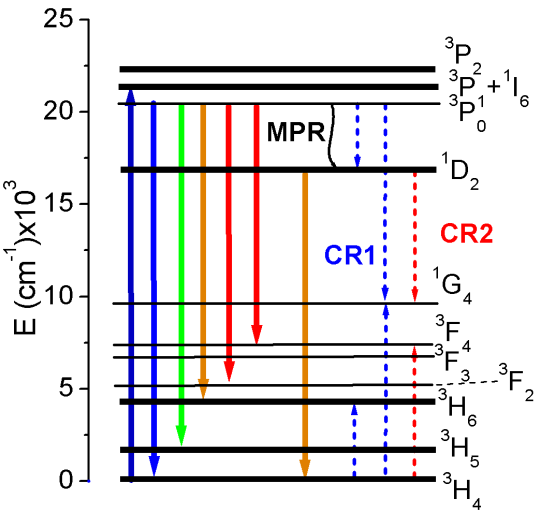

Figure 6.7. Radiative emission and Non-radiative mechanisms affecting the $^3P_0$ and $^1D_2$ emission of Pr^{3+} in oxide lattices.

6.3 298 K emission spectra

As the temperature increases the emission bands broaden and their intensity decreases. At 298 K the spectra present a broad luminescence in the 600-660 nm range, with two components: the more intense (composed by the $^1D_2 \rightarrow ^3H_4$ and $^3P_0 \rightarrow ^3H_6$ transitions) has a maximum at 605 nm that shifts to 620 nm with an increasing concentration as a consequence of the quenching of the $^1D_2$ emission, the minor one ($^3P_0 \rightarrow ^3F_2$) peaks at 655 nm (Figure 6.3). The relative intensities of the spectral components depend on the excitation wavelength: this is a typical consequence of the presence of the IVCT state (defined below) that favours the population of the $^1D_2$ state. The spectrum of the diluted crystal is rather similar to that reported for SBN: Pr (1%) [118], indicating similar environments for the optically active ions in the two lattices. The excitation spectrum (Figure 6.3) is characterized

by three band systems located in the 420-500, 340-410 and < 300 nm regions. The

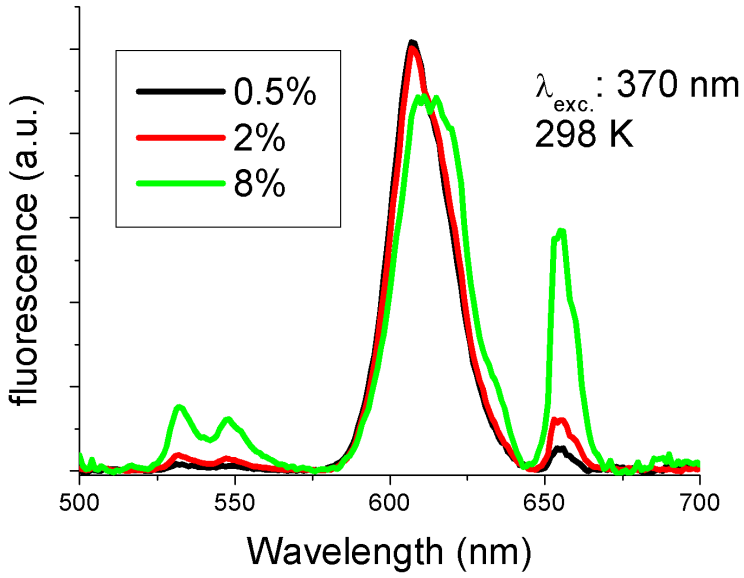

(a) Excitation at 370 nm.

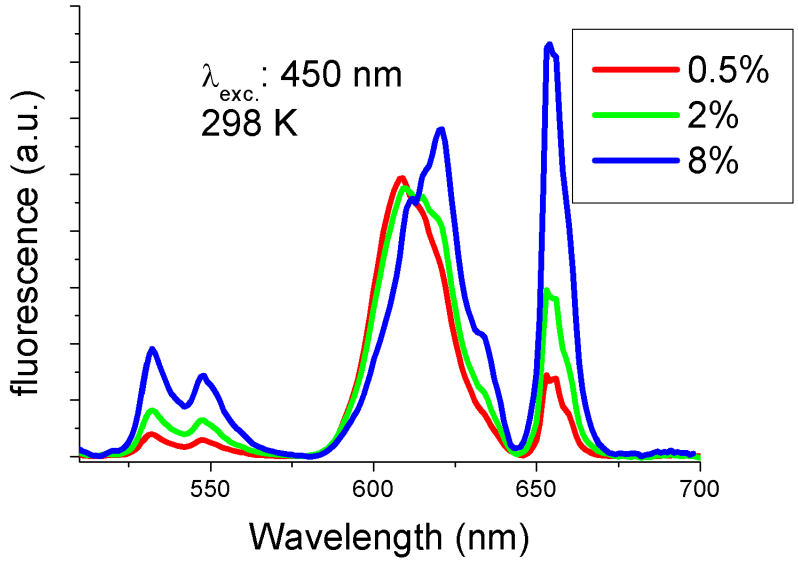

(b) Excitation at 450 nm.

Figure 6.8. Unpolarized fluorescence spectra of BNN Pr for various concentration.

last one corresponds to the host absorption band feeding the Pr^{3+} emission through an energy transfer process. The manifold in the blue region, resolved into three well separated components, is ascribed to the $^3H_4 \rightarrow ^3P_J$ (J = 0,1,2),$^1I_6$ absorption of Pr^{3+}. The band located in the 340-410 nm range is too low in energy to be assigned to a $4f^2 \rightarrow 4f^1,5d^1$ transition and it is ascribed to the intervalence charge transfer (IVCT) process $Pr^{3+}+Nb^{5+} \rightarrow Pr^{4+}+Nb^{4+}$ already observed in Pr $^{3+}$-doped niobates [119]. It is interesting to note that the IVCT maximum shifts to higher energy as the doping level increases: it is located at 374 nm in the 0.5% case, at 368 nm in the 2% and at 345 nm in the 8% case. As pointed out by Boutinaud et al [119], the position of the IVCT state is related to the optical electronegativity of the involved transition metal ion (Nb^{5+}in the present case) and to its minimum distance with respect to the lanthanide ion.

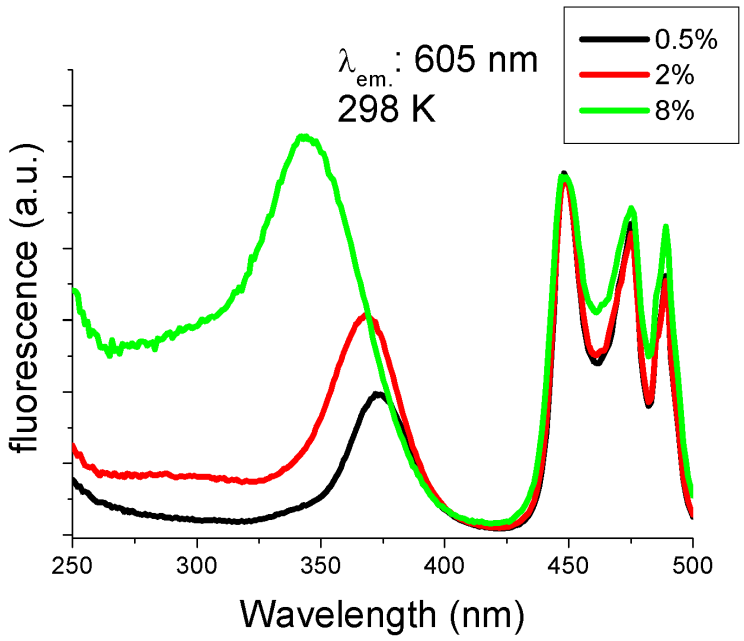

Figure 6.9. Excitation spectra at room temperature of BNN Pr at various concentration.

This dependence is formalized by the empirical equation

$$IVCT(Pr^{3+},cm-1) = 58800 - 49800\chi_{opt}(Mn^{+})d(Pr^{3+} - Mn^{+}), \qquad (6.4)$$

where $\chi_{opt}(\mathrm{Mn}^{+})$ is the optical electronegativity of the closed-shell transition metal ion Mn^{+} and $\mathrm{d}(\mathrm{Pr}^{3+}\text{-}\mathrm{Mn}^{+})$ is the shortest interatomic distance between Pr^{3+} and Mn^{+}. In the diluted crystals the shortest Pr^{3+}-Nb^{5+} distance calculated using equation 6.4 is 2.89 Å. Only in the case of C site occupancy the resulting distance, 2.90 Å, is practically coincident with the evaluated one. This confirms the average distance evaluated in the XRD analysis, and the value is quite comparable with the distance, determined for the three samples and weighted on the refined site occupancy (Table 6.3), indicating the effectiveness of the proposed model. In addition, the IVCT shift with increasing Pr^{3+} concentration indicates that the average shortest Pr^{3}+-Nb^{5+}distance increase with the doping level, confirmed by the spectral analysis.

6.4 Decay time measurements

The emission kinetics of both $^{3}\mathrm{P}_{0}$ (655 nm) and $^{1}\mathrm{D}_{2}$ (605 nm) states have been measured at different temperatures upon 455 nm excitation (Figure 6.4). The profile of the $^{3}\mathrm{P}_{0}$ emission is a single exponential only in the case of the diluted sample at 10 K. As the temperature and/or the concentration increases, the curves significantly deviate from the exponential behaviour. Possible reasons for this effect can be the following:

- As the concentration increases the distribution of the Pr^{3+} ions among the different sites tend to vary, as well as the effect of the related charge compensation mechanisms.

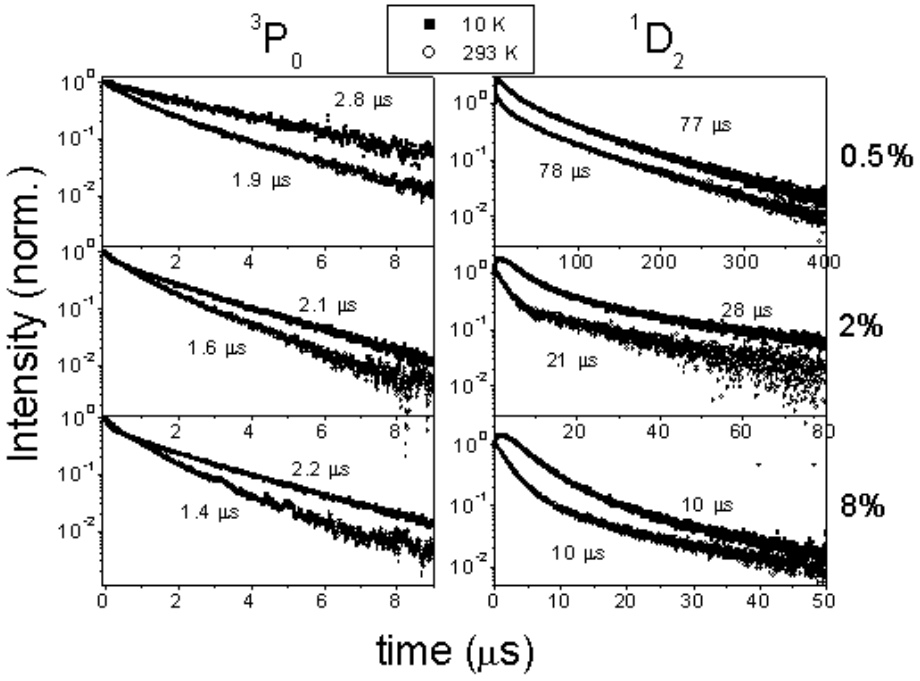

Figure 6.10. Emission decay profiles of Pr : BNN.

- The $^3P_0 \rightarrow ^1D_2$ multiphonon relaxation process requires at least four high energy (840 cm^{-1}) host phonons to occur, since the gap between the involved levels is of the order of 3300-3500 cm^{-1}. It then constitutes a temperature dependent contribution to the $^3P_0$ depopulation.
- The temperature dependent cross relaxation mechanisms.
- The de-excitation through the IVCT state can be favoured by suitable phonon assistance and then could have some temperature dependence.

It is clearly impossible to analyse the profiles on the basis of a single reliable model. We have then evaluated the effective emission decay times using [120]

$$\frac{\int tI(t)dt}{\int I(t)t} \tag{6.5}$$

where $I(t)$ represents the luminescence intensity at time t .

Table 6.4. Effective emission decay time estimated for the $^3P_0$ and $^1D_2$ manifolds at 10 K and 300 K temperature.

	$^3P_0$ lifetime (μs)		$^1D_2$ lifetime (μs)	
Temperature	10K	300K	10K	300K
0.5% Pr	1.9	2.8	77	78
2 % Pr	1.6	2.1	21	28
8 %Pr	1.4	2.2	10	10

The obtained values, shown in Table 6.4, evidence a relatively small variability, despite the number of processes potentially involved. The 10K $^1D_2$ profiles are characterized by a risetime, approximately of the order of 1 μs, confirming the feeding from the $^3P_0$ upper level through II-IV processes mentioned above. At 298 K the risetime disappears because the above-mentioned temperature dependent relaxation processes from $^3P_0$ become much more effective and the feeding process is faster. The decays are non-exponential in consequence of the presence of non-equivalent optical centres. The values of the effective decay times, calculated with equation 6.5, reveal a strong concentration dependence compatible with the resonant character of the

$$[^1D_2, ^3H_4] \rightarrow [^1G_4, ^3F_4] \tag{6.6}$$

cross relaxation responsible for the non-radiative depopulation of the $^1D_2$ level.

6.5 Conclusion

The luminescence spectra of Pr : BNN crystals are influenced by host properties and substitution mechanisms. Measurements, as a function of temperature, of the

excitation wavelength and of the doping level have evidenced the presence of non-equivalent optical centres whose emission properties are affected by different and concomitant non-radiative processes. The interaction between host and doping ions results in the formation of an IVCT state that actively contributes to the excited states dynamics of the system. In this context, the concentration shift of the IVCT band has been accounted for on the basis of a previously developed empirical model that allows the formulation of a hypothesis about the site occupancy of the Pr^{3+} ion in this host. The structures of the investigated materials have been determined by single crystal XRD measurements and are consistent with the supposed Pr $^{3+}$ occupancy, and the connection with the growth procedure has been pointed out.

Chapter 7

YPO_4 Dysprosium

In this chapter is resented the characterization of YPO_4 Dysprosium (YPO) Dy doped crystal. My contribution to this work was limited at the optical spectroscopy measurements (dynamical and steady state) and at the discussions of the results. The crystal was growth by E. Cavalli at the University of Parma, while the Judd-Ofelt analysis was performed by N. Magnani at the Institute for Transuranium Elements-Karlsruhe, in Germany. All the data at our disposal are here present in order to allow the understanding of the spectroscopic behaviour of the crystal.

7.1 Introduction

The device potentialities of Dy^{3+}-based compounds strongly depend on the relative intensity of the blue ($^4F_{9/2} \rightarrow ^6H_{15/2}$) and yellow ($^4F_{9/2} \rightarrow ^6H_{13/2}$) emission channels. The yellow-to-blue intensity ratio (Y/B) of the Dy^{3+} luminescence was ascribed by Su et al. [121] to different host related effects like covalency, site symmetry, etc, evidencing a rather complex dependence. We are exploring in detail the spectroscopic properties of a number of Dy^{3+}-doped materials in order to rationalize these

effects [122, 123, 124]. Recent papers [125, 126]have indicated it as an attractive material for the development of efficient white phosphors. Moreover, since the emission properties of YPO_4:Dy are different to those of the isostructural YVO_4:Dy [127], the intensity ratio between the blue and the yellow emission can be conveniently modulated by varying the host composition of the $YP_xV_{1-x}O_4$:Dy (with $0 \leq x \leq 1$) solid solutions [128]. This possibility remarkably extends the application range of these materials. Despite these interesting perspectives, the electronic structures and luminescence dynamics of these compounds, and of YPO_4:Dy in particular, have not yet been investigated in detail. We then measured its polarized absorption and emission spectra and the fluorescence decay profiles as a function of the temperature and of the doping concentration. From the low temperature (LT) spectra we have deduced the complete energy level scheme of the Dy^{3+} ion in this host lattice and the observed energies have been fitted to a single-ion Hamiltonian containing free-ion and crystal-field interactions. The room temperature (RT) absorption spectra have been analysed in the framework of the Judd-Ofelt (JO) theory in order to obtain information about the efficiency of the radiative transitions and, in this particular case, about the branching ratios for the luminescence from the $^4F_{9/2}$ level, that regulate the relative intensities of the visible emission bands.

7.2 10 K spectroscopy

The 10 K polarized absorption spectrum of Dy^{3+} in YPO_4 is shown in Figure 7.1. The observed multiplets, whose full widths at half-maximum (FWHM) are of the order of 15-20 cm^{-1}, correspond to the transitions from the $^6H_{15/2}$ ground state to the excited states of the $4f^9$ electronic configuration [129].

The number of the observed lines in some cases exceeds the J + 1/2 values expected from the crystal-field splitting of the $^{2S+1}L_J$ manifolds involved. This

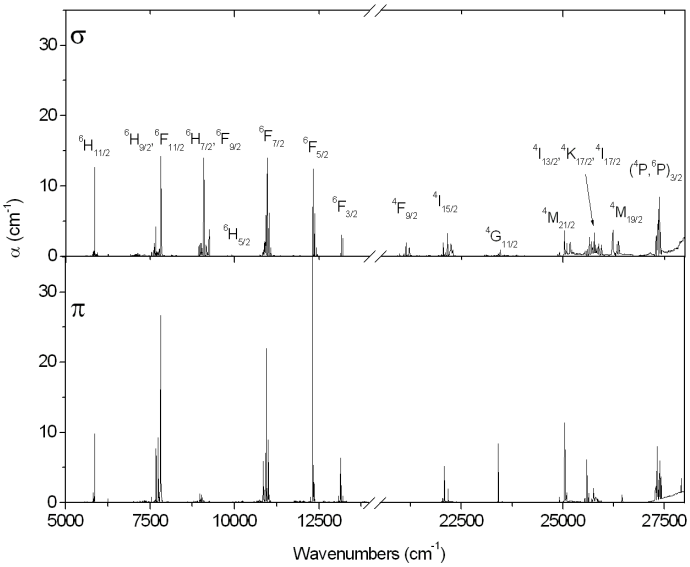

Figure 7.1. 10 K polarized absorption spectrum of YPO_4 :Dy (3%).

could be a consequence of the population, even at LT, of Stark components located just above the lowest level of the ground state or of the presence of minority centrers, constituted for instance by Dy^{3+} ions located near to lattice defects. The Stark levels of Dy^3+ are Kramers doublets and belong to the Γ_6 or Γ_7 double-group irreducible representations of the D_{2d} point group. The intensities of the optical transitions are regulated by the electric dipole selection rules:

$$\begin{array}{cc} \mathrm{E}\|c\ (\pi \text{ polarization}) & \mathrm{E}\perp c\ (\sigma \text{ polarization}) \\ \Gamma_6 \rightarrow \Gamma_7 & \Gamma_7 \rightarrow \Gamma_{6,7} \\ \Gamma_7 \rightarrow \Gamma_6 & \Gamma_7 \rightarrow \Gamma_{6,7} \end{array} \tag{7.1}$$

The structure of the ground state and of the first excited level can be obtained from the 10 K polarized visible emission spectra reported in Figure 7.2. The three

band systems centred at about 480, 575, 670 nm (inset) are assigned to the transitions from the $^4F_{9/2}$ excited level to the $^6H_{15/2}$, $^6H_13/2$ and $^6H_11/2$ levels respectively. The energy level scheme for the Dy^{3+} ion in YPO_4 deduced from the 10 K absorption and emission data is presented in Table 7.1. The observed energies have been reproduced using the following RE Hamiltonian:

$$\hat{H} = \hat{H}_{FI} + \hat{H}_{CF} \tag{7.2}$$

where, according to [130], the free-ion part is written as:

$$\begin{aligned} \hat{H}_{FI} = E_{av} + \sum F^k \hat{f}_K + \zeta \hat{H}_{SO} + \alpha L(L+1) + \beta \hat{G}(G_2) + \\ + \gamma \hat{G}(R_7) + \sum_i T^i \hat{t}_i + \sum_j M^j \hat{m}_j + \sum_k p^k \hat{p}_k \end{aligned} \tag{7.3}$$

where $k = 2, 4, 6$; $i = 2, 3, 4, 6, 7, 8$; $j = 0, 2, 4$, and the crystal-field (CF) Hamiltonian for D_{2d} point symmetry is written as

$$\begin{aligned} \hat{H}_{CF} = \sum_k \sum_q B_k^q \hat{C}_k^q = B_2^0 \hat{C}_2^0 + B_4^0 \hat{C}_4^0 + B_6^0 \hat{C}_6^0 + \\ + B_4^4 (\hat{C}_4^4 + \hat{C}_4^{-4}) + B_6^4 (\hat{C}_6^4 + \hat{C}_6^{-4}). \end{aligned} \tag{7.4}$$

This model Hamiltonian accounts for two-body electrostatic repulsion (F^k), two- and three-body configuration interactions (α,β,γ and T^i , respectively), spin-orbit coupling (ζ), spin-other-orbit interactions (M_j), electrostatically correlated spin-orbit interactions (P_k), and the crystal-field potential. A detailed description of the various free-ion operators and parameters is available in the literature [131]; the tensor operators $\hat{C}_k^q$ are defined in [132]. The CF parameters B_k^q are expressed according to the Wybourne normalization. Since $\hat{H}_{FI}$ is expected not to change significantly when the same RE ion is embedded in different hosts, the free-ion parameters for Dy^{3+}-LaF_3 [130] were tentatively used as starting values, and some of them (F^2, F^4, F^6, ζ and α) were allowed to vary during the fitting procedure.

Table 7.1. Energy levels scheme of Dy^{3+} in YPO_4.

$^{2S+1}L_J$	Exp.	Calc.	Γ_n	$^{2S+1}L_J$	Exp.	Calc.	Γ_n
	0	3	Γ_6	$^6H_{5/2}$	10040	10044	Γ_6
	-	46	Γ_6	(Γ_6+2Γ_7)	10121	10114	Γ_7
	52	52	Γ_6		10164	10160	Γ_7
$^6H_{15/2}$	112	114	Γ_7				
(4Γ_6+4Γ_7)	172	171	Γ_7		10950	10886	Γ_7
	206	202	Γ_6	$^6F_{7/2}$	11005	10925	Γ_7
	266	274	Γ_7	(2Γ_6+2Γ_7)	11057	10950	Γ_6
	308	286	Γ_7		11064	10968	Γ_6
	3462	3457	Γ_7	$^6F_{5/2}$	12254	12277	Γ_7
	3507	3501	Γ_6	(Γ_6+2Γ_7)	12312	12308	Γ_6
$^6H_{13/2}$	3507	3503	Γ_7		12321	12322	Γ_7
(3Γ_6+4Γ_7)	-	3548	Γ_7				
	-	3548	Γ_6	$^6F_{3/2}$	13094	13095	Γ_6
	3585	3598	Γ_6	(Γ_6+Γ_7)	13094	13095	Γ_7
	-	3602	Γ_7				
				$^6F_{1/2}$	13642	13632	Γ_6
	5756	5764	Γ_7	(Γ_6)			
	5813	5815	Γ_6				
$^6H_{11/2}$	5817	5821	Γ_7		20968	20957	Γ_6
(3Γ_6+3Γ_7)	-	5837	Γ_6	$^4F_{9/2}$	21070	21067	Γ_7
	5858	5859	Γ_7	(3Γ_6+2Γ_7)	21119	21100	Γ_7
	5880	5894	Γ_6		21146	21155	Γ_6
					21204	21221	Γ_6
	7490	7506	Γ_7				
	7579	7584	Γ_7		22031	22035	Γ_7
	7614	7607	Γ_6		22041	22054	Γ_7
$^6H_{9/2}$	7649	7631	Γ_7		22079	22069	Γ_6
(3Γ_6+2Γ_7)	7675	7693	Γ_6	$^4I_{15/2}$	22148	22152	Γ_7
+	7718	7726	Γ_6	(4Γ_6+4Γ_7)	22172	22168	Γ_6
$^6F_{11/2}$	-	7750	Γ_6		22232	22244	Γ_6
(3Γ_6+3Γ_7)	-	7772	Γ_7		-	22255	Γ_6
	-	7775	Γ_7		22276	22281	Γ_7
	7829	7819	Γ_6				
	-	7859	Γ_6		23359	23359	Γ_6
					23375	23372	Γ_7
$^6H_{7/2}$	-	8912	Γ_7	$^4G_{11/2}$	-	23384	Γ_6
(2Γ_6+2Γ_7)	8937	8924	Γ_7	(3Γ_6+3Γ_7)	23391	23387	Γ_7
+	9008	9000	Γ_6		23447	23436	Γ_7
$^6F_{9/2}$	9024	9024	Γ_7		-	23460	Γ_6
(3Γ_6+2Γ_7)	9044	9041	Γ_6				
	9080	9084	Γ_6				
	9153	9150	Γ_6				
	-	9153	Γ_7				
	9241	9229	Γ_7				

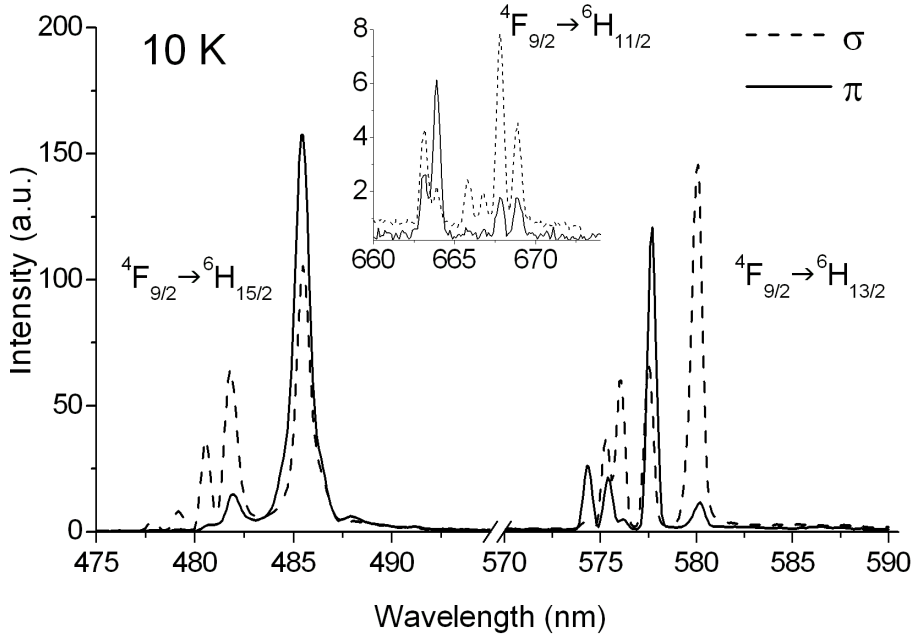

Figure 7.2. 10 K polarized emission spectrum of YPO_4:Dy (3%)

The irreducible representations reported in Table 7.1 have been determined by calculation and associated with observed features according to their polarization behaviours. The best fit of the experimental data has been carried out using the free-ion parameters reported in Table 7.2 3 and the CF parameters reported in Table 7.3. The σ (rms) for this fit is 12 cm^{-1}, of the order of the experimental FWHM.

The calculated energy levels are compared in Table 7.1 with the experimental ones. The CF parameters (B_4^4 and B_6^4 in particular) of Table 7.3 are to some extent different from those reported in a previous paper [127][7]: their final values depend in fact on the choice of the starting set, that can be made on the basis of literature data or of other evaluation criteria.

In the present case, the reliability of the CF parameters has been tested by means

Table 7.2. Free-ion parameters for Dy^{3+} in YPO_4.

Parameters	Value (cm^{-1})
$E_{av.}$	55916
F^2	91003
F^4	646566
F^6	49063
ζ	1880
α	18962
β	-633
γ	1790
T^2	329
T^3	36
T^4	127
T^6	-314
T^7	404
T^8	315
M^0	3.39
M^2	1.9
M^4	1.05
P^2	719
P^4	359
P^6	71.9

Table 7.3. CF parameters (cm^{-1}) for Dy^{3+} in YPO_4. The values determined by fitting the experimental energies are compared with those evaluated with the SPM.

	Fit	SPM
B_0^2	199 ± 12	198
$B^4 + 0$	235 ± 31	251
B_0^6	-919 ± 24	-926
B_4^4	697 ± 22	694
B_4^6	155 ± 27	-53.6

of the superposition model (SPM) analysis, based on the main assumption that the crystal-field potential at the rare-earth site can be written as the sum of axially symmetric individual contributions [133] from the ligands. In this framework, the CF parameters can be features according to their polarization behaviours.

$$B_M^n = N_M^n < r^n > \sum_l \bar{A}_n(R_l) K_n^m(\theta_l,\phi_l), \tag{7.5}$$

where K_n^m are the coordination factors defined in [134], l labels the ligands, $< r^n >$ is the average value of the n^{th} power of the radius for the RE ion considered [135], N_n^m is a suitable numerical factor [136], and we have used the usual assumption that

$$\bar{A}_n(R_l) = \bar{A}_n(R)_0 \left(\frac{R_0}{R_l}\right)^{t_n} \tag{7.6}$$

Following the procedure described in [133] we have verified that the ratios B_n^4/B_n^0 are in qualitative agreement with the experiment: in fact, for $n = 4$ we obtain a ratio of about 2.6, practically independent of t_4 (to be compared with the experimental ratio 2.96), while for n = 6 its ratio is negative for $t_6 < 11$ (a reasonable assumption since in the pure point-charge model this exponent is 7) and close to the experimental value (-0.17) for t_6 between 1 and 3. Although overparametrization prevents attempting the same analysis for B_2^0 [137], we note that the latter parameter is predicted to be positive for YPO_4:Dy for all reasonable values of t_2.

The magnitude of the $\hat{A}_n$ parameters to be chosen is in line with literature estimates for zirconates [137]. The calculated crystal-field parameters are compared to the ones resulting from the fit in Table 7.3.

7.3 Room temperature spectra and Judd-Ofelt analysis

Table 7.4. Experimental and calculated oscillator strengths (P) of Dy^{3+} in YPO_4. The Judd-Ofelt parameters, Ω_λ , the RMS and the percent error are also tabulated.

Excited state	Barycenter (cm^{-1})	P_{exp} (10^6)	P_{calc} (10^6)
$^6H_{11/2}$	5763	1.04	1.24
$^6H_{9/2}$ + $^6F_{11/2}$	7667	2.78	2.75
$^6H_{7/2}$ + $^6F_{9/2}$	8981	3.13	3.25
$^6F_{7/2}$	11090	3.33	2.83
$^6F_{5/2}$	12322	1.35	1.35
$^6F_{3/2}$	13138	0.32	0.25
$^4F_{9/2}$	20962	0.2	0.21
$^4I_{15/2}$	22094	0.34	0.47
$\Omega_2 = 0.51\ 10^{-20}$ cm^2, $\Omega_4 = 1.91\ 10^{-20}$ cm^2, $\Omega_6 = 2.87\ 10^{-20}$ cm^2			
RMS = $2.58\ 10^{-7}$; error 16.5%			

The RT polarized spectrum of the title compound is shown in Figure 7.3. In comparison with the LT spectrum, the number of components constituting the observed manifolds is increased, as well as their broadness.

Their intensities have been analysed in the framework of the Judd-Ofelt (JO) theory [138, 139]. Ten bands were considered to calculate the intensity parameters $\Omega_N (N = 2, 4, 6)$; we did not take into account the $^6F_{1/2} \leftarrow {}^6H_{15/2}$ transition because its intensity is negligible. The oscillator strengths of the transitions were determined by considering the polarization of the bands with a 2:1 ratio for $\sigma : \pi$, and the experimental data were fitted on the basis of the JO parametrization scheme after subtraction of the magnetic dipole contribution for the $^4I_{15/2} \leftarrow {}^6H_{15/2}$ transition. This contribution is small and not reported here. The reduced matrix elements were taken from Jayasankar and Rukmini [140], and the value of the refractive index was assumed to be n = 1.75 according to Zheng et al [141]. The evaluated intensity

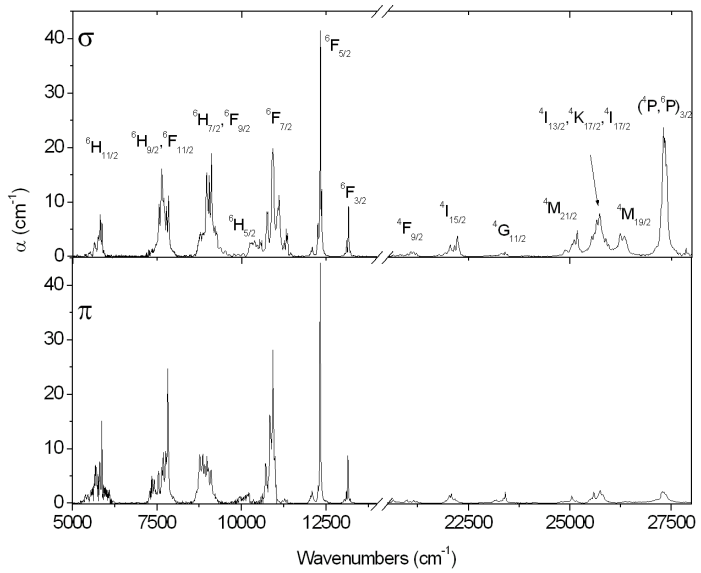

Figure 7.3. 298 K polarized absorption spectrum of YPO_4:Dy (3%).

parameters, the observed and calculated oscillator strengths, the root mean square deviation (RMS) and the per cent error are reported in Table7.4.

These parameters have been used for the calculation of the spontaneous emission probabilities and of the radiative branching ratios for the transitions from the $^4F_{9/2}$ state to the lower ones, which are reported in Table 7.5 together with the radiative lifetime of the emitting level.

In Table 7.6 these results are compared with those obtained for YVO_4:Dy [127]: it can be noted that the ratio between the branching ratio for the yellow and blue emission is much larger for the latter than for the former crystal. The Ω_2 parameter is much larger for the vanadate than the phosphate crystal, as an effect of the major intensity, in the former, of the hypersensitive $^6F_{11/2} \leftarrow ^6H_{15/2}$ absorption transition, whose reduced matrix elements are listed in Table 7.6 together with those related

Table 7.5. Calculated spontaneous emission probabilities A and radiative branching ratios β for the $^4F_{9/2}$ emitting level.

Final state	A (sec^{-1})	β
$^6F_{5/2}$	1	0.002
$^6F_{7/2}$	6	0.007
$^6H_{5/2}$	4	0.006
$^6H_{7/2}$	7	0.009
$^6F_{9/2}$	0	0
$^6F_{11/2}$	12	0.016
$^6H_{9/2}$	13	0.016
$^6H_{11/2}$	22	0.029
$^6H_{13/2}$	412	0.528
$^6H_{15/2}$	303	0.388
Radiative lifetime t = 1279 μs		

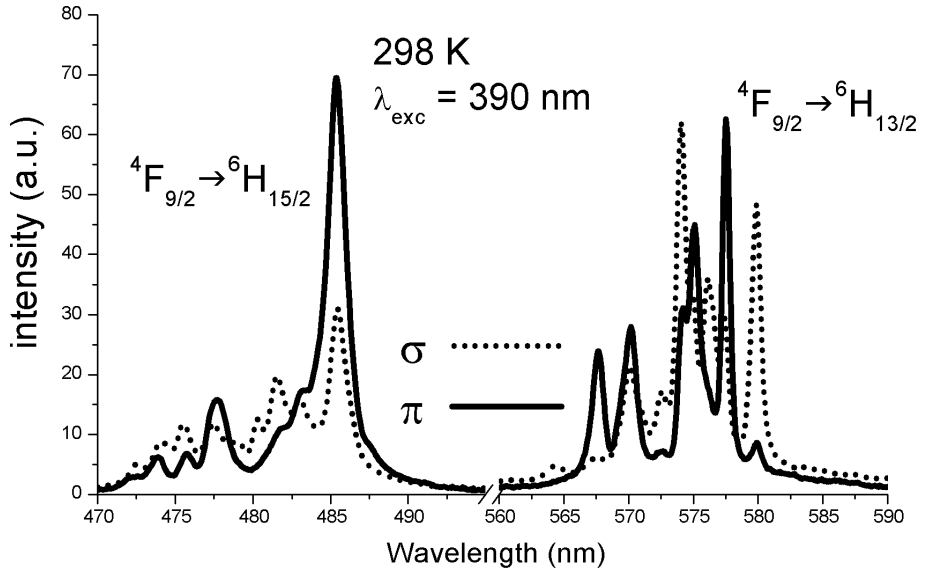

Figure 7.4. 298 K polarized absorption spectrum of YPO_4:Dy (3%).

to the blue and yellow emission transitions.

Table 7.6. (a) Comparison between the intensity parameters, the radiative lifetime of $^4F_{9/2}$ and the calculated (Y/B) ratio in the YPO_4 and YVO_4 host lattices. (b) Reduced matrix elements for some relevant absorption and emission transitions [140]

(a)	Ω_2 (10^{20} cm^2)	Ω_4 (10^{20} cm^2)	Ω_6 (10^{20} cm^2)	t(μs)	(Y/B)
YPO_4	0.51	1.91	2.87	1279	-1.36
YVO_4	6.59	3.71	1.74	440	-4.13

(b)	$\|\|U_2\|\|^2$	$\|\|U_4\|\|^2$	$\|\|U_6\|\|^2$	
$^6F_{11/2} \leftarrow {}^6H_{15/2}$	0.9349	0.831	0.2002	Absorption
$^4F_{9/2} \rightarrow {}^6H_{15/2}$	0	0.0049	0.0303	Blue emission
$^4F_{9/2} \rightarrow {}^6H_{13/2}$	0.0512	0.0172	0.0573	Yellow emission

It has to be pointed out that these are not hypersensitive transitions, as erroneously claimed in some papers [125, 126, 128]; however their intensities are strongly

affected by the Ω_2 and Ω_4 JO parameters. For large values of these parameters in fact we have to expect a relatively strong visible luminescence spectrum dominated by the yellow component, whereas with Ω_2 and Ω_4 decreasing the overall emission should concomitantly decrease with the intensity of the blue band progressively approaching, but never exceeding, that of the yellow one. The experimental trend observed in [128] (Figure 7.5) for the $Y_{0.99}Dy_{0.01}P_xV_{1-x}O_4$ ($0 \leq x \leq 1$) compositions is in reasonable agreement with this model. The 298 K polarized emission spectrum of Dy:YPO_4 in the 470-590 nm region (Figure 7.4) is composed of two band systems having comparable intensity, in agreement with the low values of Ω_2 and Ω_4.

7.4 Excited states dynamics

The decay profile of the $^4F_{9/2}$ emission has been measured as a function of the temperature and of the Dy^{3+} concentration. The 10 K curves are shown in Figure 7.5. In the case of the 0.5% doped crystal, the observed behaviour is a single exponential with decay time of 450 μs. The average distance between two active ions in this case is rather long, about 15 Å, allowing us to exclude the possibility of efficient energy transfer processes. As for a number of Dy^{3+}-doped materials [122, 124, 142], with the temperature increasing the decay time increases from 450 up to 520 μs at 298 K (see Figure 7.6). This value is significantly shorter than the radiative lifetime estimated by the JO method (1279 μs), and the difference is too important to be ascribed to non-radiative processes. Analogous behaviour has already been observed in the case of Dy:YSGG [143] and Dy:BYF [123]: in our opinion, low values of the Ω_2 intensity parameter result in the overestimation of the calculated radiative lifetime. The reason for this apparent anomaly of the JO model has not yet been clarified.

The decay curves of the 3% doped compound are not exponential, indicating the occurrence of energy transfer processes. The Inokuti-Hirayama (IH) model for the

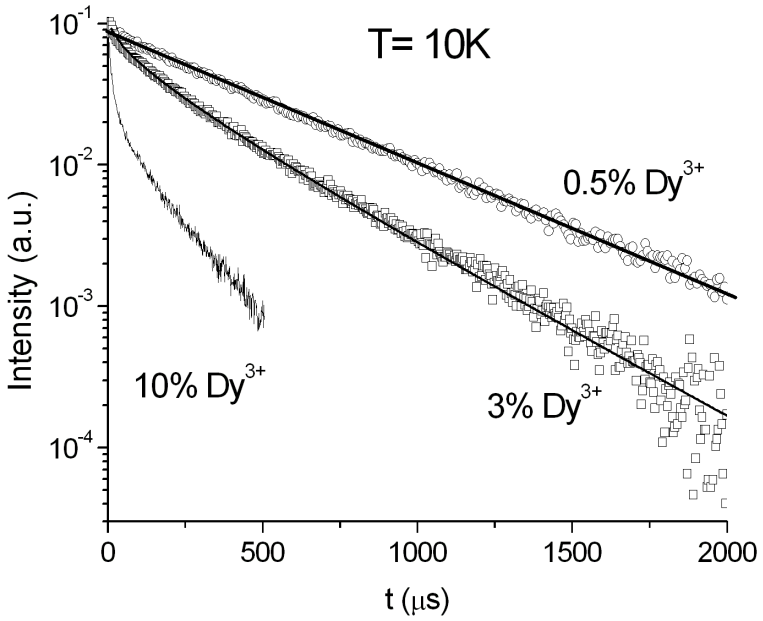

Figure 7.5. 10 K emission decay profiles of $^4F_{\frac{9}{2}}$ manifold in differently concentrated YPO_4:Dy crystals.

energy transfer in the absence of migration [144] can be reliably applied to the fit of the emission profiles:

$$I(t) = I_0 exp\left[-\frac{t}{\tau} - \alpha\left(\frac{t}{\tau}\right)^{-3/s}\right] \tag{7.7}$$

$I(t)$ is the emission intensity after pulsed excitation, I_0 is the intensity of the emission at $t = 0$,t is the lifetime of the isolated donor, a is a parameter containing the energy transfer probability and $s = 6$ for dipole-dipole (D-D), 8 for dipole-quadrupole (D-Q) and 10 for quadrupole-quadrupole (Q-Q) interaction. In the present case the best fit of the experimental data has been obtained with $s = 10$. The resulting decay time ranges from about 400 μs at 10 K to about 480 μs at 298 K, in reasonable agreement with the diluted case (see Figure 7.6). The parameter

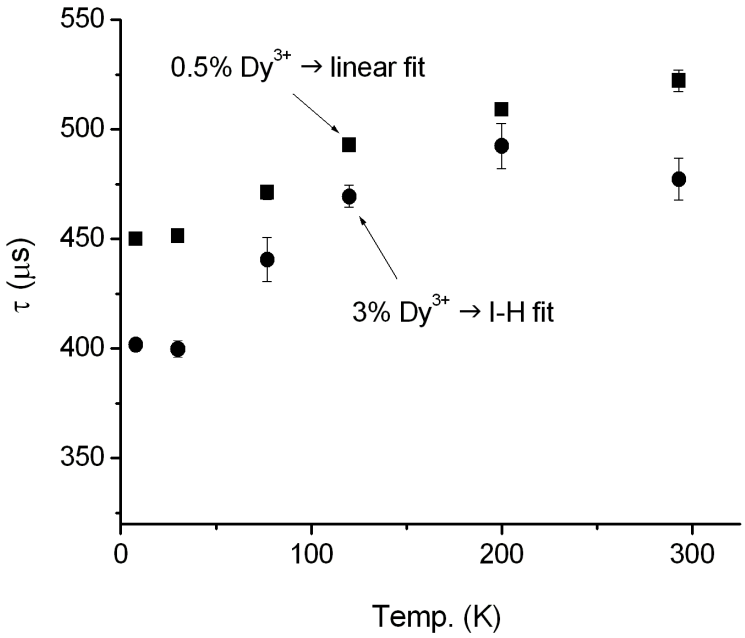

Figure 7.6. Temperature dependence of the $^4F_{\frac{9}{2}}$ manifold lifetime of the YPO_4: Dy (0.5% and 3%)

a is defined as follows:

$$\alpha = \frac{4}{3}\pi\Gamma\left(1-\frac{3}{s}\right)N_a R_0^3 \tag{7.8}$$

where Γ is the gamma function, N_a the concentration of the acceptor expressed in ions cm^{-3} and R_0 is the critical distance, that in this case ranges from 7.3 to 8 Å, in good agreement with the calculated average distance between the Dy^{3+} ions, $d_{Dy-Dy} = 8$ Å. When the Dy^{3+} concentration rises to 10% ($d_{Dy-Dy} = 5.5$ Å) the decay becomes strongly non-exponential (Figure 7.5) probably as an effect of migration processes that give rise to a significant concentration quenching. As a result, the long time tail of the profile still evidences a single-exponential behaviour, with a decay constant (of the order of 130 μs) much shorter than in the previous cases.

7.5 Results

The structure of the Stark levels of Dy^{3+} in YPO_4 has been determined on the basis of the low temperature optical spectra and reproduced by a CF calculation. The reliability of the calculated CF parameters has been confirmed by means of the SPM analysis. The host dependence of the yellow-to-blue intensity ratio (Y/B) of the Dy^{3+} luminescence has been discussed in the light of the results of the Judd-Ofelt analysis, demonstrating that the Y/B intensity ratio directly depends on the values of the Ω_2, and to a lesser extent, Ω_4 intensity parameters and that low values of these parameters imply some inconsistency between the experimental and the calculated lifetime of the $^4F_{9/2}$ state. The concentration behaviour of the decay profiles has evidenced energy transfer processes taking place for doping levels exceeding the 1% value. We are extending the investigations to other Dy^{3+}-based materials in order to test the correctness of the above conclusions and their applicability in the development of new phosphors.

Chapter 8

Tm^{3+} $LiYF_4$: spectroscopy and laser experiment.

In this chapter are reported the results of the spectroscopic measurements and laser experiments (Cw and passive Q-switching) performed on 8%at Tm^{3+} $LiYF_4$(YLF) single crystal. The analysis consisted in conventional spectroscopy around 2 μm in order to study the possibility to use this sample as active materials in that wavelength region, and in the measurements of the lifetime of $^3F_4$ metastable Tm^{3+} level. However the sample is already known as laser active media in particular for CW laser [14]. Continuous-wave (CW) powers exceeding 100 W have been already demonstrated under diode-pumping near 800 nm, with a slope efficiency of about 50% [14, 145].

Tm^{3+} is well-known as active ion for 2 μm laser system in several crystals and the laser emission have potential applications in high-field physics, military technologies, photo-medicine, optical communications and metrology. Laser action can be obtained under diode laser pumping in the $^3H_4$ manifold around 800 nm: the cross-relaxation process ($^3H_4$, $_3H_6$) $\rightarrow$ ($^3F_4$,$^3F_4$) is responsible for achieving population inversion for the $^3F_4$ $\rightarrow_3H_6$ transition, as shown in Figure 8.1. At high Tm-doping

levels, cross-relaxation between adjacent dopant ions occurs, which means that every pump photon excites two ions into the upper laser level and the quantum efficiency can be >1 [14]. The low phonon energy in fluoride crystals is an important factor contributing to the high efficiency of Tm-lasers based on these hosts [17]. The use of fluoride crystals as laser hosts is favoured because of their wide transparency window (ranging from UV up to far IR) and the low phonon energy; in particular in YLF phonon 440 cm^{-1} (structural data can be found in Chapter 3.), less than half that of typical oxides. The emission of Tm^{3+} has been studied in different hosts, and the YLF was probably the most studied fluorides.

The purpose of this study is to test the YLF as a active media for 2-micron Passive Q-switching laser (PQS). Passive Q-switching around 1.93 μm using Cr:ZnS and Cr:ZnSe SAs was first demonstrated with Tm:$KY(WO_4)_2$ and codoped Yb,Tm: $KY(WO_4)_2$ lasers [146]. The best result of 116 mW output power at a repetition rate of 20 kHz with Yb,Tm: $KY(WO_4)_2$ and Cr:ZnS corresponds to a single pulse energy of 6.7 μJ and a pulse duration of 63 ns. Note that such high repetition rates do not allow one to fully utilize the long storage time of Tm which intrinsically limits the pulse energy. PQS of Tm:$KY(WO_4)_2$ was achieved also using PbS-doped glass as a SA [147]. In this set-up, up to 44 μJ of single pulse energy was produced at a repetition rate of 2.5 kHz but for the pulse duration only an upper detection limit of 60 ns was given. Pulses as short as 8 ns were demonstrated more recently but the single pulse energy was only 30 μJ, resulting in peak powers not exceeding 4 kW [148]. Using the isostructural Tm:KLu(WO4)2 and Cr:ZnS SAs, single pulse energies as high as 145 μJ were generated at 1.92 μm with maximum average power of 0.39 W at a pulse repetition rate of 2.7 kHz and pulse durations in the 25 - 30 ns range [16]. This gives a maximum peak power of ≈6 kW. Concerning other Tm hosts, semiconductor based SAs have been used for PQS of a Tm:YAP laser in [149] achieving a maximum pulse energy of 28.1 μJ at a repetition rate of 43.7

kHz, however, the pulse duration, 447 ns, was rather long. The high pulse energy (400 μJ at 4 kHz) from a diode-pumped PQS Tm-laser, has been achieved with Tm:YAG using Cr:ZnSe as a SA [15]: However, the pulse duration in this laser was also untypically long for PQS (about 300 ns), resulting in a peak power of ≈1 kW.

While it can be concluded that the best PQS results in Tm lasers have been obtained with Cr-doped ZnS or ZnSe SAs, the use of fluoride crystals as active media is a unexplored field. Fluoride crystals exhibit longer fluorescence lifetimes and hence longer energy storage times than most other hosts [17, 18]. The use of fluoride crystals as laser hosts is favoured because of their wide transparency window (ranging from UV up to far IR) and the low phonon energy; in particular in YLF phonon 440 cm^{-1} (structural data can be found in Chapter 3.), less than half that of typical oxides. Thus, the motivation for this research was to achieve higher single pulse energy and shorter pulse durations. PQS of a diode pumped solid state laser (DPSSL) based on singly Tm-doped fluoride crystal was studied, Tm:$LiYF_4$ (Tm:YLF), and Cr:ZnS SA. Indeed, Cr:ZnS was recently employed in a co-doped (Tm,Ho):YLF laser [150] but in this case the lasing ion is Ho^{3+} at 2053 nm, and with the obtained pulse duration of 1.7 μs and pulse energy of 3.5 μJ the PQS performance of this laser was obviously rather poor.

The the spectroscopic measurements reported in this chapter have been performed at the University of Pisa, while the 2 mum laser action, both in CW that in passive Q-switching mode, has been performed a the Max Born Institute in Berlin.

8.1 Absorption

The first optical measurement performed on the samples consisted in the acquisition of the absorption spectra. These data can be helpful when it is necessary to verify the absence of impurities inside the crystal, that seriously compromise the optical

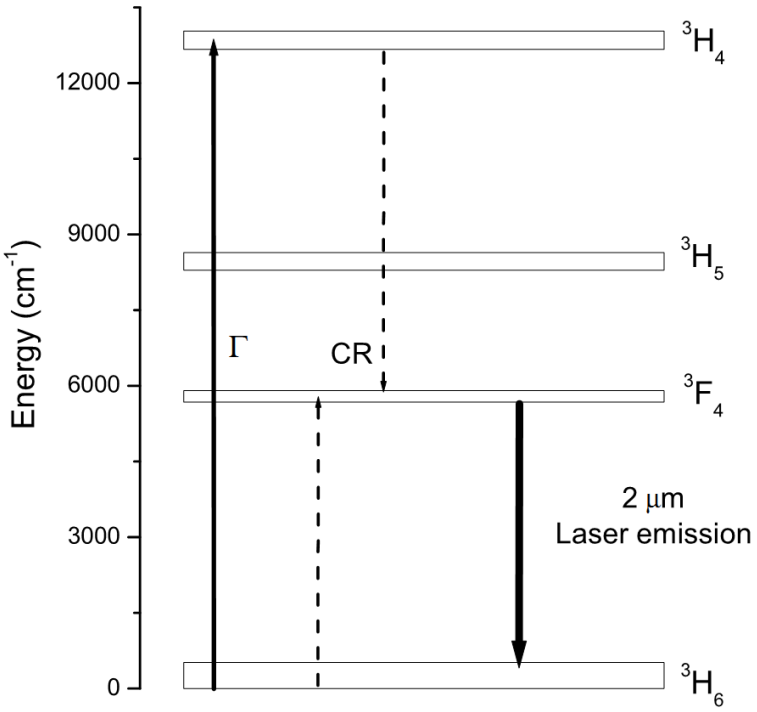

Figure 8.1. Energy level diagram of Tm^{3+} in the region of interest. Γ indicates the pump at $\sim$ 800 nm, CR stand for the cross relaxation process ($^3H_4$,$^3H_6$) $\rightarrow$ ($^3F_4$,$^3F_4$) and the laser emission $^3F_4 \rightarrow ^3H_6$ around 2 μm.

performances. We checked that the absorption unpolarized spectrum of the crystal in the interval between the 200 nm to 2000 nm, that show no evidence of incorporation of optically active impurities, within the sensitivity of the spectrophotometer, as a hint of the high purity and quality of the crystals.

Form the assorbance given by the CARY 500 defined as:

$$A(\lambda) = \log_{10} \frac{I_0}{I_1} \tag{8.1}$$

where I_0 is the reference beam signal and I_1 the signal measured after the is possible

to calculate the absorption sigma (σ_{abs})

$$\sigma_{abs} = \frac{A(\lambda) \times log_{10}(e)}{N \times d} = \frac{\alpha(\lambda)}{N}. \tag{8.2}$$

where d is the thickness of the sample, $\alpha(\lambda)$ the absorption coefficient and N is the concentration of the doping ions/cm^3, that for our sample is $1.1{\times}10^{21}$ ions/cm^3.

Particular interest has to be devoted to the $^3H_4$ spectrum because it is suitable for diode-pumping: it presents the main peak position at 780.1 nm. Of particular interest is the absorption at 802 nm, that is the wavelength of the excitation source of the laser, showing an absorption coefficient $\alpha = 1.72$ cm^{-1} in π polarization or an equivalent σ_{abs} of 1.5×10^{-21} cm^2(see Figure 8.2).

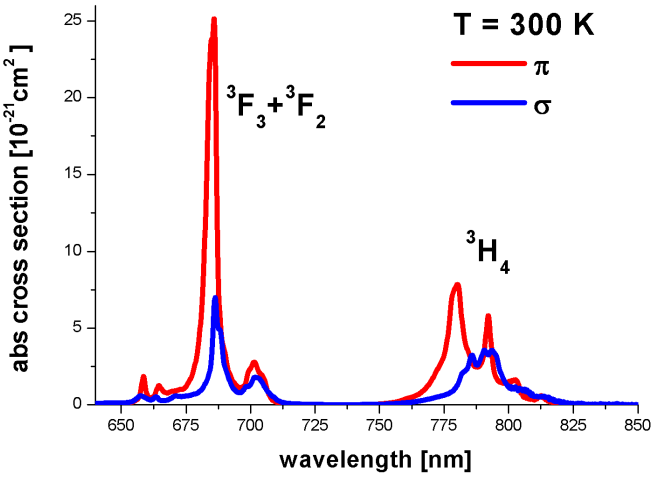

Figure 8.2. Absorption sigma in π and σ polarization of the ground state absorption of the ($^3F_2$+$^3F_3$) and $^3H_4$ manifolds.

The absorption band with the longest wavelength is the one of the $^3F_4$ manifold (Figure 8.3) from which the 2 μm laser emission starts: absorption extends up to 1900 nm. Instead of the absorption coefficient the absorption sigma is presented.

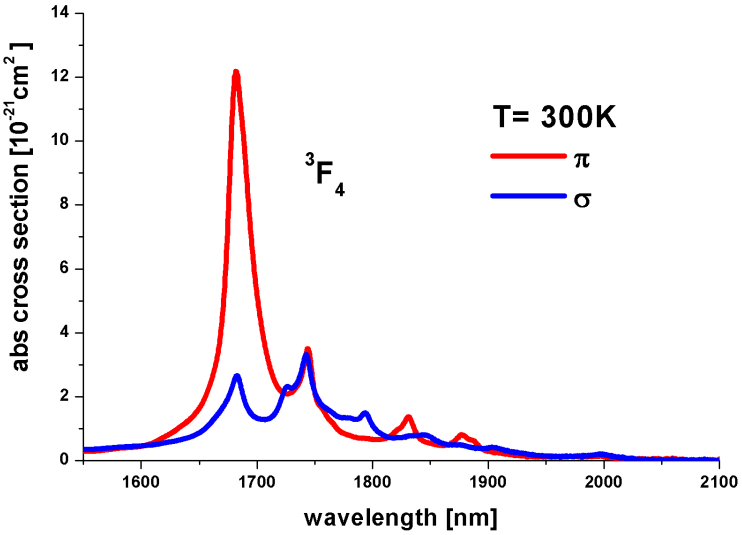

Figure 8.3. Absorption sigma in π and σ polarization of the ground state absorption of the $^3F_4$ level.

8.2 Fluorescence measurements.

The room temperature lifetime was acquired using the set-up presented in 3.5, using a Ti:Al_2O_3 pulsed laser, tuned to the maximum ground state absorption wavelength of the $^3H_4$ manifold (≈791 nm) and observing the transition $^3F_4 \rightarrow ^3H_6$ at 1932 nm. In Figure 8.4 is possible to see one of the acquired decay, that shows a single exponential decay. The experimental data were fitted by a single exponential model, and the parameters found were statistically acceptable. The resulting radiative lifetime was estimated to be 14.0±0.7 ms, that is in agreement with value found in literature [17, 18].

The static emission fluorescence was acquired using a similar set-up presented in section 3.5, using a AlGaAs laser diode tuned at an emission of 802 nm. The data collected is needed to calculate the emission sigma. The emission cross section σ_{ems}

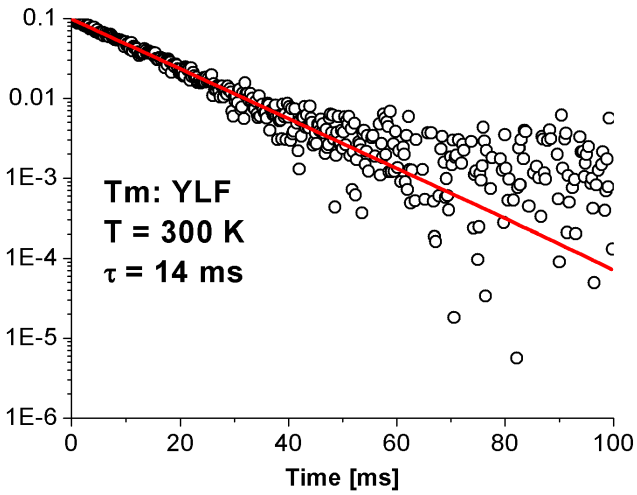

Figure 8.4. Decay of the $^3F_4 \rightarrow ^3H_6$ transition in Tm YLF, by exciting at 780 nm and observing at 1832 nm.

was estimated using the $\beta - \tau$ integral method [151], using the following formula:

$$\sigma_{ems}(\lambda) = \frac{\lambda^5}{\tau \frac{1}{3} \sum_s \left(\int \lambda I_s(\lambda) d\lambda \right) 8\pi n^2 c} I_p(\lambda), \tag{8.3}$$

where τ is the radiative lifetime, n is the refractive index of the lattice, $I_p(\lambda)$ is the fluorescence intensity in p-polarization.

The same quantity could be calculated using the reciprocity method, that relates the σ_{abs} with the emission σ_{ems}, using the formula:

$$\sigma_{ems}(\nu) = \sigma_{abs}(\nu) \frac{Z_l}{Z_u} exp\left(\frac{E_{ZL} - h\nu}{kT} \right). \tag{8.4}$$

where Z_l and Z_u are the partition function of the lower and upper manifold respectively, in our case the $^3H_6$ and $^3F_4$, and the E_{ZL} is the energy of the zero phonon line. The ratio Z_l/Z_u used was 1.51 and the wavelength of the zero phonon λ_{ZL} line is 1784.7, both the value are taken from Payne *et al.* [18, 152]. A clarification of the

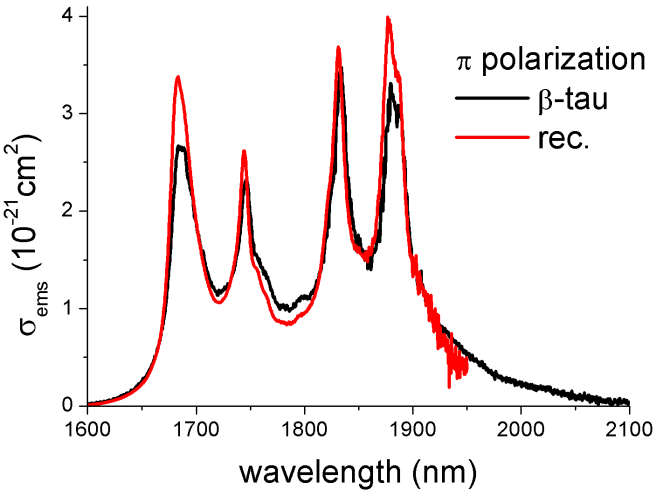

Figure 8.5. Comparison of the σ_{ems} of $^3F_4 \rightarrow ^3H_6$ transition in π polarization calculated with the $\beta - \tau$ and reciprocity method.

different method used to calculate the emission sigma is reported in appendix B. In Figure 8.2 a comparison of the results achieved with the two different method

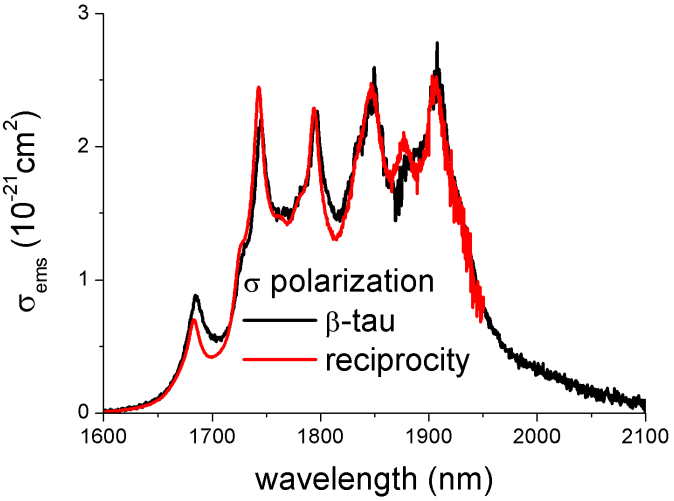

Figure 8.6. Comparison of the σ_{ems} of $^3F_4 \rightarrow ^3H_6$ transition in σ polarization calculated with the $\beta - \tau$ and reciprocity method.

are presented, the reciprocity calculation is reported only until 1950 nm, indeed at longer value the amplification of the σ_{abs} due to exponential in the equation 8.4 amplifies the background absorption. The reciprocity method shows a maximum of 4.0 $\times 10^{-21}$cm^{-1} at 1877 nm in π polarization, while the $\beta - \tau$ shows a maximum of of 3.5 $\times 10^{-21}$cm^{-1} at 1834 nm. The reciprocity seems to give an overestimated value of the σ in the whole spectra, normally it was expected that the estimation of reciprocity is higher than the $\beta - \tau$ at wavelength shorter than λ_{ZL}, where the fluorescence is lowered from the reabsorption process. At higher wavelength, on the other hand it is expected a that the $\beta - \tau$ gives an higher estimation that the other method. The behaviour explained before between the two calculation of the emission sigma is respected for the σ polarization, where reciprocity gives a higher results at wavelength shorter than λ_{ZL} and the $\beta - \tau$ for the longer(see Figure 8.2). The results is comparable with the data reported for YLF in [18] by Payne *et al.*, where the σ_{ems} was estimated using the reciprocity method, and reports a maximum a results of 3.7 $\times 10^{-21}$cm^{-1} at 1880 nm in [18, 14].

Using the polarized absorption cross sections σ_{abs} at room temperature for the present doping level and the emission cross sections σ_{ems} derived as described before using the $\beta - \tau$ integral method is possible to calculate the gain cross section gain σ_{gain}, defined by the following formula [153, 154]:

$$\sigma_{gain} = \beta \times \sigma_{ems} - (1 - \beta) \times \sigma_{abs} \tag{8.5}$$

where β represents the inversion rate.

In Figure 8.7 the polarized gain coefficient Nσ_{gain} in presented for two different inversion rate value (β = 0.2,0.3). This figure is very useful for understanding the laser behaviour and the polarization of the laser output that are presented in the next section. It is possible to seen that at lower inversion rate ($\beta = 0.2$)σ-polarization exhibits higher gain coefficient with a maximum centred around 1910 nm. At higher

inversion rates($\beta = 0.3$), however, strong π-polarized gain band emerges at shorter wavelengths, with a broader maximum centred around 1885 nm.

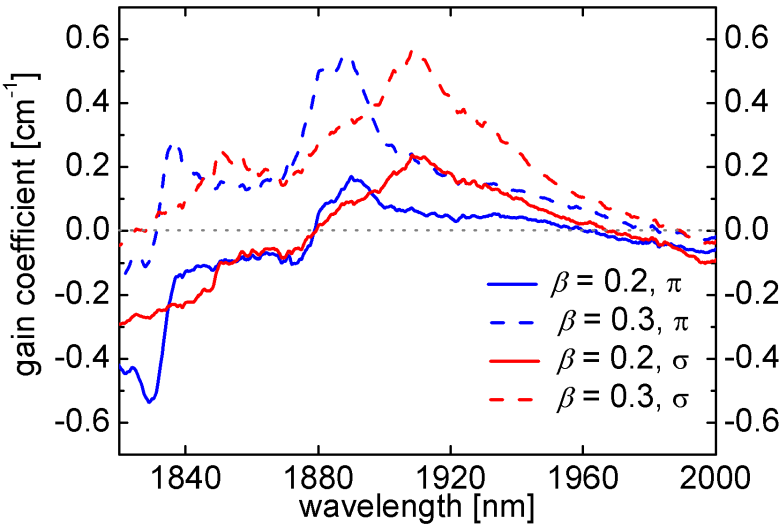

Figure 8.7. Tm:YLF polarized gain coefficient N σ_{gain} (N=1.1×10^{21} ions/cm^3 is the doping density) for two values of the inversion parameter β.

8.3 Cw and passive Q-switched laser experiment.

The laser operation was performed using an L-shape emifocal cavity as reported in Figure 8.8. The pump was delivered through the plane mirror (M1), antireflection (AR) coated for the pump wavelength and high reflection (HR) coated for the laser wavelength. As output coupler (M3) we used a Ho-laser mirror with radius of curvature R_{oc} = -100 mm whose secondary reflection band at shorter wavelengths had a maximum near 1930 nm where the transmission was 32%. The 45^o-bending mirror (M2) was plane, HR-coated for the laser and AR-coated for the pump radiation. The dichroic bending mirror was essential to avoid damage to the SA caused by the pump but at the optimum SA position the pump power still had to be limited

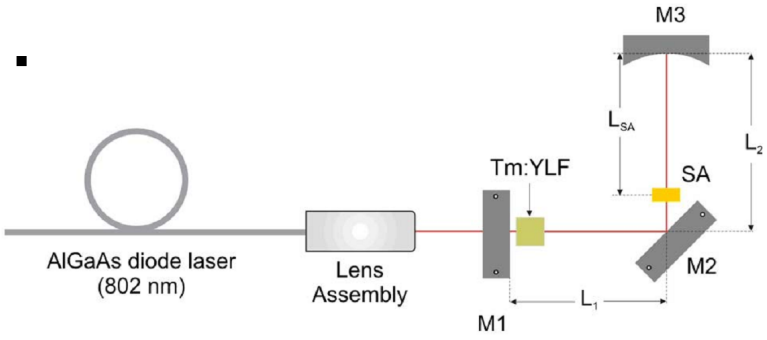

Figure 8.8. Setup of the PQS Tm:YLF laser. SA: Cr:ZnS saturable absorber, M1: dichroic pump mirror, M2: HR-laser, HT-pump mirror, M3: output coupler.

to values lower than in the CW regime to avoid damage due to the high intracavity fluence. The pump source was a fibre-coupled (NA = 0.22, 200 μm core diameter) AlGaAs diode laser delivering up to 10 W at 802 nm. The active element was an a-cut 8 at.% Tm:YLF crystal with dimensions 3 x 3 x 3 mm^3. The uncoated sample was mounted in a Cu holder with circulating water at 17°C. The incident pump beam was focused to a 200 μm spot diameter on the crystal with a lens assembly of 20 mm focal length. The polycrystalline Cr:ZnS SA samples (IPG Photonics) were specified with low signal transmission (corrected for Fresnel reflections) of T_0 = 78, 85 and 92% at 1910 nm. Their AR-coating reduced the reflection to 1% per surface. The SAs were 2.2 mm thick, with aperture of 4.5 x 9.3 mm^2.

Best operation in continuous-wave (CW) mode was achieved for a physical cavity length of 99 mm (L_1 =33 mm, L_2=66 mm). The slope efficiency with respect to the incident pump power was 11% and the threshold was 2.3 W (Figure 8.9). For the relatively low absorption of the crystal for unpolarized light at 802 nm (38%), the slope efficiency calculated relative to the absorbed power is 29%. The laser efficiency is very poor if compared with other CW Tm:YLIF laser, that normally exhibits a slope efficiency of about 50% [14, 145] but we have to bare in mind

that the cavity is not optimized for CW operation, in fact the out-coupler was choosen with high trasmittivity, for a laser cavity obviously, that is ≈ 35% at the laser wavelength. The laser wavelength was 1909 nm and the laser radiation was σ-polarized (perpendicular to the crystal c-axis). That is in agreement with the emission gain section,that exhibits a maximum at 1909 nm in σ polarization.

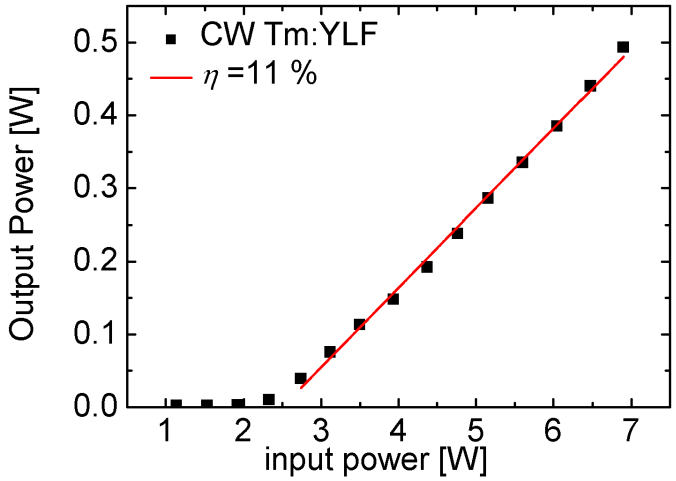

Figure 8.9. CW laser performance of the Tm:YLF laser.

The passive Q-switching (PQS) laser action was achieved posing the saturable absorber (SA) as close as possible to the bending mirror (the distance to the output coupler was ≈60 mm) which gave the shortest pulses. In the case of PQS the cavity length was reduced to 98 mm (L_2=65 mm) for optimum operation.

For the SA with T_0=92% the threshold increased to ≈ 3 W. The repetition rate was 61 Hz near threshold, increasing with the pump power to 254 Hz (Figure 8.10). The average power was also increasing, basically due to the repetition rate because the pulse energy remained almost constant, between 400 and 450 μJ. The maximum average power reached 111 mW.

Best results were achieved with the T_0 =85% SA. The pulse energy was higher

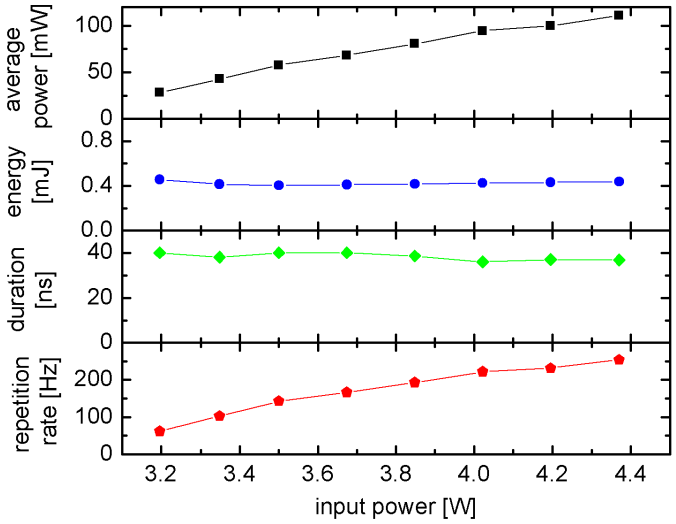

Figure 8.10. PQS characteristics of the Tm:YLF laser using Cr:ZnS SA with T_0=92%.

and almost independent of the repetition rate, around 850 μJ. The repetition rate increased from 39 to 120 Hz with the pump power (Figure 8.11). The maximum average power was 98 mW. The pulse duration remained again almost constant with pump power, around 14 ns, shorter than for the T_0 =92% SA. Lasing with the T_0=78% SA was very inefficient.

In PQS regime, using the T_0 =92% SA the emission showed a peak at 1902 nm, shifted to shorter wavelengths as compared to the CW regime, but remained σ-polarized, see Figure 8.12. With the T_0 =85% and 78% SAs the wavelength shifted to yet shorter values, 1886-1887 nm, and the polarization was π . While the wavelength shift is typical for the behaviour of a three-level laser system with increasing losses (increasing inversion rate), the polarization switching is in accordance with the individual peaks observed in the polarized emission spectra of Tm:YLF. Looking at the gain sigma Figure 8.7, is possible to see that at lower inversion rate the σ-polarization as an higher gain coefficient, with a maximum at 1910, the laser emission wavelength in CW regime. The increasing of the inversion rate due to

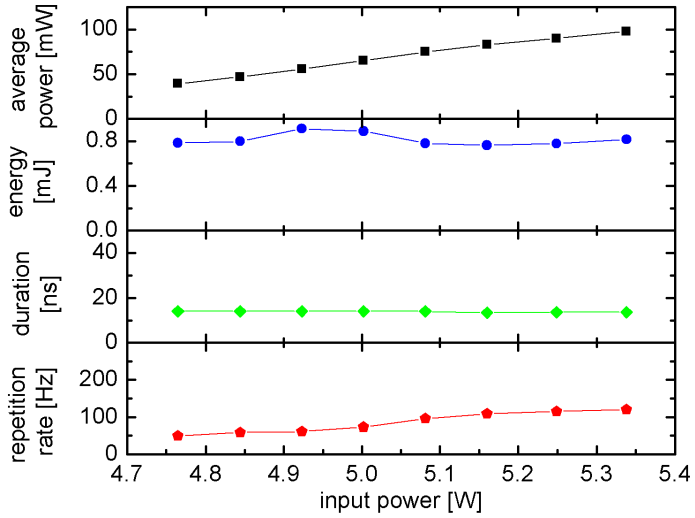

Figure 8.11. PQS characteristics of the Tm:YLF laser using Cr:ZnS SA with T_0=85% low signal transmission.

SA's losses shows an increase of π-polarization gain that it is reflected in the lasers output polarization. In fact with the T_0=92% SA the polarization is a mixing of two polarization, and finally with T_0=85% SA is π-polarized emission at 1886 nm, around the maximum of the π-gain sigma with $\beta = 0.3$

8.4 Conclusion

A Tm YLif was characterized by spectroscopic measurements, showing absorption sigma and emission sigma and lifetime comparable with the literature. For the first time it was demonstrated a Passive Q-switched of a diode-pumped Tm-doped fluoride laser using polycrystalline Cr:ZnS SA in the cavity of Tm:YLF. The energy pulse in the best case is $\approx$ 900μJ with a pulse duration of 14 ns, corresponding to $\approx$ 65 kW of peak power, this results improves of peak power of about an order of magnitude compared with [16]. The peak power ($\approx$ 65 kW) exceeded the best values obtained previously with flash lamp-pumped systems (3.2 mJ and 90 ns)

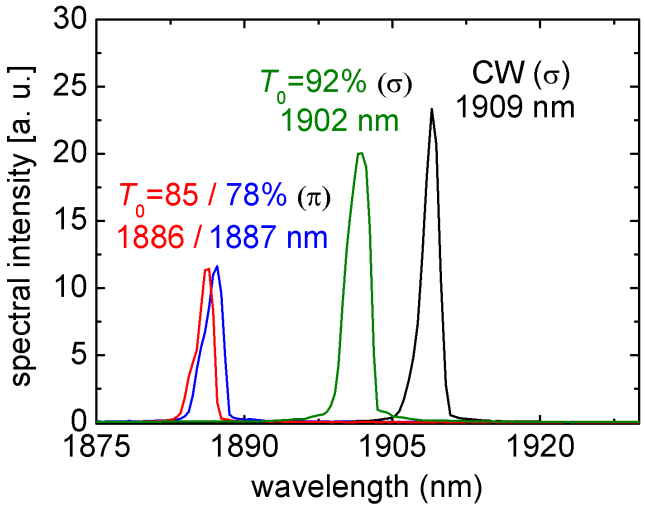

Figure 8.12. Tm:YLF laser spectra in CW and PQS regimes using different Cr:ZnS SAs. The transmission of the output coupler at the actual laser wavelength is ≈35% (CW), ≈40% (T0=92%) and ≈50% (T0=85/75%).

using Tm:YAG and Cr:ZnSe SA [155]. Also, the results double the highest, at the time of the results, the pulse energy (≈400 μJ at 4 kHz) from a diode-pumped PQS Tm-laser achieved with Tm:YAG using Cr^{2+}(Cr):ZnSe as a saturable absorber (SA) [15].

After this result other fluorides crystals, in particular $LiLuF_4$, was tested in similar laser setup, increasing the the pulse energy even more (≈1.2 mJ) with a shorter pulse duration (7.2 ns) and consequently an higher energy peak of about 166 kW [156]. Both the works demonstrate that fluoride crystals are promising Tm-hosts for achieving highest pulse energies in PQS under CW diode-pumping, and opens a new interesting field of research for 2-micron CW diode pump PQS laser.

Conclusion and Future Development

In this thesis I characterised eleven sample of Pr-doped fluoride. In order to evaluate the best pump wavelength to excite the crystals, the absorption spectra was performed at the beginning. From these measurements the best pump wavelength, where the absorption coefficient is highest, is around 444 nm, that fits the GaN laser diode. The emission is characterized by the CIE 1931 colour coordinates theory. To separate the dependence of the results from the pump light, the incident blue radiation was not taken into account during this calculation. The correlated colour temperature for each sample was calculated by their chromatic coordinates. Both looking at the CIE coordinates and the calculated CCT, each sample, in good approximation, emits in the white region.

In order to verify the possibility of obtaining an efficient white light source, the intrinsic efficiencies of the samples were measured. Since the intrinsic efficiency represents the maximum efficiency obtainable for a device based on the presented samples, and similarly for the CIE coordinates, the obtained values were used to discriminate between good and bad candidates for lighting applications. Looking at the CIE chromatic coordinates and at the intrinsic efficiency the best candidate for lighting application is the 1.25% Pr^{3+}:BaY_2F_8 with an intrinsic efficiency equal

to 55%. This value of intrinsic efficiency is comparable, within experimental uncertainties, to the 1.25% Pr^{3+}:$LiLuF_4$ sample but its chromatic coordinated are closer to the white point.

From the data collected we identified in the 1%at the best concentration of Pr-ions. Future work will be devoted to the growth and study of a 1%at Pr^{3+}:KY_3F_{10}, since this crystal is well promising. In fact the 0.3%at Pr^{3+}:KY_3F_{10}, already presented a very good efficiency of about 55%.

An other future development will be the insertion of powders of the crystals here studied in a unique host material like glass or an other crystalline medium. In this way, it will be possible to obtain a more broad spectrum closer to the black body radiation. The first step is the realization of nano or sub-micron particle of the crystals investigated, and eventually check the difference in the emission and efficiency between powders and bulk crystals. The colour in the powder mixture could be controlled with the mixing of different lattices and concentrations, this solution is in fact more simple than growing a sample with an optimized concentration, due to the long time needed to perform a growth with the Czochralski method, and also it will allow us to mixing different Rare Earth elements minimizing the problems due to the cooperative mechanism between the ions, that decrease the conversion efficiency of the materials. To date, some milling experiments are performed in our laboratory, some preliminary works on characterization particles dimension is now work in progress.

Regarding the emission of coherent light in the "eye-safe" 1.9 μm, the results achieved with the PQS Tm:YLiF laser are very promising in term of pulse energy ($\approx$900 μJ),and pulse duration (14 ns) . Furthermore the results achieved are confirmed and improved by the Tm:LiLuF PQS laser system. The fluorides crystals are so very promising and a future development could be the characterization of other fluorides single crystals, such as BaY_2F_8 that has been already tested in CW

regimes.

Appendix A

Principal methods for the Correlated Colour Temperature determination

Correlated Colour Temperature of a light source with colour coordinates (x_1; y_1) is the temperature of the Planckian radiator whose chromaticity is nearest to (x_1; y_1). The first methods proposed to estimate the CCT are based on graphical interpolation. Using the calculated (x; y) (or$u$, v) coordinates and the chart developed by Kelly [157], the CCT was found by interpolation between two isotemperature lines closely ranking the target chromaticity. The Kelly's graphic interpolation was substituted by the algorithm proposed by Robertson in 1968 [158]. This method is based directly on the graphical method, and involves interpolation between two adjacent members of a set of n isotemperature lines, defined by their correlated temperature (T_i) and their slope in the diagram (m_i). In order to find the two adjacent lines between the test chromaticity (u_T ;v_T), the distance (d_i) of the test point from

each line is calculated:

$$d_i = \frac{[(v_T - v_i) - m_i(u_T - u_i)]}{(1 + m_i^2)^{1/2}} \tag{A.1}$$

The point lies between the only two adjacent lines for which $d_j = d_j + 1$ is negative. The T_c is determined in Robinson's algorithm like:

$$Tc = \left[\frac{1}{T_c} + \frac{\theta_1}{\theta_1 + \theta_2}\left(\frac{1}{T_{j+1}} - \frac{1}{T_j}\right)\right]^{-1} \tag{A.2}$$

where $\theta_{1;2}$ are the angles between the two isotemperature lines and the line joining $(u_T\ ;v_T\ )$ to their intersection (Figure A.1). Since $\theta_{1;2}$ are small, eq. refTC can be written as:

$$T_c = \left[\frac{1}{T_c} + \frac{d_j}{d_1 - d_{j+1}}\left(\frac{1}{T_{j+1}} - \frac{1}{T_j}\right)\right]^{-1} \tag{A.3}$$

For this method a very important role was assumed by the isotemperature lines set chosen. The more narrow they are, the less is the introduced error.

With the development of new and more powerful computers other new numerical methods have been developed for calculating CCT. Many other approximation to calculate the CCT were proposed by Schanda et al. [159], by Krystek [160] and by Xingzhong [161]. The last author developed an empirical equation to calculate CCT from the 1960 chromaticities $(u;v)$ in the range of 1666-25000 K obtaining errors comparable with Robertson's. More recently McCamy proposed a third order polynomial equation for computing CCT from CIE 1931 x,y. To develop his method he used the fact that the isotemperature lines for CCTs of interest converge toward a point (*epicentre point*) in the chromaticity diagram adding that his function depends on the reciprocal of the slope of the isotemperature line from that point to two chromaticities of the light. Since for a broad CCT range there is not only one convergence point so he used the intersection between 16 isotemperature

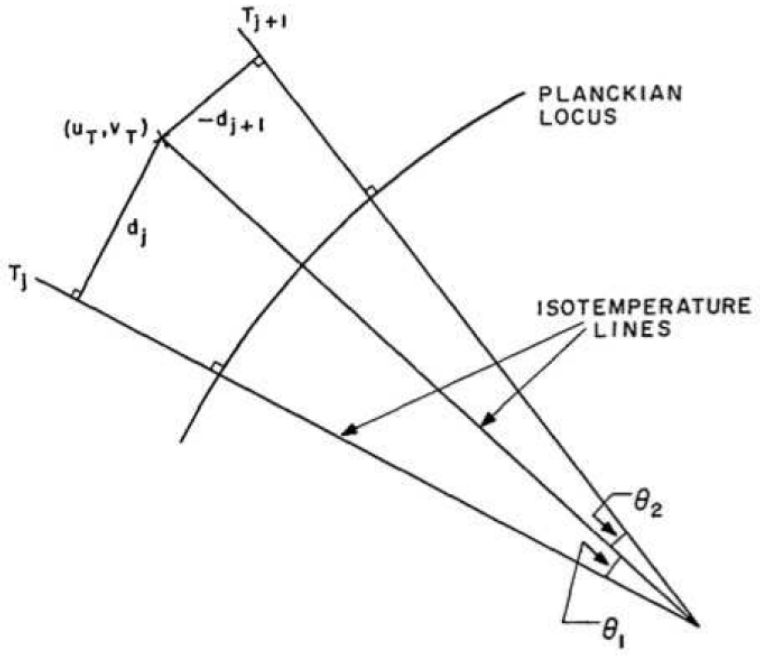

Figure A.1. Method of interpolation to find correlated colour temperature [158].

lines (between 2222 K and 12500 K). The McCamy polynomial formula is:

$$CCT = -449n3 + 3525n^2 - 6823.3n + 5520.33 \tag{A.4}$$

with n, the inverse line slope, is equal to:

$$n = \frac{x - x_e}{y - y_e} \tag{A.5}$$

where $x_e = 0.3320$ and $y_e = 0.1858$ are the epicentre coordinates. The maximum absolute error for colour temperatures ranging from 2856 (illuminant A) to 6504 (D65) is below 2 K.

In 1999 in order to extend the useful range, Javier Hernàndez-Adrès, Raymond

L.Lee and Javier Romero [88] , based on the McCamy [86, 87] approximation developed a new algorithm to calculate the CCT using the same n McCamy parameter:

$$CCT = A_0 + A_1 exp(-n/t_1) + A_2 exp(-n/t_2) + A_3 exp(-n/t_3) \qquad \text{(A.6)}$$

They began like McCamy [86, 87] by using only one colorimetric epicentre but up to 70000 K. Their error become as large as 53% above 10^5 K. Then they proposed, as Xingzhong [161] did, to add a second epicentre. Changing epicentres means changing the constants A_i and t_i in eq. A.6 The constants values are reported in Table A. The maximum relative error of eq A.6 is $<$ 1:74% for a CCT of 4792 K. However it is important to note that, as Krystek did, these errors are not too significant given that uncertainties in measuring chromaticities are normally around 5%. The last two methods are the most used in the last years. Today there is not an official and standard method to calculate the CCT. In this thesis the McCamy [86, 87] and the Hernàndez-Adrès et al. [88] approximations are taken into account.

Table A.1. Epicentre coordinates and constants for eq. A.6

Constants	Valid CCT range (K) 3000-50000	Valid CCT range (K) 50000-8×10^5
x_e	0.3366	0.3356
y_e 0.1735	0.1691	
A_0	-949.86315	36284.48953
A_1	6253.80338	0.00228
t_1	0.92159	0.7861
A_2	28.70599	5.4535×10^{-36}
t_2	0.20039	0.01543
A_3	0.00004	
t_3	0.07125	

Appendix B

Emission cross section

This appendix will be dedicated to show the details of the two most used methods that is usually used to calculate the stimulated emission cross-section: the reciprocity method and the so-called $\beta - \tau$ method developed by Aull and Jenssen [151]. Note that in this thesis only the $\beta - \tau$ method was used but in order to compare literature results is important to have in mind how the estimation was done.

In gases the strength of a transition is usually measured in terms of dipole momenta: in the case of solids, the difficulty to decide the proper correction for the local field due to the polarization induced into the crystal, leads to the introduction of the concept of emission cross-section. The stimulated emission cross-section $\sigma\nu$ is defined as the intensity gain of a laser beam per unity of population inversion when no saturation effects are present or no ESA processes occur. It is clear that such a parameter is extremely useful to determine the possibility to achieve laser effect. Entering the details of the method, some basic assumptions has to be done: first of all the energy spacing between the J manifolds should be not too large, on the other hand we have to suppose that the population in every sublevel respects the Boltzmann statistics in the case of steady-state pump. From the definition of $\sigma\nu$, it follows that the stimulated emission cross-section is proportional to the Einstein's

B coefficient, that can be obtained studying the absorption and spontaneous emission processes. Calling σ_{ji} and σ_{ij} the cross-sections for spontaneous emission and absorption respectively for the $j \rightarrow i$ transition, we have:

$$\sigma_{ji}(\nu) = \frac{g_i}{g_j}\sigma_{ij}(\nu) \tag{B.1}$$

$$\sigma_{ji}(\nu) = \frac{\lambda^2}{8\pi n^2}A_{ji}g_{ji}(\nu), \tag{B.2}$$

where g_i and g_j are the degeneracies of the i and j manifolds, A_{ji} is the spontaneous emission rate per unit time for the $j \rightarrow i$ transition, $g_{ji}(\nu)$ represents the normalized line shape factor and n is the refractive index of the crystalline host. In the case of low pump, the fluorescence signal I_{ji} will be given by:

$$I_{ji}(\nu)d\nu = GA_{ji}gji(\nu)h\nu d\nu N_j \tag{B.3}$$

where N_j is the population density of the level j and G is a calibration factor representing the fraction of the fluorescence which is collected by the optical detection apparatus corrected for the optical response of the system. Using Eq. B.2 and Eq. B.3, is it possible to write:

$$I_{ji}(\nu)d\nu = G\frac{8\pi n^2}{c^2}(\nu)h\nu^3 d\nu\sigma_{ji}(\nu)N_j. \tag{B.4}$$

B.1 Reciprocity method

After Eq. B.4 the two methods follow different ways: the reciprocity method derives the emission cross-section from the absorption coefficient spectra α (measured in cm^{-1}, the impurity concentration N (in ions/cm^3) and a detailed knowledge of the energy level positions of the ion. From the first two data it is possible to define the

absorption cross section σ_{abs} as:

$$\sigma_{abs} = \frac{\alpha}{N}. \tag{B.5}$$

Using Eq. B.1 and Eq. B.2, the cross sections for absorption and emission processes arising from the levels of the upper and lower states at energies E_i and E_j (measured from the lowest crystal field level) can be expressed as:

$$\sigma_{ems}(\nu) = \sum_{ij} g_j \left[\frac{exp(-E_j/kT)}{Z_u}\right] \sigma_{ji}(\nu) g_i \tag{B.6}$$

$$\sigma_{abs}(\nu) = \sum_{ij} g_i \left[\frac{exp(-E_i/kT)}{Z_l}\right] \sigma_{ij}(\nu) g_j \tag{B.7}$$

where the Z_u and Z_l are the partition functions of the upper and lower level respectively measured from the lowest Stark sublevel:

$$Z = \sum_k g_k exp(-E_k/kT). \tag{B.8}$$

It is useful to express the energy separation by means of

$$E_j - E_i = h\nu - E_{ZL} \tag{B.9}$$

where E_{ZL} is the zero phonon line, i.e. the energy of the transition from the lowest Stark sublevels of upper and lower manifold. Using Eqs. B.1 and B.9 in the ratio between Eqs. B.6 and B.7, we can write the final formula for the reciprocity method as:

$$\sigma_{ems}(\nu) = \sigma_{abs}(\nu) \frac{Z_l}{Z_u} exp\left(\frac{E_{ZL} - h\nu}{kT}\right). \tag{B.10}$$

B.2 Integral $\beta - \tau$ method

The integral $\beta - \tau$ method permits to determine the emission cross-section from the measurement of the fluorescence spectra and the knowledge of the radiative lifetime of the manifold. In the case of pulsed pump, the temporal behaviour of the fluorescent signal should be exponential with a time constant τ_f :

$$\frac{1}{\tau_f} = W^R + W^{NR} = \frac{1}{\tau_R} + W^{NR} \tag{B.11}$$

where τ_R is the radiative lifetime, W^R represents the radiative relaxation rate and W^{NR} the non-radiative one. A useful quantity is the radiative quantum efficiency η_a of a manifold a, defined as:

$$\eta_a = \sum_b \frac{W^R_{ab}}{\sum_b W^R_{ab} + \sum_b W^{NR}_{ab}} = \tau_a \sum_b W^R_{ab} \tag{B.12}$$

that is equal to the ratio between emitted photons and excited ions. Using the definition of quantum efficiency, it is possible to write:

$$\frac{1}{\tau_R} = \sum_j f_j \sum_i A_{ji} = \frac{\eta}{\tau_f} \tag{B.13}$$

with f_j representing the fraction of the population pumped in the sublevel j calculated via the Boltzmann statistics.

If τ_R is known, A_{ji} can be written as:

$$A_{ij} = \frac{\beta_{ij}}{f_i} \frac{1}{\tau_R} \tag{B.14}$$

where β_{ji} is the branching ratio for the transition $j \to i$, i.e. the fraction of the total photon flux emitted from the upper level. Such datum can be easily calculated

from the experimental fluorescence spectra:

$$\beta_{ij} = \frac{\int \frac{I_{ji}(\nu)}{h\nu} d\nu}{\sum_{kl} \int \frac{I_{kl}(\nu)}{h\nu} d\nu} = \frac{\int I_{ji}(\lambda) d\lambda}{\sum_{kl} \int I_{kl}(\lambda) d\lambda}. \tag{B.15}$$

In our approximation of steady-state pump, the total number of excited ions in the emitting multiplet N_{tot} is linked to the population of the manifold j through $N_j = f_j N_{tot}$. Summing over all the possible states and over all the frequencies both sides of Eq. B.3 and dividing by $h\nu$, it is possible to use Eq. B.13 to obtain:

$$\int \sum_{i,j} \frac{I_{ij}(\nu)}{h\nu} d\nu = \frac{G\eta N_{tot}}{\tau_f}. \tag{B.16}$$

Solving Eq. B.16 for GN_{tot} and replacing in Eq. B.4 we find:

$$\sigma_{ji}(\nu) = \frac{\eta c^2}{\tau_f f_i \left(\int \frac{I(\nu)}{h\nu} d\nu \right) 8\pi n^2 h\nu^3} I_{ij}(\nu) \tag{B.17}$$

where $I(\nu) = \sum_{i,j} I_{ij}(\nu)$ is the total fkuorescence, and the integral has to be performed on the entire fluorescent spectrum.

Considering the overlap with the other transitions $k \rightarrow l$ we must correct the stimulated emission cross-section as:

$$\sigma(\nu) = \sigma_{ij}(\nu) + \sum_{ij} \frac{f_k}{f_l} \sigma_{kl}(\nu). \tag{B.18}$$

Replacing Eq. B.17 in Eq. B.18 and converting to wavelength we have:

$$\sigma(\lambda) = \frac{\eta \lambda^5}{\tau_f f_i \left(\int \lambda I(\lambda) d\lambda \right) 8\pi n^2 c} I(\lambda). \tag{B.19}$$

In Eq. B.19 all the terms are known or can be calculated but f_j , and it has become normal practice to define an effective cross-section neglecting this factor. If

the crystal has different crystallographic axes the formula has to be corrected in:

$$\sigma(\lambda) = \frac{\eta\lambda^5}{\tau_f \frac{1}{3} \sum_s \left(\int \lambda I_s(\lambda) d\lambda\right) 8\pi n^2 c} I_p(\lambda). \tag{B.20}$$

where the sum has to be intended over the different polarizations and the index p is a label for the orientation.

Bibliography

[1] Yang W.-J.; Luo L.; Chen T.-M.; Wang N.-S. Luminescence and energy transfer of Eu- and Mn-coactived $CaAl_2Si_2O_2$ as a potential phosphor for white-light UVLED. *Chem. Mater.*, 17:3883–3888, 2005.

[2] H. Hanzawa X. Piao, T. Jorikawa and K.-I. Machida. Characterization and luminescence properties of $Sr_2Si_5N_8$:Eu^{2+} phosphor for white light-emitting diode illumination. *Applied Physic Letters*, 88:161908, 2006.

[3] A. Dodabalapur M. Strukelj, R.H. Jordan. Organic multilayer white emitting diodes. *J. Am. Chem. Soc.*, 118:1213–1214, 1996.

[4] J.T. Lim; N.H. Lee; Y.J. Ahn; G.W. Kang and C.H. Lee. White-light emitting device based on organic multilayer structure. *Current Applied Physics*, 2:295–298, 2002.

[5] P.T. Furuta; L. Deng; S. Garon; M.E. Thompson and J.M.J. Fréchet. Platinum-functionalized random copolimers for use in solution-processible efficient near white organic light-emitting diodes. *J. Am. Chem. Soc.*, 126:15388–15389, 2004.

[6] K. Hutchinson; J. Gao; G Shick; Y Rubin and F. Wudl. Bulky light bulbs: white light electroluminescence from a fluorescent C_{60} adduct-single layer organic LED. *J. Am. Chem. Soc.*, 121:5611–5612, 1999.

[7] J. Milliez, A. Rapaport, M. Bass, A. Cassanho, and H. P. Jenssen. High-Brightness White-Light Source Based on Up-Conversion Phosphor s. *Journal*

of Display Technology, 2:307–311, September 2006.

[8] H. Jennsen M. Bass, A. Rapaport. Dispersed crystallite up-conversion displays, 2003. Patent U.S. 6,654,161 B2.

[9] A. Rapaport M. Bass, J. Eichenholz. Optically written display. Patent US 6,897,999 B1.

[10] M. Raudsepp S. Sivukumar, F.C.J. M van Veggel. Bright white light through up-conversion of a single NIR source from sol-gel-derived thin film made with Ln^{3+}-doped LaF_3 nanoparticles. *J. Am. Chem. Soc.*, 127:12462–12465, 2005.

[11] J. Brodrick. Next-generation lighting initiative at the u.s. department of energy: Catalyzing science into the marketplace. *IEEE Journal of Display Technology*, 3:91, 2007.

[12] T. Sandrock, T. Danger, E. Heumann, G. Huber, and B. H. T. Chai. Efficient continuous wave-laser emission of Pr^{3+}-doped fluorides at room temperature. *Applied Physics B: Lasers and Optics*, 58:149–151, 1994. 10.1007/BF01082350.

[13] T. Fukuda P. Rudolph. Fiber crystal growth from the melt. *Crystal Research and Technology*, 34:3–40, 1999.

[14] K. Scholle, S. Lamrini, P. Koopmann, and P. Fuhrberg. 2 μm laser sources and their possible applications. In B. Pal, editor, *Frontiers in Guided Wave Optics and Optoelectronics*, pages 491–496. Intech, 2010.

[15] M. Mond, E. Heumann, G. Huber, S. Kuck, V.I. Levchenko, V.N. Yakimovich, V.E. Shcherbitsky, V.E. Kisel, and N.V. Kuleshov. Passive q-switching of a diode-pumped Tm:YAG laser by Cr^{2+}:ZnSe. In *Lasers and Electro-Optics Europe, 2003. CLEO/Europe. 2003 Conference on*, page 38, june 2003.

[16] Martha Segura, Martin Kadankov, Xavier Mateos, Maria Cinta Pujol, Joan Josep Carvajal, Magdalena Aguiló, Francesc Díaz, Uwe Griebner, and Valentin Petrov. Passive Q-switching of the diode pumped Tm^{3+}:$KLu(WO_4)_2$

laser near 2-μm with Cr^{2+}:ZnS saturable absorbers. *Opt. Express*, 20(4):3394–3400, Feb 2012.

[17] F. Cornacchia, A. Toncelli, and M. Tonelli. lasers with fluoride crystals: Research and development. *Progress in Quantum Electronics*, 33(2-4):61 – 109, 2009.

[18] S.A. Payne, L.L. Chase, L.K. Smith, W.L. Kway, and W.F. Krupke. Infrared cross-section measurements for crystals doped with Er^{3+}, Tm^{3+}, and Ho^{3+}. *IEEE Journal of Quantum Electronics*, 28(11):2619 –2630, nov 1992.

[19] M.S. Shur and R. Zukauskas. Solid-state lighting: Toward superior illumination. *Proceedings of the IEEE*, 93(10):1691 –1703, oct. 2005.

[20] DTI global watch mission report. LED lighting technology: lessons from the USA., 2006.

[21] Jr. Nick Holonyak and S. F. Bevacqua. Coherent (visible) light emission from $Ga(As_{1-x}P_x)$ junctions. *Applied Physics Letters*, 1(4):82–83, 1962.

[22] H. Kroemer. A proposed class of hetero-junction injection lasers. *Proceedings of the IEEE*, 51(12):1782 –1783, dec. 1963.

[23] A. Duggal A. Bergh, G. Craford and R. Haitz. The promise and challenge of solid-state lighting. *Physics Today*, pages 42–47, 2001.

[24] Michael R. Krames, Oleg B. Shchekin, Regina Mueller-Mach, GerdO. Mueller, Ling Zhou, Gerard Harbers, and M. George Craford. Status and future of high-power light-emitting diodes for solid-state lighting. *J. Display Technol.*, 3(2):160–175, Jun 2007.

[25] Andrew J. Steckl, Jason Heikenfeld, and Steven C. Allen. Light wave coupled flat panel displays and solid-state lighting using hybrid inorganic/organic materials. *J. Display Technol.*, 1(1):157, Sep 2005.

[26] H. Matsubara; K.Katayama; T.Takebe. White color light emitting diode and neutral color light emitting diode, 1999. U.S, patent 6,337,536 B1.

[27] Woan-Jen Yang and Teng-Ming Chen. White-light generation and energy transfer in $SrZn_2(PO_4)_2$:Eu,Mn phosphor for ultraviolet light-emitting diodes. *Applied Physics Letters*, 88(10):101903, 2006.

[28] C.W. Tang and S.A. VanSlyke. Organic electroluminescent diodes. *Appl. Phys. Lett.*, 51:913, 1987.

[29] C. W. Tang, S. A. VanSlyke, and C. H. Chen. Electroluminescence of doped organic thin films. *Journal of Applied Physics*, 65(9):3610–3616, 1989.

[30] Benjamin C. Krummacher, Vi-En Choong, Mathew K. Mathai, Stelios A. Choulis, Franky So, Frank Jermann, Tim Fiedler, and M. Zachau. Highly efficient white organic light-emitting diode. *Applied Physics Letters*, 88(11):113506, 2006.

[31] K. Hutchison, J. Gao, G. Schick, Y. Rubin, and F. Wudl. Bucky light bulbs: White light electroluminescence from a fluorescent C_{60} adduct-single layer organic LED. *Journal of the American Chemical Society*, 121(23):5611–5612, 1999.

[32] Yulong Shen, Matthias W. Klein, Daniel B. Jacobs, J. Campbell Scott, and George G. Malliaras. Mobility-dependent charge injection into an organic semiconductor. *Phys. Rev. Lett.*, 86:3867–3870, Apr 2001.

[33] P. Schlotter, R. Schmidt, and J. Schneider. Luminescence conversion of blue light emitting diodes. *Applied Physics A: Materials Science & Processing*, 64:417–418, 1997. 10.1007/s003390050498.

[34] A. Toncelli, L. Bonelli, R. Faoro, D. Parisi, M. Tonelli. Investigation of Pr-doped fluoride crystals as possible white-light emitters. *Optical Materials*, 31:1205–1209, 2008.

[35] S. Hufner. *Optical Spectra of Transparent Rare Earth Compounds*. Academic Press, 1978.

[36] G. H. Dieke and H. M. Crosswhite. *Spectra and Energy levels of Rare Earth*

Ions in crystals. J. Wiley & Sons, New York, 1968.

[37] H. Bethe. Termaufspaltung in kristallen. *Annalen der Physik*, 395(2):133–208, 1929.

[38] D. H. Brainard. *Handbook of photonics*, chapter 26. McGRAW-HILL, 1995.

[39] J. M. Palmer. *"Radiometry and photometry: units and conversions," in Handbook of Optics, vol. III.* McGraw-Hill, Inc., 2001.

[40] J. Schanda. *Colorimetry Understanding the CIE System.* John Wiley & Sons, 2007.

[41] C.R. Nave. http://hyperphysics.phy-astr.gsu.edu/hbase/hframe.html.

[42] C. J. Ballhausen. *Introduction to Ligand Field Theory.* McGraw-Hill New York, 1962.

[43] M. Tinkham. *Group Theory and quantum mechanics.* McGraw-Hill, 1964.

[44] G. H. Dieke and H. M. Crosswhite. The spectra of the doubly and triply ionized rare earths. *Appl. Opt.*, 2:675, 1963.

[45] L. A. Riseberg and H. W. Moos. Multiphonon orbit-lattice relaxation of excited states of rare-earth ions in crystals. *Phys. Rev.*, 174:429–438, Oct 1968.

[46] L.A. Risenberg and M.J. Weber. *Relaxation phenomena in rare earth luminescence.* North Holland, 1976.

[47] Th. Föster. Zwischenmolekulare energiewanderung und fluoreszenz. *Annalen der Physik*, 437(1-2):55–75, 1948.

[48] D. L. Dexter. A theory of sensitized luminescence in solids. *The Journal of Chemical Physics*, 21(5):836–850, 1953.

[49] B. R. Pamplin. *Crystal growth. Pergamon Press, Oxford*, volume 10. Pergamon Press, Oxford, 1975.

[50] L.H. Guilbert, Gesland J.Y., A. Bulou, and Retoux R. Structure and raman spectroscopy of czochralski-grown barium yttrium and barium ytterbium fluorides crystals. *Materials Research Bulletin*, 28(9):923–930, 1993. cited By

(since 1996) 52.

[51] O. Izotova and V. Aleksandrov. *Sov. Phys. Doklady*, 15:525, 1970.

[52] A. Toncelli, M. Tonelli, A. Cassanho, and H.P. Jenssen. Spectroscopy and dynamic measurements of a Tm,Dy:BaY_2F_8 crystal. *Journal of Luminescence*, 82(4):291 – 298, 1999.

[53] M. J. Weber, editor. *Handbook of optical materials*. CRC Press, 2003.

[54] L. G. DeShazer, S. C. Rand, and B. A. Wechsler. *Laser crystals, Handbook of Laser Science and Technology*, volume Vol. V: Optical Materials. CRC Press, 2000.

[55] S. Aléonard, Y. L. Fur, L. Pontonnier, M. Gorius, and M.-T. Roux. Quelques fluoruresmixtes terre rare-metal alcalin de structures derivés de celle de la fluorine. *Ann. Chim. Fr.*, 3:417, 1978.

[56] Ortwin Greis and John M. Haschke. Rare earth fluorides. In Jr. Karl A. Gschneidner and LeRoy Eyring, editors, *Handbook of the physict and chemistry of rare earths*, volume 5 of *Handbook on the Physics and Chemistry of Rare Earths*, chapter 45, pages 387 – 460. Elsevier, 1982.

[57] S. Alèonard, M. Labeau, Y. Le Fur, and M.F. Gorius. Etude du system KF-ErF_3. *Materials Research Bulletin*, 8(6):605 – 617, 1973.

[58] Y.Yanaguchi; K.M. Dummdorf; H.P. Jenssen and A.Cassanho. Spectroscopy of Nd:KYF_4. *Osa Proceeding on solid-state lasers*, 15:36–40, 1993.

[59] N.M. Khaidukov Y. Le Fur and S. Aléonard. Structure of KYF_4. *Acta Cryst.*, C48, 1992.

[60] Toomas H. Allik, Larry D. Merkle, Richard A. Utano, Bruce H. T. Chai, J.-L. V. Lefaucheur, Heika Voss, and G. Jeffrey Dixon. Crystal growth, spectroscopy, and laser performance of Nd^{3+}:KYF_4. *J. Opt. Soc. Am. B*, 10(4):633–637, Apr 1993.

[61] Dubinskii M.A., Khaidukov N.M., Garipov I.G., DemYanets L.N., Naumov

A.K., Semashko V.V., and Malyusov V.A. Spectral-kinetic and lasing characteristics of new Nd^{3+} -activated laser hosts of the KF-YF_3 system. *Journal of Modern Optics*, 37(8):1355–1360, 1990.

[62] X. X. Zhang, P. Hong, M. Bass, and B. H. T. Chai. Multisite nature and efficient lasing at 1041 and 1302 nm in Nd^{3+} doped potassium yttrium fluoride. *Applied Physics Letters*, 66(8):926–928, 1995.

[63] A. Ellens, S.J. Kroes, J. Sytsma, G. Blasse, and N.M. Khaidukov. Luminescence of some ternary gadolinium fluoride crystals. *Materials Chemistry and Physics*, 30(2):127 – 133, 1991.

[64] E. Sani; A Toncelli; M. Tonelli and F. Traverso. Growth and spettroscopic analysis of Tm,Ho:KYF_4. *Journal of Physics: Condensed Matter*, 16:241–252, 2004.

[65] M Bouffard, T Duvaut, J P Jouart, N M Khaidukov, and M F Joubert. Site-selective upconversion excitation of Er^{3+}:KYF_4. *J. Phys.: Condens. Matter*, 1999.

[66] R. E. Peale, H. Weidner, P. L. Summers, and B. H. T. Chai. Site-selective spectroscopy of Ho^{3+}:KYF_4. *Journal of Applied Physics*, 75(1):502–506, 1994.

[67] Y. Le Fur, N. M. Khaidukov, and S. Aléonard. Structure of $KY_{0.95}Er_{0.05}F_4$. *Acta Crystallographica Section C*, 48(11):2062–2064, Nov 1992.

[68] E.N. Silva; A.P. Ayala; J-Y. Gesland and R.L. Moreira. Vibrational spectrum and lattice dynamics of KY_3F_{10} single crystals. *Vibrational Spectroscopy*, 37:21–26, 2004.

[69] C.A. Morrison and R.P. Leavitt. Spectroscopic properties of triply ionized lanthanides in transparent host crystals. In Jr. Karl A. Gschneidner and LeRoy Eyring, editors, *Handbook of the physict and chemistry of rare earths*, volume 5 of *Handbook on the Physics and Chemistry of Rare Earths*, chapter 46, pages 461–692. Elsevier, 1992.

[70] Alexander A. Kaminskii, Ken ichi Ueda, and Noboru Uehara. New laser-diode-pumped cw laser based on Nd^{3+}-ion-doped tetragonal $LiLuF_4$ crystal. *Japanese Journal of Applied Physics*, 32(Part 2, No. 4B):L586–L588, 1993.

[71] F. Cornacchia; A.Richter; E. Heumann; G.Hubner; D. Parisi and M.Tonelli. Visible emission of solid state pumped $LiLuF_4$:Pr^{3+}. *Optics Express*, 15:992–1002, 2007.

[72] C.M. Combes; P. Dorenbos; C.W.E. van Eijk; C.Pedrini; H.W. Den Hartog; J.Y. Gesland and P.A. Rodnyi. Optical and scintillation properties of Ce^{3+} doped $LiYF_4$ and $LiLuF_4$ crystals. *Journal of Luminescence*, 71:65–70, 1997.

[73] Alexandr A Kaminskii, A I Lyashenko, N P Isaev, V N Karlov, V L Pavlovich, S N Bagayev, A V Butashin, and L E Li. Quasi-cw Pr^{3+} : $LiYF_4$ laser with λ= 0.6395 μm and an average output power of 2.3 W. *Quantum Electronics*, 28(3):187, 1998.

[74] R. W. G. Wycko. In *Crystal Structures*, volume 3. Interscience Publishers, 1965.

[75] L. L. Chase L. D. DeLoach, S. A. Payne, L. K. Smith, W. L. Kway, and W. F. Krupke. valuation of absorption and emission properties of Yb^{3+} doped crystals for laser applications. *IEEE JOURNAL OF QUANTUM ELECTRONICS*, 29:1179, 1993.

[76] S.H. Smith and B.M. Wanklyn. Flux growth of rare earth vanadates and phosphates. *Journal of Crystal Growth*, 21(1):23 – 28, 1974.

[77] W.O. Milligan, D.F. Mullica, G.W. Beall, and L.A. Boatner. Structural investigations of YPO_4, $ScPO_4$, and $LuPO_4$. *Inorganica Chimica Acta*, 60(0):39 – 43, 1982.

[78] Bryan C. Chakoumakos, Marvin M. Abraham, and Lynn A. Boatner. Crystal structure refinements of zircon-type MVO_4 (M = Sc, Y, Ce, Pr, Nd, Tb, Ho, Er, Tm, Yb, Lu). *Journal of Solid State Chemistry*, 109(1):197 – 202, 1994.

[79] L. Shea Rohwer; J.E. Martin. Measuring the absolute quantum efficiency of luminescent materials. *Journal of luminescence*, 115:77–90, 2005.

[80] E. P. A. United States environmental protection agency. Lighting fundamentals., 1997.

[81] A. J. Milliez. *Up-conversion in rare-earth doped micro-particles applied to new emissive 2D display.* PhD thesis, University of central Florida, Orlando, Florida, 2006.

[82] B.W. D'Andrade; M.E. Thompson and S.R. Forrest. Controlling exciton diffusion in multilayer white phosphorescent organic light emitting device. *Advanced materials*, pages 147–150, 2002.

[83] A.R. Duggal; J.J. Shiang; C.M. Heller and D.F. Foust. Organic light-emitting device for illumination quality light. *Applied physics letters*, 80:3470–3472, 2002.

[84] Z. Hao; J. Zhang; X. Zhang; X. Sun; Y. Luo; S. Lu and Wang X-J. White light emitting diode by using α-$Ca_2P_2O_7$:Eu^{2+}, Mn^{2+} phosphor. *Appl. Phys. Lett.*, 90:261113, 2007.

[85] Color and Vision Research Laboratories.

[86] C.S. McCamy. Correlated color temperature as an explicit function of chromaticity coordinates. *Color Research and Application*, 17:142, 1992.

[87] Erratum. *Color Research and Application*, 18(2):150–150, 1993.

[88] Javier Hernández-Andrés, Raymond L. Lee, and Javier Romero. Calculating correlated color temperatures across the entire gamut of daylight and skylight chromaticities. *Appl. Opt.*, 38(27):5703–5709, Sep 1999.

[89] Kanji BANDO, Kensho SAKANO, Yasunobu NOGUCHI, and Yoshinori SHIMIZU. Development of high-bright and pure-white led lamps. *Journal of Light and Visual Environment*, 22(1):1.2–1.5, 1998.

[90] A. Mohan Babu B.C. Jamalaiah, J. Suresh Kumar, T. Suhasini, and L. Rama

Moorthy. Photoluminescence properties of Sm^{3+} in LBTAF glasses. *Journal of luminescence*, 129:363, 2009.

[91] R.S.Pandher W.Tian and B.R.Reddy. Efficient infrared quantum counter and excited-state absorption cross-section measurements in europium-doped calcium fluoride. *J.Opt.Soc.Am.B*, 18:1627, 2001.

[92] H. Riesen and W. A. Kaczmarek. Efficient X-ray generation of Sm^{2+} in nanocrystalline $BaFCl/Sm^{3+}$:a photoluminescent X-ray storage phosphor. *Inorg. Chem.*, 46:7235–723, 2007.

[93] A. Di Lieto. Private communication.

[94] Alessandra Toncelli, Francesca Moglia, and Mauro Tonelli. Optical properties of ions in for completely-solid-state cw UV laser emission. *Optical Materials*, 33(1):22 – 25, 2010.

[95] A. Bensalah, Y. Guyot, M. Ito, A. Brenier, H. Sato, T. Fukuda, and G. Boulon. Growth of Yb^{3+}-doped $YLiF_4$ laser crystal by the Czochralski method. attempt of Yb^{3+} energy level assignment and estimation of the laser potentiality. *Optical Materials*, 26(4):375 – 383, 2004. Third International Symposium on Lasers and Nonlinear Optical Materials (ISLNOM-3).

[96] D. Parisi, S. Veronesi, and M. Tonelli. Effects of polarized excitation on the ^3P_j manifolds emission in $KYF_4:Pr^{3+}$ single crystal. *Optical Materials*, 34(2):410 – 413, 2011. Selected papers from the 7th European-Israeli Workshop on "Materials for and by Optics" Claude Bernard/Lyon 1 University December 8-9, 2010 Villeurbanne France.

[97] S. Veronesi, D. Parisi, F. Marchetti, and M. Tonelli. Effect of Ce co-doping on KY_3F_{10}:Pr crystals. *Journal of Physics and Chemistry of Solids*, 71(6):913 – 917, 2010.

[98] Mathieu Laroche, Alain Braud, Sylvain Girard, Jean Louis Doualan, Richard Moncorge, Michel Thuau, and Larry D. Merkle. Spectroscopic investigations

of the 4f-5d energy levels of Pr^{3+} in fluoride crystals by excited-state absorption and two-step excitation measurements. *J. Opt. Soc. Am. B*, 16(12):2269–2277, Dec 1999.

[99] L. A. Riseberg and H. W. Moos. Multiphonon orbit-lattice relaxation in $labr_3$, $lacl_3$, and laf_3. *Phys. Rev. Lett.*, 19:1423–1426, Dec 1967.

[100] W. D. Partlow and H. W. Moos. Multiphonon relaxation in $LaCl_3$:Nd^{3+}. *Phys. Rev.*, 157:252–256, May 1967.

[101] Ratnakar R. Neurgaonkar and Warren K. Cory. Progress in photorefractive tungsten bronze crystals. *J. Opt. Soc. Am. B*, 3(2):274–282, Feb 1986.

[102] G. Foulon, A. Brenier, M. Ferriol, M.-T. Cohen-Adad, and G. Boulon. Laser heated pedestal growth and spectroscopic properties of neodymium doped $Ba_2NaNb_5O_{15}$ single crystal fibers. *Chemical Physics Letters*, 249(56):381 – 386, 1996.

[103] A. Rodenas, D. Jaque, F. Agull-Rueda, and A.A. Kaminskii. Self-activated Nd^{3+}:$Ba_2NaNb_5O_{15}$ optical super-lattices: Micro characterization and non-collinear laser light generation. *Optics Communications*, 262(2):220 – 223, 2006.

[104] F.Carrillo Romo, C. Goutaudier, Y. Guyot, M.Th. Cohen-Adad, G. Boulon, K. Lebbou, A. Yoshikawa, and T. Fukuda. Yb^{3+}-doped $Ba_2NaNb_5O_{15}$ (BNN) growth, characterization and spectroscopy. *Optical Materials*, 16(12):199 – 206, 2001. Proceedings of the fourth French–Israeli Workshop: Optical Properties.

[105] S. Bigotta, G. Gorini, A. Toncelli, M. Tonelli, E. Cavalli, and E. Bovero. Optical spectra of Er^{3+} in $Ba_2NaNb_5O_{15}$ single crystals. *Optical Materials*, 28(4):395 – 400, 2006.

[106] S. Bigotta, A. Toncelli, M. Tonelli, E. Cavalli, and E. Bovero. Spectroscopy and energy transfer parameters of Tm^{3+}- and Ho^{3+}-doped $Ba_2NaNb_5O_{15}$ single

crystals. *Optical Materials*, 30(1):129 – 131, 2007. Selected papers from the 4th International Symposium on Laser, Scintillator and Nonlinear Optical Matetials: ISLNOM-44th International Symposium on Laser, Scintillator and Nonlinear Optical Materials.

[107] S Bigotta, M Tonelli, and E Cavalli. $Ba_2NaNb_5O_{15}$ single crystals doped with Tm^{3+} and Ho^{3+} : spectroscopy and energy transfer parameters. *Journal of Physics: Condensed Matter*, 19(47):476208, 2007.

[108] Enrico Cavalli, Alessandro Belletti, Rachid Mahiou, and Philippe Boutinaud. Luminescence properties of $Ba_2NaNb_5O_{15}$ crystals activated with Sm^{3+}, Eu^{3+}, Tb^{3+} or Dy^{3+} ions. *Journal of Luminescence*, 130(4):733 – 736, 2010.

[109] Altomare A, Burla M C, Camalli M, Cascarano G andGiacovazzo C, Guagliardi A, Moliterni A G G, Polidori G, and Spagna R. SIR2002, program for crystal structure solution and refinement IRMEC-CNR, bari, italy, 2002.

[110] Sheldrick G M. SHELXL97, program for crystal structure refinement university of gottingen, germany, 1993.

[111] P. B. Jamieson, S. C. Abrahams, and J. L. Bernstein. Ferroelectric tungsten bronze-type crystal structures. ii. barium sodium niobate $Ba_{4+x}Na_{2-2x}Nb_{10}O_{30}$. *The Journal of Chemical Physics*, 50(10):4352–4363, 1969.

[112] P. J. Lin and L. A. Bursill. Superlattice structure of ferroelectric barium sodium niobate (BNN). *Acta Crystallographica Section B*, 43(6):504–512, Dec 1987.

[113] P Labbe, H Leligny, B Raveau, J Schneck, and J C Toledano. X-ray structural determination of the quasi-commensurate phase of barium sodium niobate. *Journal of Physics: Condensed Matter*, 2(1):25, 1990.

[114] Simone Fabbrici, Erica Montanari, Lara Righi, Gianluca Calestani, and

Andrea Migliori. Charge order and tilt modulation in multiferroic $K_xM^{II}_xM^{III}_{1-x}F_3(0.4 \leq x \leq 0.6)$ transition metal fluorides with tetragonal tungsten bronze structure. *Chemistry of Materials*, 16(16):3007–3019, 2004.

[115] F. Mezzadri, S. Fabbrici, E. Montanari, L. Righi, G. Calestani, E. Gilioli, F. Bolzoni, and A. Migliori. Structural properties and multiferroic phase diagram of $K_{0.6}Fe^{ii}_{0.6}Fe^{iii}_{0.4}F_3$ fluoride with TTB structure. *Phys. Rev. B*, 78:064111, Aug 2008.

[116] R. Naccache, F. Vetrone, A. Speghini, M. Bettinelli, and J. A. Capobianco. Cross-relaxation and upconversion processes in Pr^{3+} singly doped and Pr^{3+}/Yb^{3+} codoped nanocrystalline $Gd_3Ga_5O_{12}$: The sensitizer/activator relationship. *The Journal of Physical Chemistry C*, 112(20):7750–7756, 2008.

[117] H.-R. Xia, L.-X. Li, H. Yu, X.-L. Meng, L. Zhu, and L.-J. Hu. Raman and infrared spectra of Nd-doped barium sodium niobate crystals. *Crystal Research and Technology*, 34(7):901–910, 1999.

[118] Marco Bettinelli, Adolfo Speghini, Airn Rdenas, Pablo Molina, Maria de la O Ramrez, Brbara Capote, Daniel Jaque, Luisa E. Baus, and Jos Garca Sol. Luminescence of lanthanide ions in strontium barium niobate. *Journal of Luminescence*, 122-123(0):307 – 310, 2007. Luminescence and Optical Spectroscopy of Condensed Matter Proceedings of the 2005 International Conference on Luminescence and Optical Spectroscopy of Condensed Matter 2005 International Conference on Luminescence and Optical Spectroscopy of Condensed Matter.

[119] P Boutinaud, E Cavalli, and M Bettinelli. Emission quenching induced by intervalence charge transfer in Pr^{3+} -or Tb^{3+} -doped $YNbO_4$ and $CaNb_2O_6$. *Journal of Physics: Condensed Matter*, 19(38):386230, 2007.

[120] Nakazawa E. *Phosphor Handbook*. Boca Raton, FL:CRC Press, 1999.

[121] Qiang Su, Zhiwu Pei, Lisheng Chi, Hongjie Zhang, Zhongyi Zhang, and Feng

Zou. The yellow-to-blue intensity ratio (Y/B) of Dy^{3+} emission. *Journal of Alloys and Compounds*, 192(1-2):25 – 27, 1993.

[122] Enrico Cavalli, Enrico Bovero, Nicola Magnani, Mariola O Ramirez, Adolfo Speghini, and Marco Bettinelli. Optical spectroscopy and crystal-field analysis of $YAl_3(BO_3)_4$ single crystals doped with dysprosium. *Journal of Physics: Condensed Matter*, 15(7):1047, 2003.

[123] Daniela Parisi, Alessandra Toncelli, Mauro Tonelli, Enrico Cavalli, Enrico Bovero, and Alessandro Belletti. Optical spectroscopy of BaY_2F_8 :Dy^{3+}. *Journal of Physics: Condensed Matter*, 17(17):2783, 2005.

[124] Enrico Cavalli, Enrico Bovero, and Alessandro Belletti. Optical spectroscopy of $CaMoO_4$:Dy^{3+} single crystals. *Journal of Physics: Condensed Matter*, 14(20):5221, 2002.

[125] Zhiliang Xiu, Zhongsen Yang, Mengkai Lü, Suwen Liu, Haiping Zhang, and Guangjun Zhou. Synthesis, structural and luminescence properties of Dy^{3+}-doped YPO_4 nanocrystals. *Optical Materials*, 29(4):431 – 434, 2006.

[126] Hua Lai, Amurisana Bao, Yuming Yang, Weiwei Xu, Yanchun Tao, and Hua Yang. Preparation and luminescence property of Dy^{3+}-doped YPO_4 phosphors. *Journal of Luminescence*, 128(3):521 – 524, 2008.

[127] Enrico Cavalli, Marco Bettinelli, Alessandro Belletti, and Adolfo Speghini. Optical spectra of yttrium phosphate and yttrium vanadate single crystals activated with Dy^{3+}. *Journal of Alloys and Compounds*, 341(12):107 – 110, 2002. Proceedings of the 5th International Conference on Excited States of Transition Elements.

[128] Amurisana Bao, Hua Yang, Chunyan Tao, Ying Zhang, and Lili Han. Luminescent properties of nanoparticles $YP_xV_{1-X}O_4$:Dy phosphors. *Journal of Luminescence*, 128(1):60 – 66, 2008.

[129] Alexander A. Kaminskii. *Crystalline Lasers: Physical Processes And Operating Schemes*. Boca Raton, FL: CRC Press, 1996.

[130] W. T. Carnall, G. L. Goodman, K. Rajnak, and R. S. Rana. A systematic analysis of the spectra of the lanthanides doped into single crystal LaF_3. *The Journal of Chemical Physics*, 90(7):3443–3457, 1989.

[131] H. M. Grosswhite and H. Crosswhite. Parametric model for f-shell configurations. i. the effective-operator hamiltonian. *J. Opt. Soc. Am. B*, 1(2):246–254, Apr 1984.

[132] Giulio Racah. Theory of complex spectra. ii. *Phys. Rev.*, 62:438–462, Nov 1942.

[133] D J Newman and B Ng. The superposition model of crystal fields. *Reports on Progress in Physics*, 52(6):699, 1989.

[134] D.J. Newman. Theory of lanthanide crystal fields. *Advances in Physics*, 20(84):197–256, 1971.

[135] A.J. Freeman and J.P. Desclaux. Dirac-fock studies of some electronic properties of rare-earth ions. *Journal of Magnetism and Magnetic Materials*, 12(1):11 – 21, 1979.

[136] M. J. Weber and R. W. Bierig. Paramagnetic resonance and relaxation of trivalent rare-earth ions in calcium fluoride. i. resonance spectra and crystal fields. *Phys. Rev.*, 134:A1492–A1503, Jun 1964.

[137] D. J. Newman and Betty Ng. *Crystal Field Handbook*. Cambridge University Press, 2000.

[138] B. R. Judd. Optical absorption intensities of rare-earth ions. *Phys. Rev.*, 127:750–761, Aug 1962.

[139] G. S. Ofelt. Intensities of crystal spectra of rare-earth ions. *The Journal of Chemical Physics*, 37(3):511–520, 1962.

[140] C.K. Jayasankar and E. Rukmini. Spectroscopic investigations of Dy^{3+} ions in

borosulphate glasses. *Physica B: Condensed Matter*, 240(3):273 – 288, 1997.

[141] Hairong Zheng and Richard S. Meltzer. Nonradiative relaxation of rare-earth ions in YPO_4 crystal. *Journal of Luminescence*, 122123(0):478 – 480, 2007.

[142] Alexander A. Kaminskii, John B. Gruber, Sergei N. Bagaev, Ken-ichi Ueda, Uwe Hömmerich, Jae Tae Seo, Doyle Temple, Bahram Zandi, Aleksei A. Kornienko, Elena B. Dunina, Aleksei A. Pavlyuk, Rima F. Klevtsova, and Fedor A. Kuznetsov. Optical spectroscopy and visible stimulated emission of Dy^{3+} ions in monoclinic $\alpha KY(WO_4)_2$ and $\alpha KGd(WO_4)_2$ crystals. *Phys. Rev. B*, 65:125108, Mar 2002.

[143] Dhiraj K. Sardar, William M. Bradley, Raylon M. Yow, John B. Gruber, and Bahram Zandi. Optical transitions and absorption intensities of $Dy^{3+}(^4F_9)$ in YSGG laser host. *Journal of Luminescence*, 106(34):195 – 203, 2004.

[144] Mitio Inokuti and Fumio Hirayama. Influence of energy transfer by the exchange mechanism on donor luminescence. *The Journal of Chemical Physics*, 43(6):1978–1989, 1965.

[145] Martha Segura. Q-switching experiments on Tm:KLuWO and Tm:YLF lasers. Max Born Institute internal report.

[146] L. E. Batay, A. N. Kuzmin, A. S. Grabtchikov, V. A. Lisinetskii, V. A. Orlovich, A. A. Demidovich, A. N. Titov, V. V. Badikov, S. G. Sheina, V. L. Panyutin, M. Mond, and S. Kück. Efficient diode-pumped passively Q-switched laser operation around 1.9 μm and self-frequency raman conversion of tm-doped $KY(WO_4)_2$. *Applied Physics Letters*, 81(16):2926–2928, 2002.

[147] M.S. Gaponenko, I.A. Denisov, V.E. Kisel, A.M. Malyarevich, A.A. Zhilin, A.A. Onushchenko, N.V. Kuleshov, and K.V. Yumashev. Diode-pumped Tm:$KY(WO_4)_2$ laser passively Q-switched with PbS-doped glass. *Applied Physics B*, 93:787–791, 2008.

[148] M.S. Gaponenko, A.A. Onushchenko, V.E. Kisel, A.M. Malyarevich, K.V.

Yumashev, and N.V. Kuleshov. Compact passively Q-switched diode-pumped Tm:$KY(WO_4)_2$ laser with 8 ns 30μJ pulses. *Laser Physics Letters*, 9(4):291–294, 2012.

[149] Baoquan Yao, Yi Tian, Gang Li, and Yuezhu Wang. InGaAs/GaAs saturable absorber for diode-pumped passively Q-switched dual-wavelength Tm:YAP lasers. *Opt. Express*, 18(13):13574–13579, Jun 2010.

[150] X.L. Zhang, L. Li, J.H. Cui, and Y.L. Ju. Tunable repetition frequency passively Q-switched Tm,Ho:YLF laser with Cr:ZnS as a saturable absorber. *Laser Physics*, 21:1581–1584, 2011.

[151] B. Aull and H. Jenssen. Vibronic interactions in Nd:YAG resulting in non reciprocity of absorption and stimulated emission cross sections. *Quantum Electronics, IEEE Journal of*, 18(5):925 – 930, may 1982.

[152] H. P. Jenssen, A. Linz, R. P. Leavitt, C. A. Morrison, and D. E. Wortman. Analysis of the optical spectrum of Tm^{3+} in $LiYF_4$. *Phys. Rev. B*, 11:92–101, Jan 1975.

[153] A. Dergachev and P. F. Moulton. In J. Zayhowski, editor, *Advanced Solid-State Photonics*, volume 83 of *OSA Trends in Optics and Photonics(Optical Society of America)*. 2003.

[154] P. Moulton. Mid-infrared coherent sources (mics 2005), paper we7, 6-11 November 2005.

[155] Tzong-Yow Tsai and Milton Birnbaum. Q-switched 2-μm lasers by use of a Cr^{2+}:ZnSe saturable absorber. *Appl. Opt.*, 40(36):6633–6637, Dec 2001.

[156] Haohai Yu, Valentin Petrov, Uwe Griebner, Daniela Parisi, Stefano Veronesi, and Mauro Tonelli. Compact passively Q-switched diode-pumped Tm:$LiLuF_4$ laser with 1.26 mJ output energy. *Opt. Lett.*, 37(13):2544–2546, Jul 2012.

[157] Kenneth L. Kelly. Lines of constant correlated color temperature based on MacAdam's (u,υ) uniform chromaticity transformation of the CIE diagram.

J. Opt. Soc. Am., 53(8):999–1002, Aug 1963.

[158] A. R. ROBERTSON. Computation of correlated color temperature and distribution temperature. *J. Opt. Soc. Am.*, 58(11):1528–1535, Nov 1968.

[159] J. Schanda and M. Danyi. Correlated color-temperature calculations in the CIE 1976 chromaticity diagram. *Color Research & Application*, 2(4):161–163, 1977.

[160] M. Krystek. An algorithm to calculate correlated colour temperature. *Color Research & Application*, 10(1):38–40, 1985.

[161] Qiu Xingzhong. Formulas for computing correlated color temperature. *Color Research & Application*, 12(5):285–287, 1987.

List of Figures

1.1 The evolution of total efficacy of solid-state lighting technologies [23] 9
1.2 Three main approaches to solid-state lighting [25] 11
1.3 Four main approaches to OLED production [30] 13

2.1 Response of human eye: absolute spectral luminous efficiency functions for photopic and scotopic. 19
2.2 Normalized colour sensitivity of the red-, green- and blue-sensitive cones of the human eye [41] 21
2.3 (a)The historical RGB colour matching functions and (b) the CIE 1931 colour matching functions [41].In both case the vertical axis is the tristimulus value 22
2.4 The 1931 CIE chromaticity diagram [41] 24
2.5 Typical values or the level splitting in rare earth ions. 31
2.6 Scheme of the energy levels of all triply ionized rare-earth ions [44]. . 33
2.7 Multiphonon relaxation rate as a function of the temperature for different number of phonons. 38
2.8 Multiphonon relaxation rate as a function of the energy gap in different matrices. 39
2.9 Cooperative relaxation. 40
2.10 Schemes representing the various energy transfer mechanisms. 44

3.1 View of the unit cell of BaY_2F_8 . The polyhedron defined by the surrounding fluoride ligands of an Y^{3+}-ion is marked [50]. 47
3.2 Structure of KYF_4 [58]. The illustration is the z = 1/3 cation plane projected along c. 49
3.3 Scheme of the unit cell of KY_3F_{10} crystal. The polyhedron defined by the surrounding fluoride ligands of an Y^{3+}-ion is marked. 50
3.4 View of the unit cell of $LiLuF_4$. The polyhedron defined by the surrounding fluoride ligands of an Y^{3+}-ion is marked [70] 51
3.5 Internal scheme of Cary 500 spectrophotometer. 55
3.6 Internal scheme of Triax 320 monochromator. 57
3.7 Scheme of the experimental apparatus for fluorescence measurements 60
3.8 Experimental setup for the absorption measurements 63
3.9 Experimental setup for the fluorescence measurements 64

4.1 Energy levels of the Pr^{3+} ion and the transition studied 66
4.2 Absorption of KY_3F_{10} 0.3% Pr^{3+} in the 420-500nm regions. 68
4.3 Polarized absorption of KYF_4 1.25% Pr^{3+} in the 420-500nm interval . 69
4.4 Polarized absorption of $LiLuF_4$ 1.25% Pr^{3+} in the 430-490nm regions 70
4.5 Polarized absorption of BaYF 1.25% Pr^{3+} in the 420-500nm regions . 71
4.6 Polarized absorption of BaYF 3% Pr^{3+} in the 420-500nm regions . . . 73
4.7 Normalized f_{abs} plotted versus the volume of the sample, the label indicated in Table 4.1 are used to discriminate the different sample. . 77
4.8 Unpolarized fluorescence at room temperature of 1.25%Pr:$LiLuF_4$. . . 79
4.9 Unpolarized fluorescence at room temperature of 1.25%PrKYF_4 sample. 79
4.10 Unpolarized fluorescence at room temperature of 1.25%Pr:BaY_2F_8 samnple. 80
4.11 Unpolarized fluorescence at room temperature of 0.3%Pr:KY_3F_{10} sample. 80

4.12 GaN laser diode spectrum for the efficiency measurement 81
4.13 Plot of the efficiency measured versus the nominal doping levels. . . . 85
4.14 Colour coordinate of the samples reported in the CIE 1931 diagram, the white regions is reported 87
4.15 Energy levels of Sm^{3+} and Eu^{3+} and studies transition 92
4.16 1% $Sm^{3+/2+}$:BaY_2F_8 polarized fluorescence 94
4.17 (a)1% Eu^{3+}:BaY_2F_8 polarized fluorescence (b) colour coordinate of the sample investigated. 95

5.1 Comparison between the room temperature absorption, in π polarization, of KYF_4 (left axis) and $LiLuF_4$ (right axis). The level assignment refers to $LiLuF_4$. 99
5.2 Simplified Pr^{3+} energy level scheme. Arrows indicate the pump wavelengths and the main transitions discussed in the paper. 101
5.3 Polarized room temperature fluorescence pumping with the diode laser. 102
5.4 Polarized room temperature fluorescence pumping with the argon laser. 103
5.5 Room temperature fluorescence in σ polarization pumping with both argon and diode lasers. The red arrows indicate the observation wavelength in lifetime measurements. 104
5.6 Unpolarized fluorescence vs temperature pumping with diode laser. . 105
5.7 Unpolarized fluorescence vs temperature pumping with argon laser. . 106
5.8 Arrhenius plot of the peak area pumping with both argon and diode lasers. 107

6.1 TTB structure with the conventional sites nomenclature. 110
6.2 Configurations of the triangular channels resulting from the modulation of the BNN structure and allowing the accommodation of the Pr^{3+} ions in the C site 115

6.3 Polarized emission spectra of Pr BNN samples measured upon 476.5 nm laser excitation. 117

6.4 Polarized emission spectra of the most Pr BNN doped sample,measured upon 476.5 nm laser excitation. 118

6.5 The 600-680 nm emission manifold (π polarization, E parallel c axis) measured (a) for different excitation wavelengths for the 0.5% sample 118

6.6 The 600-680 nm emission manifold (π polarization, E parallel c axis) measured for different Pr^{3+} concentrations. 119

6.7 Radiative emission and Non-radiative mechanisms affecting the $^3P_0$ and $^1D_2$ emission of Pr^{3+} in oxide lattices. 120

6.8 Unpolarized fluorescence spectra of BNN Pr for various concentration. 121

6.9 Excitation spectra at room temperature of BNN Pr at various concentration. 122

6.10 Emission decay profiles of Pr : BNN. 124

7.1 10 K polarized absorption spectrum of YPO_4 :Dy (3%). 129

7.2 10 K polarized emission spectrum of YPO_4:Dy (3%) 132

7.3 298 K polarized absorption spectrum of YPO_4:Dy (3%). 136

7.4 298 K polarized absorption spectrum of YPO_4:Dy (3%). 138

7.5 10 K emission decay profiles of $^4F_{\frac{9}{2}}$ manifold in differently concentrated YPO_4:Dy crystals. 140

7.6 Temperature dependence of the $^4F_{\frac{9}{2}}$ manifold lifetime of the YPO_4: Dy (0.5% and 3%) 141

8.1 Energy level diagram of Tm^{3+} in the region of interest. Γ indicates the pump at $\sim$ 800 nm, CR stand for the cross relaxation process ($^3H_4$,$^3H_6$) $\rightarrow$ ($^3F_4$,$^3F_4$) and the laser emission $^3F_4 \rightarrow ^3H_6$ around 2 μm. 146

8.2 Absorption sigma in π and σ polarization of the ground state absorption of the ($^3F_2$+$^3F_3$) and $^3H_4$ manifolds. 147
8.3 Absorption sigma in π and σ polarization of the ground state absorption of the $^3F_4$ level. 148
8.4 Decay of the $^3F_4 \rightarrow ^3H_6$ transition in Tm YLF, by exciting at 780 nm and observing at 1832 nm. 149
8.5 Comparison of the σ_{ems} of $^3F_4 \rightarrow ^3H_6$ transition in π polarization calculated with the $\beta - \tau$ and reciprocity method. 150
8.6 Comparison of the σ_{ems} of $^3F_4 \rightarrow ^3H_6$ transition in σ polarization calculated with the $\beta - \tau$ and reciprocity method. 150
8.7 Tm:YLF polarized gain coefficient N σ_{gain} (N=1.1×10^{21} ions/cm^3 is the doping density) for two values of the inversion parameter β. . . . 152
8.8 Setup of the PQS Tm:YLF laser. SA: Cr:ZnS saturable absorber, M1: dichroic pump mirror, M2: HR-laser, HT-pump mirror, M3: output coupler. 153
8.9 CW laser performance of the Tm:YLF laser. 154
8.10 PQS characteristics of the Tm:YLF laser using Cr:ZnS SA with T_0=92%. 155
8.11 PQS characteristics of the Tm:YLF laser using Cr:ZnS SA with T_0=85% low signal transmission. 156
8.12 Tm:YLF laser spectra in CW and PQS regimes using different Cr:ZnS SAs. The transmission of the output coupler at the actual laser wavelength is ≈35% (CW), ≈40% (T0=92%) and ≈50% (T0=85/75%). . 157

A.1 Method of interpolation to find correlated colour temperature [158]. . 163

List of Tables

2.1 Radiometric and photometric quantities and units. 19

3.1 Summary or the Pr-studied crystals [75, 64, 68, 71] 52

4.1 Absorption results, for any sample we report the absorption. 76
4.2 Intrinsic efficiency evaluated for the sample. 82
4.3 Luminous efficiency for common light emitters, sources: PHILIPS and OSRAM and [80]. 84
4.4 CIE 1931 colour coordinate of the sample studied pumped with GaN laser diode(λ=444nm). 88
4.5 Correlated colour temperature for every investigated sample calculate using the McCamy approximation ([86, 87]) and according to the most recent method developed by Javier Hernández-Adrés, Raymond L.Lee and Javier Romero([88]). 89
4.6 CIE Standard illuminants [41]. 91
4.7 Chromatic characterization of the principal commercial white light sources [89] and Kodak catalogue. 91

5.1 Lifetime values observed in KYF:Pr exciting at two different wavelength, 445 and 457 nm. The decay curves were recorded relatively to the two main emission peaks. 103

6.1 Crystal data. 111
6.2 Atomic coordinates and displacement parameters (Å). 112
6.3 Selected bond lengths and distances (Å). 113
6.4 Effective emission decay time estimated for the $^3P_0$ and $^1D_2$ manifolds at 10 K and 300 K temperature. 125

7.1 Energy levels scheme of Dy^{3+} in YPO_4. 131
7.2 Free-ion parameters for Dy^{3+} in YPO_4. 133
7.3 CF parameters (cm^{-1}) for Dy^{3+} in YPO_4. The values determined by fitting the experimental energies are compared with those evaluated with the SPM. 133
7.4 Experimental and calculated oscillator strengths (P) of Dy^{3+} in YPO_4. The Judd-Ofelt parameters, Ω_λ , the RMS and the percent error are also tabulated. 135
7.5 Calculated spontaneous emission probabilities A and radiative branching ratios β for the $^4F_{9/2}$ emitting level. 137
7.6 (a) Comparison between the intensity parameters, the radiative lifetime of $^4F_{9/2}$ and the calculated (Y/B) ratio in the YPO_4 and YVO_4 host lattices. (b) Reduced matrix elements for some relevant absorption and emission transitions [140] 138

A.1 Epicentre coordinates and constants for eq. A.6 164